Part 1:

Finite Element Development and Technology

Chapter 2

Stability of elastostatic elements with drilling degrees of freedom

2.1 Summary

This chapter presents a short introduction and background to finite element formulations with drilling degrees of freedom (DOFs). Early parts of the chapter are largely given as a background to the formulation of elements with drilling DOFs. However, this chapter also presents a new contribution which has been made in the stability analysis of these elements. In particular, the novel idea of using the skew-symmetric part of stress as an error estimate has been proposed.

In particular, a numerical investigation into the effect of the penalty parameter in elements with drilling DOFs, for which the stress tensor $\boldsymbol{\sigma}$ is not *a priori* assumed to be symmetric, is offered. The parameter under investigation is γ, which relates the in-plane translations to the rotations for elements with drilling DOFs. Rather than simply reporting on the quantitative influence of γ on measures like displacement, rotation and stress, the skewness of the nonsymmetric stress tensor is directly assessed. Results are presented for both isotropic and orthotropic constitutive relationships.

2.1.1 A word on notation

Before starting with the presentation, some brief notes on the notation employed are called for. Firstly, the notations employed to denote variables in this chapter, and in Chapter 3, differ somewhat. In the present chapter, the conventional mechanical symbolic designations are used, whereas in Chapter 3 the symbols traditionally used in the piezoelectric research community are employed. For example in what is to follow, $\boldsymbol{\epsilon}$ denotes the mechanical strain tensor, which is denoted $\boldsymbol{S}$ in Chapter 3. Furthermore, in Chapter 3 the symbol $\boldsymbol{\epsilon}$ is reserved for the dielectric constitutive properties. To avoid confusion, the notation employed is explained in detail in the text of each chapter and should not be assumed to be consistent throughout this work.

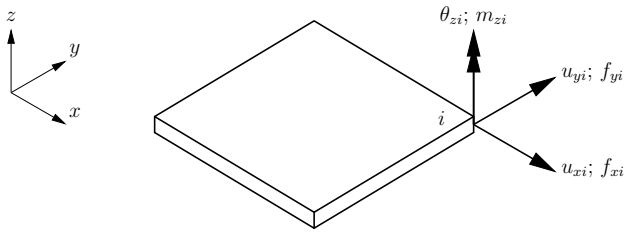

(a) Membrane deformations and forces.

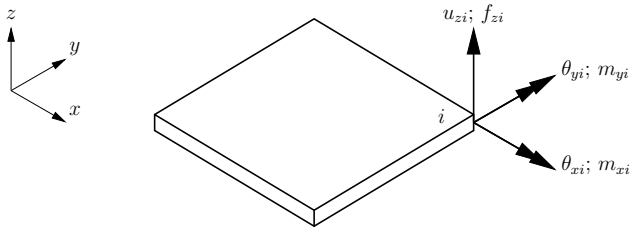

(b) Bendng deformations and forces.

Figure 2.1: Flat element subject to in-plane membrane and bending actions.

Secondly, a conventional tensor notation, similar to that employed by for example Pimpinelli [20], where "·" is reserved for the scalar inner product between tensors of given order, is used. This notation is slightly different to that employed for example by Hughes and Brezzi [18] or Ibrahimbegovic *et al.* [21].

2.2 Introduction

In this section some background is presented on finite elements with drilling degrees of freedom (DOFs). Much of the work in the early part of this chapter is relatively widely known, but is given here as an introduction for those readers unfamiliar with the topic.

In recent times, elements with in-plane rotational (drilling) degrees of freedom have become quite popular. Apart from enrichment of the displacement field, which increases element accuracy, drilling degrees of freedom allow for the modelling of, for instance, folded plates and beam-slab intersections. Although only planar membrane elements are considered in this chapter, the need for elements with an in-plane rotational DOFs should be seen in the light of their application in shell analyses. Plane stress membrane elements are commonly combined with plate elements to form flat shell elements. The membrane and plate (bending) constituents of such a flat shell element are depicted separately in Figure 2.1. The element possesses nodal displacements u_x, u_y and u_z and rotations θ_x, θ_y and θ_z, and can be subjected to both in-plane membrane and bending actions at each node i.

As explained for example in Zienkiewicz and Taylor [22], for in-plane actions, the states of stress and strain can be uniquely defined in terms of the two in-plane displacements. The

relation between in-plane forces and displacements is given by:

$$\boldsymbol{k}^{\mathrm{m}}\boldsymbol{q}^{\mathrm{m}} = \boldsymbol{f}^{\mathrm{m}}, \tag{2.1}$$

where $\boldsymbol{q}^{\mathrm{m}} = [\boldsymbol{u}_{xi} \;\; \boldsymbol{u}_{yi}]^T$, represents the in-plane displacements in the x and y directions, with corresponding forces $\boldsymbol{f}^{\mathrm{m}} = \left[\boldsymbol{f}_{xi} \;\; \boldsymbol{f}_{yi}\right]^T$. The components of displacement are comprised of the displacements at each node. For the 4-node element depicted in Figure 2.1, we have $\boldsymbol{u}_{xi} = [u_{x1} \;\; u_{x2} \;\; u_{x3} \;\; u_{x4}]^T$, $\boldsymbol{u}_{yi} = [u_{y1} \;\; u_{y2} \;\; u_{y3} \;\; u_{y4}]^T$, with the forces expanded similarly. The superscript 'm' denotes these as in-plane membrane components. $\boldsymbol{k}^{\mathrm{m}}$ is the membrane stiffness matrix.

Similarly, the bending components can be expressed uniquely in terms of the out-of-plane displacement and two rotations at each node as

$$\boldsymbol{k}^{\mathrm{b}}\boldsymbol{q}^{\mathrm{b}} = \boldsymbol{f}^{\mathrm{b}}, \tag{2.2}$$

where $\boldsymbol{q}^{\mathrm{b}} = [\boldsymbol{u}_{zi} \;\; \boldsymbol{\theta}_{xi} \;\; \boldsymbol{\theta}_{yi}]^T$, with the forces and moments given by $\boldsymbol{f}^{\mathrm{b}} = [\boldsymbol{f}_{zi} \;\; \boldsymbol{m}_{xi} \;\; \boldsymbol{m}_{yi}]^T$. In this case, the superscript 'b' indicates that these terms are bending-related, and $\boldsymbol{k}^{\mathrm{b}}$ is the plate bending stiffness matrix.

In this simple illustrative example, there is no coupling between in-plane and bending actions. What is more, up to this point it has not been necessary, at least in terms of the description of the problem mechanics, to include the in-plane rotations ($\boldsymbol{\theta}_{zi}$).

All six degrees of freedom at each node can now be assembled as

$$\boldsymbol{k}\boldsymbol{q} = \boldsymbol{f}, \tag{2.3}$$

where, at each node, displacements and rotations are given as $\boldsymbol{q}_i = [\boldsymbol{q}_i^{\mathrm{m}} \;\; \boldsymbol{q}_i^{\mathrm{b}} \;\; \boldsymbol{\theta}_{zi}]^T$ and the forces and moments are assembled as $\boldsymbol{f}_i = [\boldsymbol{f}_i^{\mathrm{m}} \;\; \boldsymbol{f}_i^{\mathrm{b}} \;\; \boldsymbol{m}_{zi}]^T$. The stiffness matrix is in turn, made up of the following submatrices for a 4-node element

$$\boldsymbol{k} = \left[\begin{array}{c|c|c} \boldsymbol{k}^{\mathrm{m}}_{8\times 8} & \mathbf{0}_{8\times 12} & \mathbf{0}_{20\times 4} \\ \hline \mathbf{0}_{12\times 8} & \boldsymbol{k}^{\mathrm{b}}_{12\times 12} & \\ \hline \multicolumn{2}{c|}{\mathbf{0}_{4\times 20}} & \mathbf{0}_{4\times 4} \end{array}\right], \tag{2.4}$$

where no stiffness is associated with the rotational degree of freedom.

Difficulties arise if any number of flat shell elements employing this formulation, connected at a node, are co-planar (or nearly so) [22]. Examples of this type of assemblage include flat shell segments, as well as straight boundaries of singly curved shells. When the local coordinate directions of these elements happen to coincide with the global coordinates, the equilibrium equations corresponding to terms with $\boldsymbol{\theta}_{zi}$ reduce to 0=0, which does not present special difficulties. However, if the local and global coordinates differ the global stiffness matrix becomes singular, and detection of this singularity could present difficulties. If it is not possible to assemble stiffness matrices in local coordinates (and simply delete all 0=0 equations), an arbitrary stiffness k'_{θ_z}, can be inserted at these points only. Both of these procedures lead to programming difficulties in general codes, due to the subjective nature of 'nearly co-planar' detection.

There are several problems (apart from the rank deficiency) associated with this type of element. The ordinary membrane part of the stiffness matrix employing an isoparametric formulation is usually very stiff, especially in bending. This problem can be alleviated by employing a mixed or hybrid element, or an element with an enhanced strain formulation. A more serious problem is that of possible incompatible in-plane rotation which could occur in an assembly, for example in beam-slab connections, or at the intersection of a folded plate.

These issues can be addressed if suitable membrane elements with drilling degrees of freedom (DOFs) are formulated, implemented and superimposed on an appropriate plate element to form a shell element with 6 DOFs per node. Since most general and commercial finite element codes make provision for 6 DOFs per node in any case, this improvement is largely cost free in terms of computational and implementational effort [22]. Furthermore, the resulting membrane elements are generally more accurate due to an enrichment of the displacement field [21, 23, 24].

2.3 Historical development of elements with drilling DOFs

In this section a brief history of the development of elements with drilling DOFs is presented. Distinction will be made between *vertex* (or ω) rotations which need not be directly related to the continuum mechanics definition of in-plane rotation, and *drilling* (or Ω) rotations that are. In a finite element setting, the Ω drilling degree of freedom may be physically interpreted as a true rotation of the vertex bisecting the angle between adjacent edges of the finite element. The continuum mechanics definition of the in-plane rotation field Ω_z is

$$\Omega_z = \frac{1}{2}\left(\frac{\partial u_y}{\partial x} - \frac{\partial u_x}{\partial y}\right), \tag{2.5}$$

where u_x and u_y are the components of the in-plane displacement field in the x and y directions, respectively.

Compilations of early (unsuccessful) efforts to develop elements with drilling DOFs are presented by Frey [25] and Bergan and Felippa [26] as well as, among others, [27, 28]. Several early attempts to develop membrane elements with drilling DOFs failed, for example [29, 30]. These repeated failures prompted Irons and Ahmad [31] to view as futile the task of constructing elements with drilling degrees of freedom.[1]

However in the mid-80's, Allman [32] and Bergan and Felippa [26] achieved a previously unattained level of success. Instead of the cubic functions previously used, they employed a quadratic displacement function for the normal component of displacement.

The interpolation used by Allman (referred to as Allman interpolations) is depicted in Figure 2.2. Specifically the interpolation consists of a quadratic function for the component of displacement normal to the element side, and a linear form for the tangential component of displacement.

[1] To be fair though, some of the theory used to develop current elements was not known to them at the time [26].

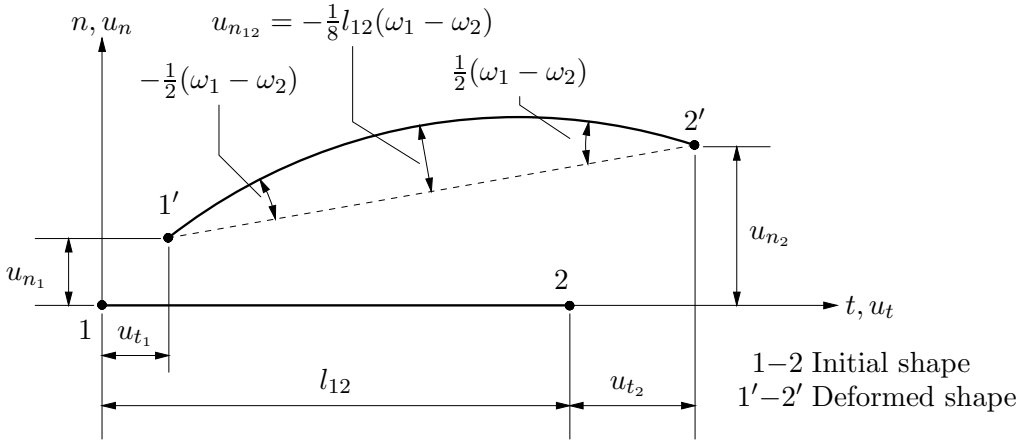

Figure 2.2: Displacement of an element side 1−2.

According to Allman [32] (who introduced the term 'vertex rotations'), the relation between vertex rotation, ω, and normal displacement is given by

$$-\omega_2 + \omega_1 = \frac{\partial u_n}{\partial s}|_l - \frac{\partial u_n}{\partial s}|_0, \tag{2.6}$$

where ω_1 and ω_2 are the vertex rotations at nodes 1 and 2, respectively. It can be shown that this reduces to

$$\omega_1 - \omega_2 = -\frac{8}{l_{12}} u_{n_{12}}. \tag{2.7}$$

The interpolation of u_n can therefore be written in terms of nodal vertex rotations as

$$u_n = (1 - \frac{s}{l_{12}})u_{n_1} + \frac{s}{l_{12}} u_{n_2} - \frac{s}{2}(1 - \frac{s}{l_{12}})(\omega_1 - \omega_2). \tag{2.8}$$

Clearly, these vertex rotations are not the same as the true rotations for plane elasticity, defined in (2.5), but related to them in an indeterminate way only [25].

Since then, many papers on the subject have appeared. Cook [33] showed that the Allman element can be obtained by applying a coordinate transformation to a higher order element with mid-side nodes. This technique was extended to elements other than triangles, resulting in rank deficient quadrilateral elements. MacNeal and Harder [24] refined this element by developing a method to suppress the rank deficiency.

Other noteworthy developments are credited to Jetteur, Jaamei and Frey [25, 34, 35, 36] and to Taylor and Simo *et al.* [37, 38, 39].

More recently, Hughes and Brezzi [18], presented a rigorous mathematical framework in which to formulate elements with independent rotational interpolations. They argue that, utilising the formulation of Reissner [40], formulations employing 'convenient' displacement, rotation and stress interpolations are doomed to failure. Instead, they propose a modified variational principle, with improved stability properties in the discrete form.

Early finite element interpolations employing the formulation of Hughes and Brezzi were presented by Hughes *et al.* [41] and Ibrahimbegovic *et al.* [21, 42]. These elements depend

on a problem-dependent penalty parameter γ, which relates the in-plane translations to the in-plane rotations. The value of γ has been the topic of a number of studies [18, 21, 43, 44, 44]. For linear elastic isotropic Dirichlet problems, the formulation is reported to be relatively insensitive to the value of γ [18, 21, 45], and it was proposed that $\gamma = \mu$, with μ the shear modulus. For different conditions (e.g. orthotropy or elastodynamics), a greater sensitivity to the value of γ is to be expected. For dynamic problems, for example, Hughes *et al.* [44] propose $\gamma = \mu/10$.

Independent from work on drilling degrees of freedom, the developments in mixed/hybrid membrane finite elements have been equally important during recent years. Since the assumed stress finite element presented by Pian [46], numerous formulations have been proposed. A compilation is presented by Pian [47]. Eventually, assumed stress formulations were combined with drilling degrees of freedom in a single element formulation, e.g. see Aminpour [48, 49], Sze and Ghali [50], and Geyer and Groenwold for quadrilateral 8β and 9β drill families [43].

Since then, the development of membrane finite elements with drilling DOFs has been significant. Sze and co-workers [51, 50] developed elements with in-plane rotations and assumed stress fields. Groenwold and Stander [52, 53] applied the 5-point quadrature presented by Dovey [54] to drilling degree of freedom membranes, which improved the element behaviour through the introduction of a 'soft' higher order deformation mode. Later Geyer and Groenwold [43] also developed assumed stress finite elements with drilling DOFs. Recently Pimpinelli developed an assumed strain quadrilateral element with drilling degrees of freedom [20].

In this chapter the effect of the parameter γ, which relates the in-plane translations and rotations, is numerically investigated. The chapter is set out as follows: Firstly in Section 2.4, the framework developed by Hughes and Brezzi [18], within which elements with drilling DOFs are formulated, is presented. The finite element interpolations employed are then detailed in Section 2.5. Next, stability requirements for the Dirichlet elastostatic problem due to Hughes and Brezzi are briefly discussed in Section 2.6. In Section 2.7, stability and consistency requirements are numerically verified for constant stress states. Numerical results are presented in Section 2.8, while concluding remarks are presented in Section 2.9.

2.4 Variational formulation of elements with drilling DOFs

The focus of this chapter is the element sensitivity to the problem dependant parameter γ, and not the variational formulation of the elements. It would therefore not be appropriate to present details of the variational formulation of elements with drilling DOFs here, especially since that information can be found in the references presented in Section 2.3. Instead, only the functionals from which the elements used in this study are derived (as introduced in [18]), are presented.

This presentation is merely to illustrate the framework wherein these elements are formulated, as well as to act as an introduction to show how this framework for the elastostatic

problem was extended for piezoelectricity in Chapter 3.

We proceed, as in [20], by defining $\bar{\Omega}$ as a closed and bounded domain occupied by a body in three dimensional space. The interior part of $\bar{\Omega}$ is denoted by Ω and it's boundary by $\partial\Omega$, $\Omega \cup \partial\Omega = \bar{\Omega}$. The measure of Ω is V and the measure of $\partial\Omega$ is S. $\mathcal{V}$ is the vector space associated with the Euclidean point space and $\mathcal{L}$ the space of all linear applications of $\mathcal{V}$ into $\mathcal{V}$, which possesses inner product $\boldsymbol{A} \cdot \boldsymbol{B} = \mathrm{tr}(\boldsymbol{A}^t\boldsymbol{B})$, $\boldsymbol{A}, \boldsymbol{B} \in \mathcal{L}$ and $\boldsymbol{A}^t$ the transpose of $\boldsymbol{A}$ (see [20]). Reference will also be made to subsets of $\mathcal{L}$, namely $\mathcal{S}$ and $\mathcal{W}$ which contain, respectively symmetric and skew-symmetric tensors in $\mathcal{L}$.

The boundary $\partial\Omega$, is split into two parts, $\partial\Omega_u$ and $\partial\Omega_t$ such that $\partial\Omega_u \cup \partial\Omega_t = \partial\Omega$ and $\partial\Omega_u \cap \partial\Omega_t = \emptyset$. On $\partial\Omega_u$ displacements $\bar{\boldsymbol{u}}$ are prescribed, while on $\partial\Omega_t$ the traction $\bar{\boldsymbol{t}}$ is prescribed.[2] The discussion is limited to linear elastic problems and discussion of boundary conditions is omitted.[3]

In the most general case, the stress tensor, $\boldsymbol{\sigma} \in \mathcal{L}$ (which is not *a priori* assumed to be symmetric), the displacement vector field $\boldsymbol{u}$, the skew-symmetric infinitesimal rotational tensor, $\boldsymbol{\psi} \in \mathcal{W}$, and the strain tensor $\boldsymbol{\epsilon} \in \mathcal{S}$ are taken as dependent variables. The variational formulation requires the rotations $\boldsymbol{\psi}$, strains $\boldsymbol{\epsilon}$ and stresses $\boldsymbol{\sigma}$, together with the displacement generalised derivatives $\boldsymbol{\nabla u}$, belong to the space of square-integrable functions over the region Ω.

The Euclidean decomposition of a second-rank tensor is used, e.g.,

$$\boldsymbol{\sigma} \;=\; \mathrm{symm}\;\boldsymbol{\sigma} + \mathrm{skew}\;\boldsymbol{\sigma}, \tag{2.9}$$

where

$$\mathrm{symm}\;\boldsymbol{\sigma} = \frac{1}{2}(\boldsymbol{\sigma} + \boldsymbol{\sigma}^t), \tag{2.10}$$

$$\mathrm{skew}\;\boldsymbol{\sigma} = \frac{1}{2}(\boldsymbol{\sigma} - \boldsymbol{\sigma}^t). \tag{2.11}$$

The problem under consideration is now constructed as follows: Given $\boldsymbol{f}$, the body force vector, find $\boldsymbol{u}$, $\boldsymbol{\psi}$, $\boldsymbol{\sigma}$ and $\boldsymbol{\epsilon}$ such that:

$$\mathrm{div}\;\boldsymbol{\sigma} + \boldsymbol{f} = \boldsymbol{0}, \tag{2.12}$$

$$\mathrm{skew}\;\boldsymbol{\sigma} = \boldsymbol{0}, \tag{2.13}$$

$$\boldsymbol{\psi} = \mathrm{skew}\boldsymbol{\nabla u}, \tag{2.14}$$

$$\boldsymbol{\epsilon} = \mathrm{symm}\boldsymbol{\nabla u}, \tag{2.15}$$

$$\mathrm{symm}\;\boldsymbol{\sigma} = \boldsymbol{c}\;\boldsymbol{\epsilon}, \tag{2.16}$$

for all $\boldsymbol{x} \in \Omega$. Equations (2.12) through (2.16) represent respectively, the linear and rotational momentum balance equations, the definition of rotation in terms of displacement

[2] It is of course possible to have part of the boundary with both displacements and tractions prescribed, as often used to simulate symmetry boundary conditions [55]. However, at no point are both forces and displacements in coincident directions prescribed.

[3] Boundary conditions may be incorporated in the standard manner, e.g. see [16, 21, 56, 57], and will be dealt with in more detail in Chapter 3.

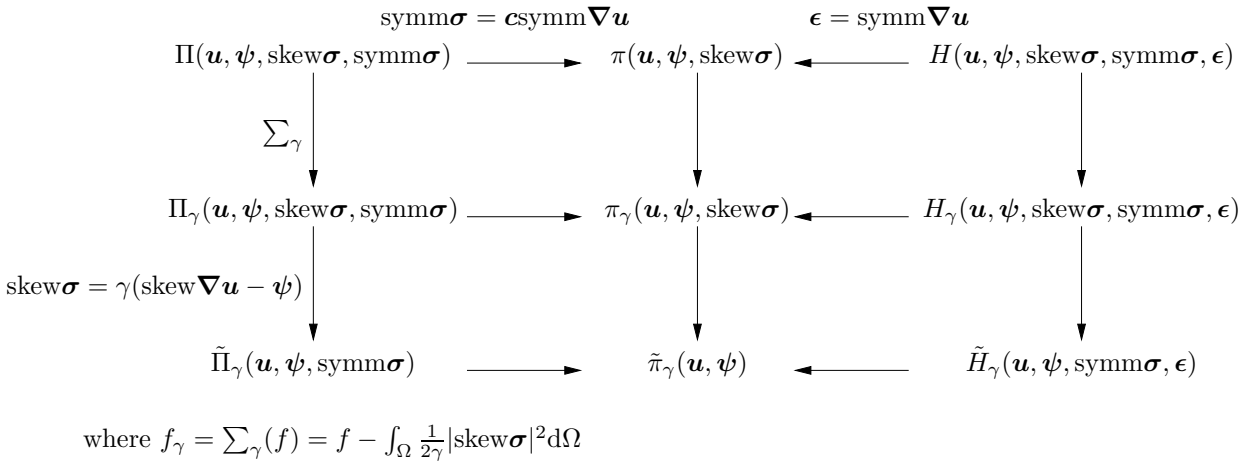

Figure 2.3: Relationship among functionals. (Figure from [18].)

gradient, the compatibility condition for strain in terms of displacement gradient and the constitutive equations. The tensor of elastic stiffness is represented by $\boldsymbol{c}$.

Reissner [40] presented a variational formulation for the boundary value problem reflected in (2.12) to (2.16). However, this formulation is inappropriate for numerical applications. The problems associated with Reissner's formulation are summarised, and addressed in the ground-breaking paper of Hughes and Brezzi [18]. Upon concluding their paper, a graphical illustration of the relationships between the various functionals employed in their study is given. These relations are repeated in Figure 2.3.

The functionals denoted H are used as a basis for Hu-Washizu type variational formulations, while those denoted Π are used to construct Hellinger-Reissner like formulations. The simplest functionals which ultimately result in 'irreducible' displacement-based formulations are denoted π.

In particular, the functional denoted H is given explicitly by Hughes and Brezzi [18] as

$$H(\boldsymbol{u}, \boldsymbol{\psi}, \text{skew}\boldsymbol{\sigma}, \text{symm}\boldsymbol{\sigma}, \boldsymbol{\epsilon}) = \frac{1}{2}\int_\Omega \boldsymbol{c\epsilon} \cdot \boldsymbol{\epsilon} \text{d}V + \int_\Omega (\text{symm}\boldsymbol{\nabla u} - \boldsymbol{\epsilon}) \cdot \text{symm}\boldsymbol{\sigma} \text{d}V + \int_\Omega (\text{skew}\boldsymbol{\nabla u} - \boldsymbol{\psi}) \cdot \text{skew}\boldsymbol{\sigma} \text{d}V - \int_\Omega \boldsymbol{f} \cdot \boldsymbol{u} \text{d}V + \text{Boundary Terms}, \quad (2.17)$$

where symm$\boldsymbol{\sigma}$ acts as a Lagrange multiplier enforcing the compatibility conditions and skew$\boldsymbol{\sigma}$ enforces the relationship between $\boldsymbol{\psi}$ and $\boldsymbol{u}$.

It can be shown that the functional H can be used to derive a Hellinger-Reissner like functional Π by substituting $\boldsymbol{\epsilon} = \boldsymbol{s}\ \boldsymbol{\sigma}$ into (2.17), where $\boldsymbol{s} = \boldsymbol{c}^{-1}$ is the compliance tensor. Since $\boldsymbol{\epsilon}$ does not appear in the functional, the compatibility conditions are enforced in a strong sense *a priori*. This connection is not illustrated in the original figure, see Figure 2.3. The

functional Π is now given as

$$\Pi(\boldsymbol{u},\boldsymbol{\psi},\text{skew}\boldsymbol{\sigma},\text{symm}\boldsymbol{\sigma}) = -\frac{1}{2}\int_\Omega \boldsymbol{s}\text{symm}\boldsymbol{\sigma}\cdot\text{symm}\boldsymbol{\sigma}\text{d}V + \int_\Omega \text{symm}\boldsymbol{\nabla u}\cdot\text{symm}\boldsymbol{\sigma}\text{d}V + \int_\Omega(\text{skew}\boldsymbol{\nabla u}-\boldsymbol{\psi})\cdot\text{skew}\boldsymbol{\sigma}\text{d}V - \int_\Omega \boldsymbol{f}\cdot\boldsymbol{u}\text{d}V + \text{Boundary Terms}. \quad (2.18)$$

A similar Π functional to that found in, for example [43, 58], is presented. This functional is slightly different to the one suggested by Reissner [40] and used by Hughes and Brezzi as a basis for their theory [18]. However, it results in the same Euler-Lagrange equations as the one suggested by Reissner and Hughes and Brezzi.

Finally, as shown in Figure 2.3, the functional π can be derived by either substituting the compatibility conditions into H or by substituting $\text{symm}\boldsymbol{\sigma} = \boldsymbol{c}\,\text{symm}\boldsymbol{\nabla u}$ into Π. The π functional can then be trivially shown to be

$$\pi(\boldsymbol{u},\boldsymbol{\psi},\text{skew}\boldsymbol{\sigma}) = \frac{1}{2}\int_\Omega \boldsymbol{c}\text{symm}\boldsymbol{\nabla u}\cdot\text{symm}\boldsymbol{\nabla u}\text{d}V + \int_\Omega(\text{skew}\boldsymbol{\nabla u}-\boldsymbol{\psi})\cdot\text{skew}\boldsymbol{\sigma}\text{d}V - \int_\Omega \boldsymbol{f}\cdot\boldsymbol{u}\text{d}V + \text{Boundary Terms}. \quad (2.19)$$

The functionals which have been presented thus far are not appropriate for numerical implementation. The Π functional suggested by Reissner in particular, was shown to have stability problems in the discrete form [18]. The variational problem of Reissner was modified in order to preserve the stability of the discrete problem by the addition of the term $\frac{1}{2\gamma}\int_\Omega |\text{skew}\boldsymbol{\sigma}|^2\,\text{d}V$ [18], as depicted in Figure 2.3. The resulting Hu-Washizu type functional H_γ, after the modification is thus given by

$$H_\gamma(\boldsymbol{u},\boldsymbol{\psi},\text{skew}\boldsymbol{\sigma},\text{symm}\boldsymbol{\sigma},\boldsymbol{\epsilon}) = \frac{1}{2}\int_\Omega \boldsymbol{c}\boldsymbol{\epsilon}\cdot\boldsymbol{\epsilon}\text{d}V + \int_\Omega(\text{symm}\boldsymbol{\nabla u}-\boldsymbol{\epsilon})\cdot\text{symm}\boldsymbol{\sigma}\text{d}V + \int_\Omega(\text{skew}\boldsymbol{\nabla u}-\boldsymbol{\psi})\cdot\text{skew}\boldsymbol{\sigma}\text{d}V - \frac{1}{2\gamma}\int_\Omega |\text{skew}\boldsymbol{\sigma}|^2\text{d}V - \int_\Omega \boldsymbol{f}\cdot\boldsymbol{u}\text{d}V + \text{Boundary Terms}. \quad (2.20)$$

The corresponding Hellinger-Reissner-like functional Π_γ can be shown to be

$$\Pi_\gamma(\boldsymbol{u},\boldsymbol{\psi},\text{skew}\boldsymbol{\sigma},\text{symm}\boldsymbol{\sigma}) = -\frac{1}{2}\int_\Omega \boldsymbol{s}\text{symm}\boldsymbol{\sigma}\cdot\text{symm}\boldsymbol{\sigma}\text{d}V + \int_\Omega \text{symm}\boldsymbol{\nabla u}\cdot\text{symm}\boldsymbol{\sigma}\text{d}V + \int_\Omega(\text{skew}\boldsymbol{\nabla u}-\boldsymbol{\psi})\cdot\text{skew}\boldsymbol{\sigma}\text{d}V - \frac{1}{2\gamma}\int_\Omega |\text{skew}\boldsymbol{\sigma}|^2\text{d}V - \int_\Omega \boldsymbol{f}\cdot\boldsymbol{u}\text{d}V + \text{Boundary Terms}, \quad (2.21)$$

and the equivalent π functional including $\text{skew}\boldsymbol{\sigma}$ can be written as

$$\pi_\gamma(\boldsymbol{u},\boldsymbol{\psi},\text{skew}\boldsymbol{\sigma}) = \frac{1}{2}\int_\Omega \boldsymbol{c}\text{symm}\boldsymbol{\nabla u}\cdot\text{symm}\boldsymbol{\nabla u}\text{d}V + \int_\Omega(\text{skew}\boldsymbol{\nabla u}-\boldsymbol{\psi})\cdot\text{skew}\boldsymbol{\sigma}\text{d}V - \frac{1}{2\gamma}\int_\Omega |\text{skew}\boldsymbol{\sigma}|^2\text{d}V - \int_\Omega \boldsymbol{f}\cdot\boldsymbol{u}\text{d}V + \text{Boundary Terms}. \quad (2.22)$$

Finally, it is possible, and indeed attractive for the skew-symmetric part of the stress tensor to be eliminated from the functionals by substituting $\text{skew}\boldsymbol{\sigma} = \gamma(\text{skew}\boldsymbol{\nabla u} - \boldsymbol{\psi})$, which appears as one of the Euler-Lagrange equations in the foregoing three functionals. The resulting Hu-Washizu like functional can be shown to be

$$\tilde{H}_\gamma(\boldsymbol{u}, \boldsymbol{\psi}, \text{symm}\boldsymbol{\sigma}, \boldsymbol{\epsilon}) = \frac{1}{2}\int_\Omega \boldsymbol{c\epsilon} \cdot \boldsymbol{\epsilon} \text{d}V + \int_\Omega (\text{symm}\boldsymbol{\nabla u} - \boldsymbol{\epsilon}) \cdot \text{symm}\boldsymbol{\sigma} \text{d}V + \frac{\gamma}{2}\int_\Omega |\text{skew}\boldsymbol{\nabla u} - \boldsymbol{\psi}|^2 \text{d}V - \int_\Omega \boldsymbol{f} \cdot \boldsymbol{u} \text{d}V + \text{Boundary Terms}. \quad (2.23)$$

Pimpinelli [20] used a slightly modified version of the $\tilde{H}_\gamma$ functional to derive a numerical model based on the minimisation of his modified Hu-Washizu like functional. His element is based in the framework of the assumed strain method of Simo and Rifai [59]. The Hellinger-Reissner like equivalent, using the base functional Π_γ is found to be

$$\tilde{\Pi}_\gamma(\boldsymbol{u}, \boldsymbol{\psi}, \text{symm}\boldsymbol{\sigma}) = -\frac{1}{2}\int_\Omega \boldsymbol{s}\text{symm}\boldsymbol{\sigma} \cdot \text{symm}\boldsymbol{\sigma} \text{d}V + \int_\Omega \text{symm}\boldsymbol{\nabla u} \cdot \text{symm}\boldsymbol{\sigma} \text{d}V + \frac{\gamma}{2}\int_\Omega |\text{skew}\boldsymbol{\nabla u} - \boldsymbol{\psi}|^2 \text{d}V - \int_\Omega \boldsymbol{f} \cdot \boldsymbol{u} \text{d}V + \text{Boundary Terms}. \quad (2.24)$$

Finally, the resulting 'irreducible' functional with only displacement and in-plane rotations as independent variables is

$$\tilde{\pi}_\gamma(\boldsymbol{u}, \boldsymbol{\psi}) = \frac{1}{2}\int_\Omega \boldsymbol{c}\text{symm}\boldsymbol{\nabla u} \cdot \text{symm}\boldsymbol{\nabla u} \text{d}V + \frac{\gamma}{2}\int_\Omega |\text{skew}\boldsymbol{\nabla u} - \boldsymbol{\psi}|^2 \text{d}V - \int_\Omega \boldsymbol{f} \cdot \boldsymbol{u} \text{d}V + \text{Boundary Terms}. \quad (2.25)$$

It can be shown that for each of the elements implemented in this chapter, the patch test is passed for any $\gamma > 0$ [18]. However, the parameter γ is problem dependent [18, 21], and its sensitivity is detailed in this chapter.

Since not all of the elements resulting from the formulations just highlighted are implemented here, Figure 2.4 depicts the links between the various functionals in relation to this study. The functionals contained in the top row are those based on Reissner's work [40], and were shown to have stability issues in discrete form. They therefore do not form part of this investigation. Also, although recently Pimpinelli [20] proposed an assumed strain quadrilateral element with drilling degrees of freedom, based on a functional similar to $\tilde{H}_\gamma$, elements based on Hu-Washizu like functionals are beyond the scope of this study. The elements considered in this study are based on the functionals enclosed by the solid line. Details of the variational formulations and numerical implementations of these elements can be found in many references, including [18, 21, 43] and are therefore not repeated here.

2.5 Finite element interpolation

In this section, the finite element interpolations employed in the elements arising from the variational formulations pointed out in the foregoing are presented. For the sake of brevity,

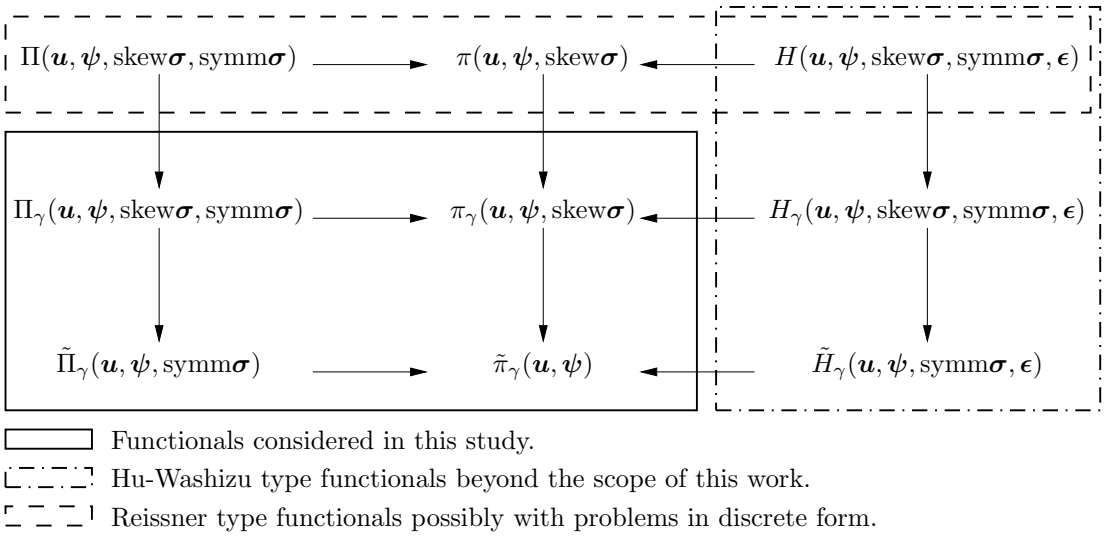

Figure 2.4: Applications of functionals proposed by Hughes and Brezzi in discrete form.

we refrain from giving the elemental stiffness matrices here, as they are easily derived through application of stationary principles to the functionals presented in the previous section.[4]

It is required that the three distinct independent interpolation fields arising from the translations, rotations and the assumed stress field are interpolated.[5] The standard element displacement gradient operators follow [43, 53].

Consider a 4-node quadrilateral element with degrees of freedom as depicted in Figure 2.5. The reference surface of the element is defined by

$$\boldsymbol{x} \;=\; \sum_{I=1}^{4} N_I^e(r,s)\boldsymbol{x}_I, \tag{2.26}$$

where $\boldsymbol{x}$ represents coordinates (x, y) and $N_I(r, s)$ are the isoparametric shape functions [60]

$$N_I^e(r,s) \;=\; \frac{1}{4}(1+r_I r)(1+s_I s)\;;\; I=1,2,3,4. \tag{2.27}$$

The independent rotation field is interpolated as a standard bilinear field over each element:

$$\theta_z \;\equiv\; \psi^h \;=\; \sum_e \sum_{I=1}^{4} N_I^e(r,s)\psi_i. \tag{2.28}$$

The in-plane displacement approximation is taken as an Allman-type interpolation

$$\begin{pmatrix} u_x \\ u_y \end{pmatrix} \;=\; \boldsymbol{u}^h \;=\; \sum_e \sum_{I=1}^{4} N_I^e(r,s)\boldsymbol{u}_I \;+\; \sum_e \sum_{I=5}^{8} NS_I^e(r,s)\frac{l_{JK}}{8}(\psi_K-\psi_J)\boldsymbol{n}_{JK}, \tag{2.29}$$

[4] Once again, these can be found in many references, including [21, 43, 52, 53].

[5] Since Hu-Washizu functionals are not considered, interpolation of strain or enhanced strain is not necessary.

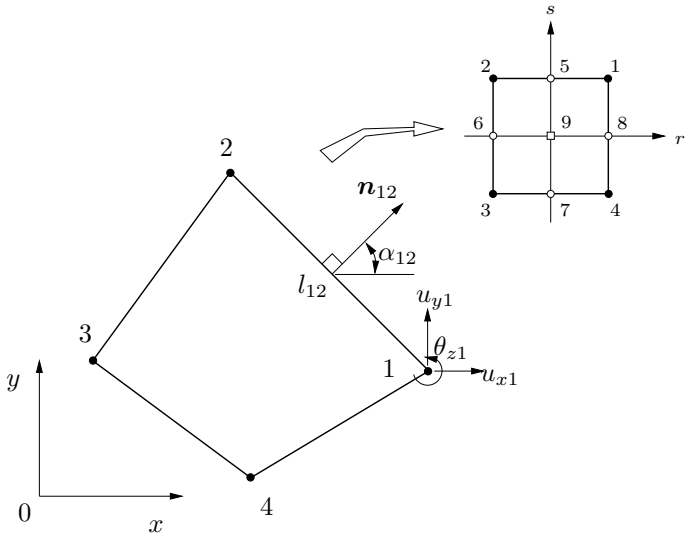

Figure 2.5: Four node element with drilling degrees of freedom.

where l_{JK} and $\boldsymbol{n}_{JK}$ are the length and the outward unit normal vector on the element side associated with the corner nodes J and K, i.e.

$$\boldsymbol{n}_{JK} \;=\; \left\{ \begin{array}{c} n_1 \\ n_2 \end{array} \right\} \;=\; \left\{ \begin{array}{c} \cos\alpha_{JK} \\ \sin\alpha_{JK} \end{array} \right\}, \tag{2.30}$$

and

$$l_{JK} \;=\; ((x_K - x_J)^2 + (y_K - y_J)^2)^{1/2}. \tag{2.31}$$

In the above, a FORTRAN-like definition of adjacent corner nodes is employed:

$$J \;=\; I - 4 \;;\quad K \;= \mathrm{mod}(I, 4) + 1. \tag{2.32}$$

In Equation (2.29) the serendipity shape functions are defined by

$$NS^e_I(r,s) \;=\; \frac{1}{2}(1 - r^2)(1 + s_I s) \;;\; I = 5, 7, \tag{2.33}$$

$$NS^e_I(r,s) \;=\; \frac{1}{2}(1 + r_I r)(1 - s^2) \;;\; I = 6, 8. \tag{2.34}$$

Employing matrix notation and defining

$$\mathrm{symm}\ \boldsymbol{\nabla} \boldsymbol{u}^e \;=\; \boldsymbol{B}^e_I \boldsymbol{u}_I \;+\; \boldsymbol{G}^e_I \psi_I, \tag{2.35}$$

where $\boldsymbol{u}_I$ and ψ_I are nodal values of the displacement and the rotation fields, respectively. The $\boldsymbol{B}^e_I$ matrix in Equation (2.35) has the standard form

$$\boldsymbol{B}^e_I \;=\; \left[\begin{array}{cc} N^e_{I,x} & 0 \\ 0 & N^e_{I,y} \\ N^e_{I,y} & N^e_{I,x} \end{array} \right] \;;\; I = 1, 2, 3, 4, \tag{2.36}$$

where $N_{I,x} = \frac{\partial N_I}{\partial x}$. The part of the displacement interpolation associated with the rotation defines

$$\boldsymbol{G}_I^e = \frac{1}{8}\begin{bmatrix} \left(l_{IJ}\cos\alpha_{IJ}NS^e_{L,x} - l_{IK}\cos\alpha_{IK}NS^e_{M,x}\right) \\ \left(l_{IJ}\sin\alpha_{IJ}NS^e_{L,y} - l_{IK}\sin\alpha_{IK}NS^e_{M,y}\right) \\ \left\{ \begin{array}{c} l_{IJ}\cos\alpha_{IJ}NS^e_{L,y} - l_{IK}\cos\alpha_{IK}NS^e_{M,y} \\ + \\ l_{IJ}\sin\alpha_{IJ}NS^e_{L,x} - l_{IK}\sin\alpha_{IK}NS^e_{M,x} \end{array} \right\} \end{bmatrix}, \tag{2.37}$$

where

$$I = 1,2,3,4;\ \ M = I+4;\ \ L = M - 1 + 4\text{int}(1/I);$$
$$K = \text{mod}(M,4) + 1;\ \ J = L - 4, \tag{2.38}$$

and

$$NS_{L,x} = \frac{\partial NS_L}{\partial x}.$$

Terms associated with the skew-symmetric part of the displacement gradient are now considered. Denoting

$$\text{skew}\ \boldsymbol{\nabla u}^e - \psi^e = \boldsymbol{b}_I^e \boldsymbol{u}_I + g_I^e \psi_I, \tag{2.39}$$

where

$$\boldsymbol{b}_I^e = < -\frac{1}{2}N^e_{I,y} \quad \frac{1}{2}N^e_{I,x} > ; \quad I = 1,2,3,4, \tag{2.40}$$

and

$$g_I^e = [-\frac{1}{16}(l_{IJ}\cos\alpha_{IJ}NS^e_{L,y} l_{IK}\cos\alpha_{IK}NS^e_{M,y})$$
$$+\frac{1}{16}(l_{IJ}\sin\alpha_{IJ}NS^e_{L,x} l_{IK}\sin\alpha_{IK}NS^e_{M,x}) - N_I^e] ; \quad I = 1,2,3,4, \tag{2.41}$$

with indices J, K, L, M again defined by (2.38)

For the assumed stress field, the global stresses are directly interpolated by the stress parameters β_i, i.e.

$$\text{symm}\ \boldsymbol{\sigma}^h = \sum_e \boldsymbol{P}^e \boldsymbol{\beta}^e, \tag{2.42}$$

where $\boldsymbol{P}^e$ is the interpolation matrix in terms of the local coordinates and $\boldsymbol{\beta}^e$ is the stress parameter vector. The stress field assumed in (2.42) may, without loss of generality, be expressed for an individual element as:

$$\text{symm}\ \boldsymbol{\sigma}^e = \boldsymbol{P\beta} = \text{symm}\ \boldsymbol{\sigma}_c^e + \text{symm}\ \boldsymbol{\sigma}_h^e = [\boldsymbol{I}_c\ \boldsymbol{P}_h]\left\{ \begin{array}{c} \boldsymbol{\beta}_c \\ \boldsymbol{\beta}_h \end{array} \right\}, \tag{2.43}$$

where the superscript e is dropped on $\boldsymbol{P}_*$ and $\boldsymbol{\beta}_*$ for reasons of clarity. In (2.43), $\boldsymbol{I}_c$ allows for the accommodation of constant stress states required to pass the patch test. The higher order stress field is represented by

$$\text{symm}\ \boldsymbol{\sigma}_h^e = \boldsymbol{P}_h\boldsymbol{\beta}_h = \boldsymbol{P}_{h2}\boldsymbol{\beta}_{h2} + \boldsymbol{P}_{h3}\boldsymbol{\beta}_{h3}, \tag{2.44}$$

where $\boldsymbol{P}_{h2}\boldsymbol{\beta}_{h2}$ and $\boldsymbol{P}_{h3}\boldsymbol{\beta}_{h3}$ are introduced for reasons of clarity. We select

$$\boldsymbol{P}_{h2}\boldsymbol{\beta}_{h2}+\boldsymbol{P}_{h3}\boldsymbol{\beta}_{h3} = \begin{bmatrix} \eta & 0 \\ 0 & \xi \\ 0 & 0 \end{bmatrix} \begin{Bmatrix} \beta_4 \\ \beta_5 \end{Bmatrix} + \begin{bmatrix} -\xi & 0 & \eta^2 \\ 0 & -\eta & -\xi^2 \\ \eta & \xi & 0 \end{bmatrix} \begin{Bmatrix} \beta_6 \\ \beta_7 \\ \beta_8 \end{Bmatrix}. \tag{2.45}$$

Combined with $\boldsymbol{I}_c$, $\boldsymbol{P}_{h2}$ yields the usual formulation for a 5-parameter stress field, as was for instance also used by Di and Ramm [61], for their 5β elements. $\boldsymbol{P}_{h3}$ represents the additional terms required for elements with drilling degrees of freedom. This formulation is similar to the unconstrained field used by Sze and Ghali [50]. However, (2.42) represents an unconstrained interpolation field, which is not necessarily optimal. Constraints may be enforced by a suitable transformation matrix (e.g. see [61]). Here, the rational constraints proposed by Pian and Sumihara [62] are opted for, viz.

$$\text{symm}\,\boldsymbol{\sigma}_h^e = \boldsymbol{P}_h\boldsymbol{\beta}_h = \boldsymbol{T}_0\boldsymbol{P}_{h2}\boldsymbol{\beta}_{h2}+\boldsymbol{T}_0\boldsymbol{P}_{h3}\boldsymbol{\beta}_{h3}, \tag{2.46}$$

with

$$\boldsymbol{T}_0 = \begin{bmatrix} a_1^2 & a_3^2 & 2a_1a_3 \\ b_1^2 & b_3^2 & 2b_1b_3 \\ a_1b_1 & a_3b_3 & a_1b_3+a_3b_1 \end{bmatrix}, \tag{2.47}$$

and

$$\begin{bmatrix} a_1 & b_1 \\ a_2 & b_2 \\ a_3 & b_3 \end{bmatrix} = \frac{1}{4}\begin{bmatrix} -1 & 1 & 1 & -1 \\ 1 & -1 & 1 & -1 \\ -1 & -1 & 1 & 1 \end{bmatrix} \begin{bmatrix} x_1 & y_1 \\ x_2 & y_2 \\ x_3 & y_3 \\ x_4 & y_4 \end{bmatrix}. \tag{2.48}$$

While normalized transformation of the higher order part of the stress field is probably more accurate [43], the rational approach of Pian and Sumihara is simpler, in particular if element equilibrium is enforced.

Finally, 9 stress parameters may also be used, even though this is one more than the optimal number of stress parameters. In this case, the higher order stress field becomes

$$\boldsymbol{P}_{h3}\boldsymbol{\beta}_{h3} = \begin{bmatrix} -\xi & 0 & \eta^2 & 0 \\ 0 & -\eta & 0 & -\xi^2 \\ \eta & \xi & 0 & 0 \end{bmatrix} \begin{Bmatrix} \beta_6 \\ \beta_7 \\ \beta_8 \\ \beta_9 \end{Bmatrix}. \tag{2.49}$$

2.6 Stability analysis

After Hughes and Brezzi, the simplest form of the functionals considered in Section 2.4, namely functional $\tilde{\pi}_\gamma(\boldsymbol{u},\boldsymbol{\psi})$ given by (2.25) is considered. The variational equation which results from variations on (2.25) is

$$\begin{aligned} 0 = \delta\tilde{\pi}_\gamma = &\int_\Omega \boldsymbol{c}\,\text{symm}\boldsymbol{\nabla}\boldsymbol{u}\cdot\text{symm}\boldsymbol{\nabla}\delta\boldsymbol{u}\mathrm{d}V \\ &+\gamma\int_\Omega(\text{skew}\boldsymbol{\nabla}\boldsymbol{u}-\boldsymbol{\psi})\cdot(\text{skew}\boldsymbol{\nabla}\delta\boldsymbol{u}-\delta\boldsymbol{\psi})\mathrm{d}V-\int_\Omega\boldsymbol{f}\cdot\delta\boldsymbol{u}\mathrm{d}V. \end{aligned} \tag{2.50}$$

Hughes and Brezzi then rewrite (2.50) as follows: Find $\{\boldsymbol{u}, \boldsymbol{\psi}\}$ such that

$$\boldsymbol{B}_\gamma(\boldsymbol{u}, \boldsymbol{\psi}; \delta\boldsymbol{u}, \delta\boldsymbol{\psi}) = \boldsymbol{f}(\{\delta\boldsymbol{u}, \delta\boldsymbol{\psi}\}), \tag{2.51}$$

for arbitrary variations $\delta\boldsymbol{u}$ and $\delta\boldsymbol{\psi}$, where $\boldsymbol{B}_\gamma(\boldsymbol{u}, \boldsymbol{\psi}; \delta\boldsymbol{u}, \delta\boldsymbol{\psi})$ is in symmetric bilinear form, and where $\boldsymbol{f}(\{\boldsymbol{v}, \boldsymbol{\omega}\})$ is continuous. It is now possible to prove that $\boldsymbol{B}_\gamma$ is U-elliptic [18], viz. there exists a constant $\eta_U > 0$, such that

$$\boldsymbol{B}_\gamma(\boldsymbol{u}, \boldsymbol{\psi}; \delta\boldsymbol{u}, \delta\boldsymbol{\psi}) \geq \eta_U ||\{\delta\boldsymbol{u}, \delta\boldsymbol{\psi}\}||_U^2, \ \forall \ \{\delta\boldsymbol{u}, \delta\boldsymbol{\psi}\} \in U, \tag{2.52}$$

where $U \equiv V \times W$, and V and W are appropriate spaces of displacement and rotation functions. For the Dirichlet problem and isotropy (see Hughes and Brezzi [18] for details), this results in

$$\gamma \leq \mu, \tag{2.53}$$

with μ the shear modulus. The equality or upper bound represented by (2.53) was selected by a number of authors. In Section 2.8, this bound is further reflected on from a numerical point of view. Incidentally, the numerical approach was already suggested by Hughes and Brezzi, who remark that 'numerical experimentation will be useful in finding optimal values for γ.'

2.7 Consistency and stability

It is well known that the elements with drilling DOFs considered herein all pass the patch test; they are also of adequate rank. Hence they are unconditionally convergent. This is true for any value of $\gamma > 0$ [18, 52].

This leads to the observation that the symmetry condition of the stress tensor should exactly be achieved for problems characterized by constant states of strain, viz. skew $\boldsymbol{\nabla u} - \boldsymbol{\psi} = 0$. Numerical experimentation reveals that this is, to machine precision, indeed the case for pure extension and pure shear patch tests, as well as the modified pure shear patch depicted in Figure 2.6.

2.8 Numerical experiments

In this section, numerical results for the elements highlighted in the foregoing are presented. The integration schemes employed on individual partition matrices are as given in [63]. The penalty matrix, relating displacements and in-plane rotations, is evaluated using a 1 point integration rule. The remaining partition stiffness terms are calculated using a 3×3 integration rule, although a reduced order (5 or 8 point) scheme could also be used. The following denotation is used:

- Q4X denotes drill elements without assumed stress interpolation. Unless otherwise stated, the mixed formulation, with functional represented by (2.22), is used.

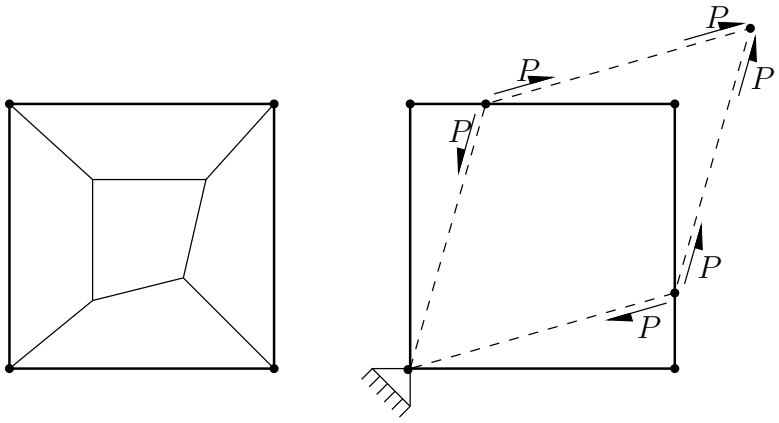

Figure 2.6: Modified shear patch test

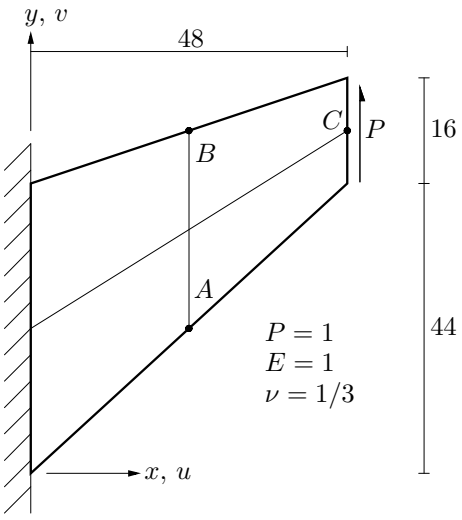

Figure 2.7: Cook's membrane

- 8β and 9β respectively indicates assumed stress drill elements with 8 and 9 stress interpolation parameters (see (2.45) and (2.49)). Unless otherwise stated, results are presented for the displacement formulation, this time represented by (2.24).

2.8.1 Cook's membrane

The popular swept and tapered cantilever beam subjected to a uniformly distributed tip load, as originally proposed by Cook, is depicted in Figure 2.7. Results as a function of parameter γ, are depicted in Figures 2.8 and 2.9, for respectively a 4×4 and a 32×32 mesh. At $\gamma = \mu$ there is a distinct change in slope of the beam tip displacement and rotation curves. The maximum value of skew$\boldsymbol{\sigma}$ over all elements, denoted τ_0 in the figures, is also reported (normalized with respect to it's value at $\gamma = \mu$). The value of τ_0 clearly increases sharply as γ increases above μ, and it is obvious that $\gamma \leq \mu$ is required. However, the equality is not necessarily optimal, $\gamma = \mu/10$, $\mu/100$, or even $\mu/1000$, may be more accurate.

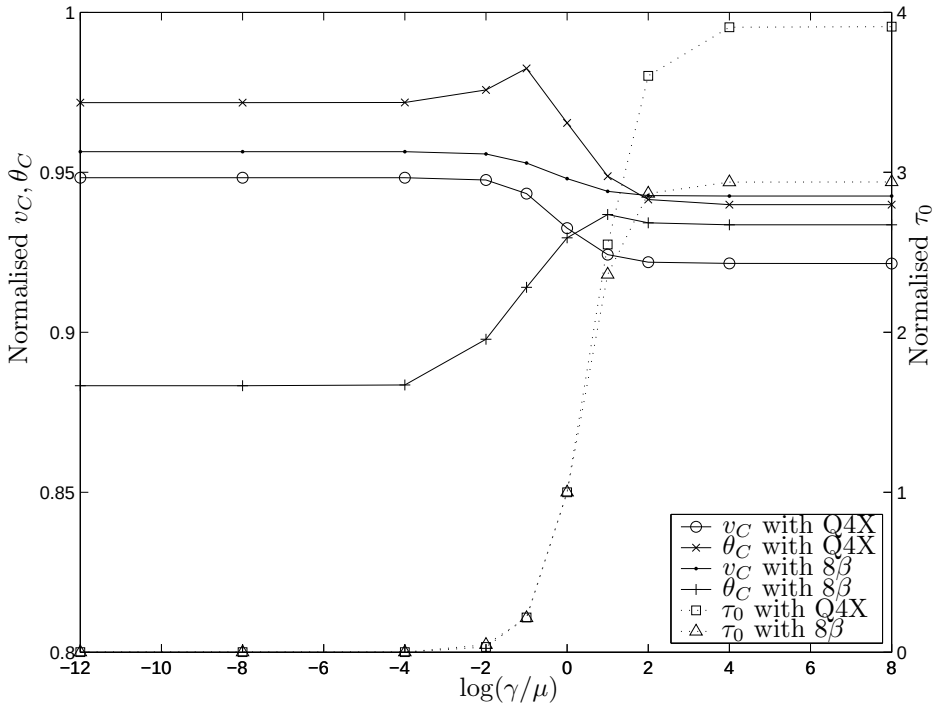

Figure 2.8: Cook's membrane: Effect of γ on displacement, rotation and skew $\boldsymbol{\sigma}$ for the 4×4 mesh

2.8.2 Cantilever beam subjected to end shear

A further popular test problem is the shear loaded cantilever beam depicted in Figure 2.10. For the penalty γ, a similar trend is observed to that of Cook's membrane above (Figure 2.11). Again the effect of γ is not nearly as pronounced on rotation and displacement as on the skew part of the stress tensor, and values of $\gamma < \mu$ seem suitable, rather than $\gamma = \mu$.

2.8.3 Orthotropic membrane cantilever

Next the orthotropic cantilever, depicted in Figure 2.12, is considered. Even though only one layer is considered, the strain variation becomes quite complex for non-zero ply angle arrangements [43].

Numerical results for the parameter γ are presented in Figures 2.13 and 2.14, for a ply arrangement of respectively 0 and 30 degrees. The displacement and rotation results are normalized with respect to solutions computed using a refined finite element mesh. For 0 degrees, the displacement based and stress based elements are almost identical (which is not surprising, since the mesh is regular).

For the 30 degrees orientation, the displacement and rotation prediction of the stress based element is superior, while this element also predicts a lower value of skew$\boldsymbol{\sigma}$. On the scale of the graphs, it is not very obvious how sensitive the displacement results are to the value of γ, however, results may differ by some 5% as a result of different values of γ. For this

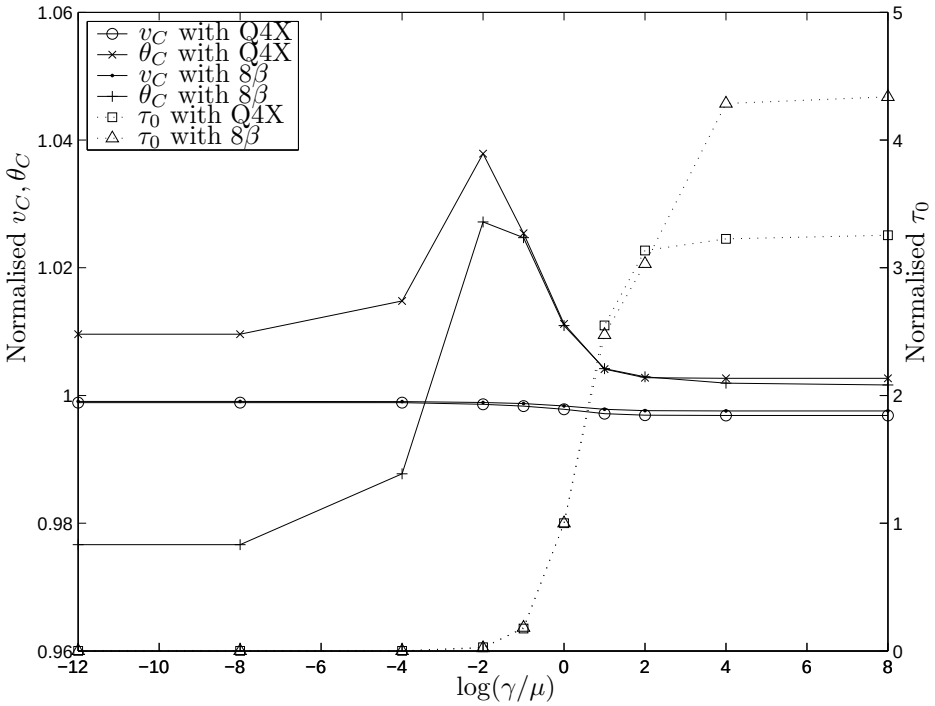

Figure 2.9: Cook's membrane: Effect of γ on displacement, rotation and skew $\boldsymbol{\sigma}$ for the 32×32 mesh

problem, it is clear that $\gamma = \mu_{12}$ is no longer ideal; values of $\gamma = \mu_{12}/10^3$ or even $\mu_{12}/10^4$ seem superior.

For the irregular distorted mesh, results are depicted in Figure 2.15. While the mesh distortion is probably a bit extreme, the effect of γ is illustrated clearly. Element performance starts to degrade from roughly $\gamma = \mu/10000$, and the degradation is quite pronounced. For this problem, the loss in accuracy of displacements, rotations as well as skew$\boldsymbol{\sigma}$ due to high values of γ is significant.

2.9 Conclusions

In this chapter, the formulation of finite elements with drilling DOFs has briefly been outlined. Thereafter, a numerical investigation into the effect of the penalty parameter in elements with drilling degrees of freedom, for which the stress tensor $\boldsymbol{\sigma}$ is not *a priori* assumed to be symmetric, has been presented. The parameter under investigation is γ, which relates the in-plane translations to the rotations.

Rather than only reporting on the quantitative influence of the penalty parameter γ on measures like displacement, rotation and stress, the skewness of the nonsymmetric part of the stress tensor $\boldsymbol{\sigma}$, is directly assessed. Results are presented for both isotropic and orthotropic constitutive relationships.

It is shown that, in general, values smaller than $\gamma = \mu$, with μ the shear modulus, are

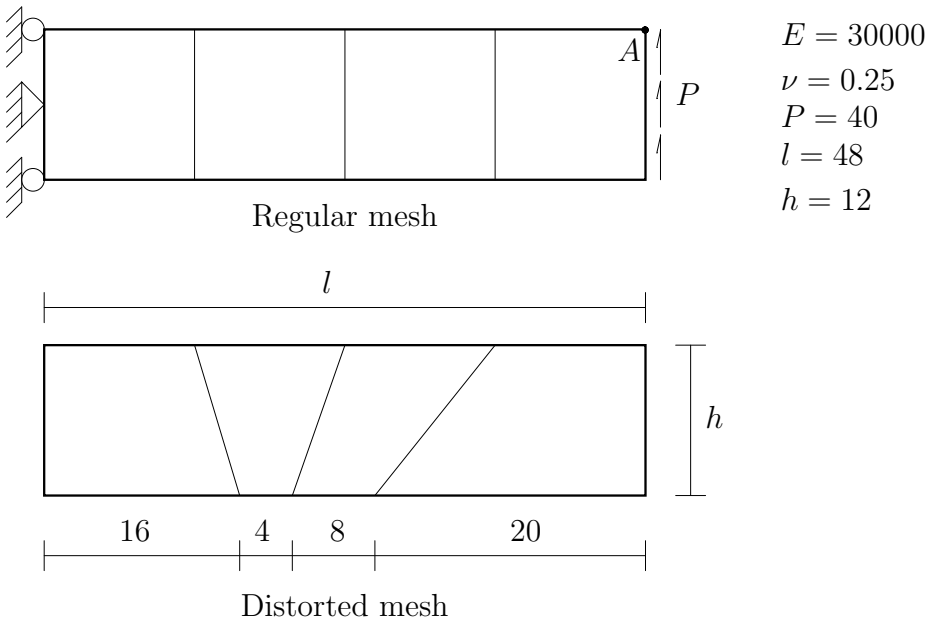

Figure 2.10: Cantilever beam under shear load

desirable, even though the formulation is convergent for all values of γ. Values of $\gamma/\mu = 10^{-1}$ or 10^{-2} seem to result in accurate solutions. However, in implementing elements with drilling degrees of freedom based on the procedure suggested by Hughes and Brezzi [18], the skewness of the nonsymmetric part of the stress tensor $\boldsymbol{\sigma}$, may directly be used to quantitatively assess the validity of selected values of γ.

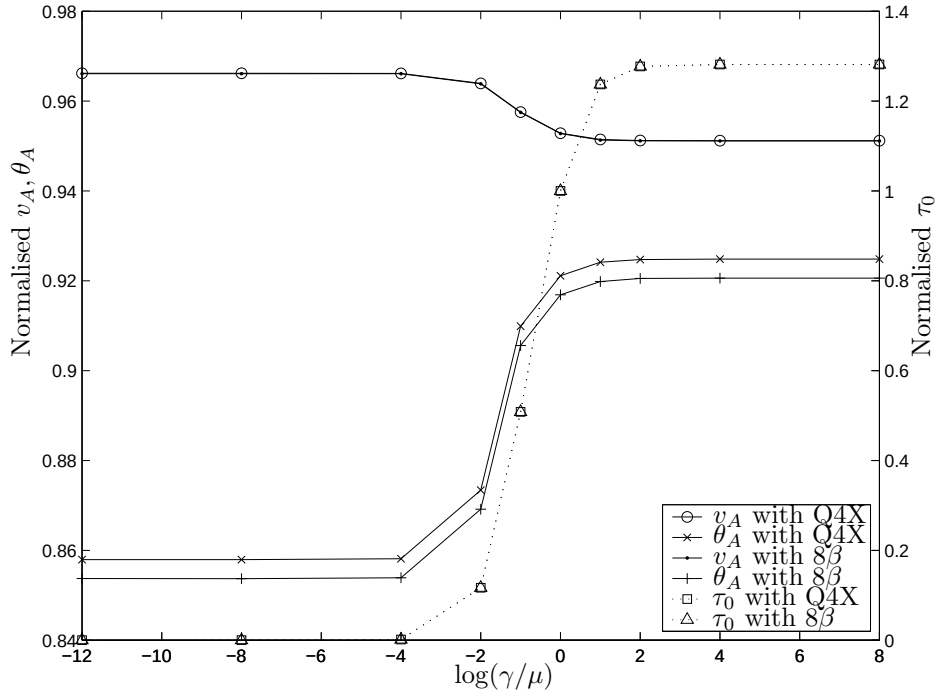

Figure 2.11: Cantilever beam: Effect of γ on tip displacement and skew $\boldsymbol{\sigma}$

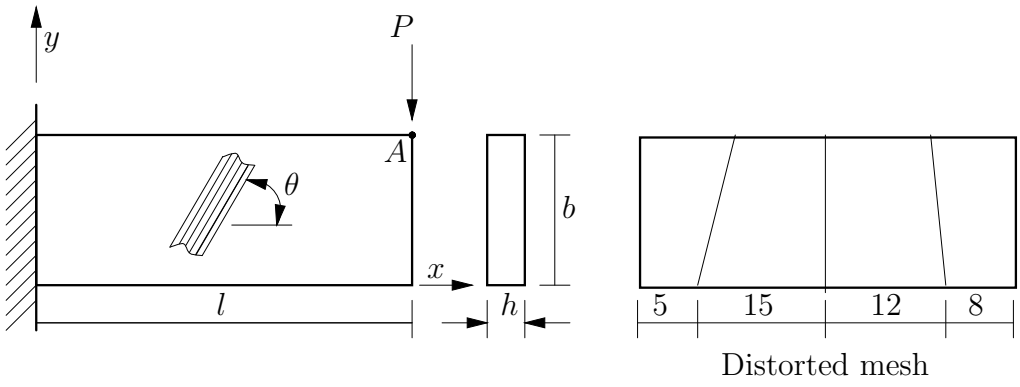

Figure 2.12: Orthotropic membrane cantilever

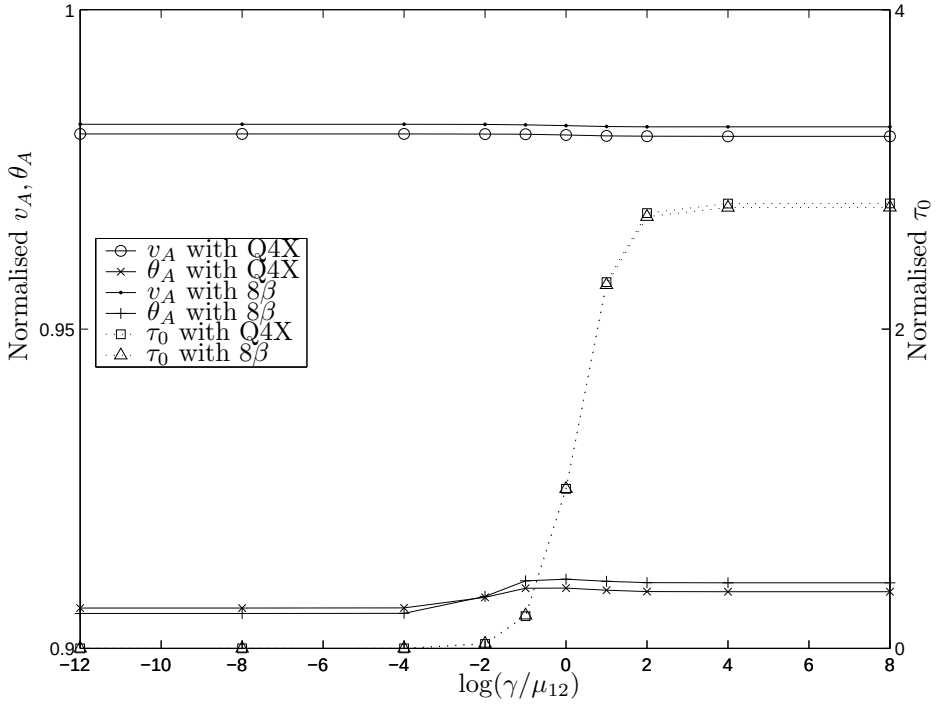

Figure 2.13: Orthotropic membrane cantilever: Effect of γ for a 0 degree ply arrangement (regular mesh)

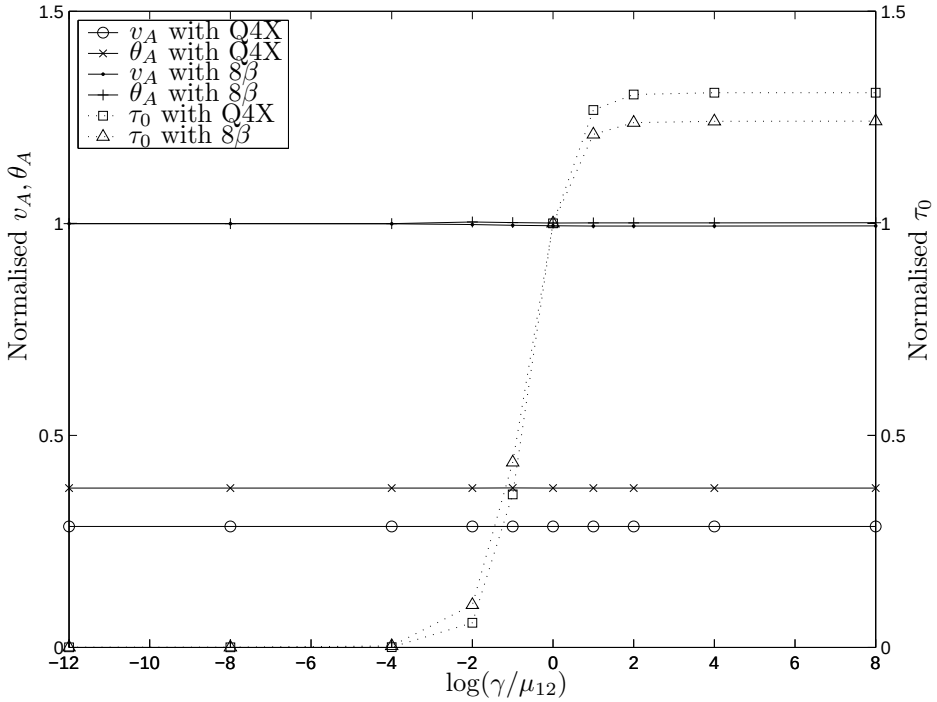

Figure 2.14: Orthotropic membrane cantilever: Effect of γ for a 30 degree ply arrangement (regular mesh)

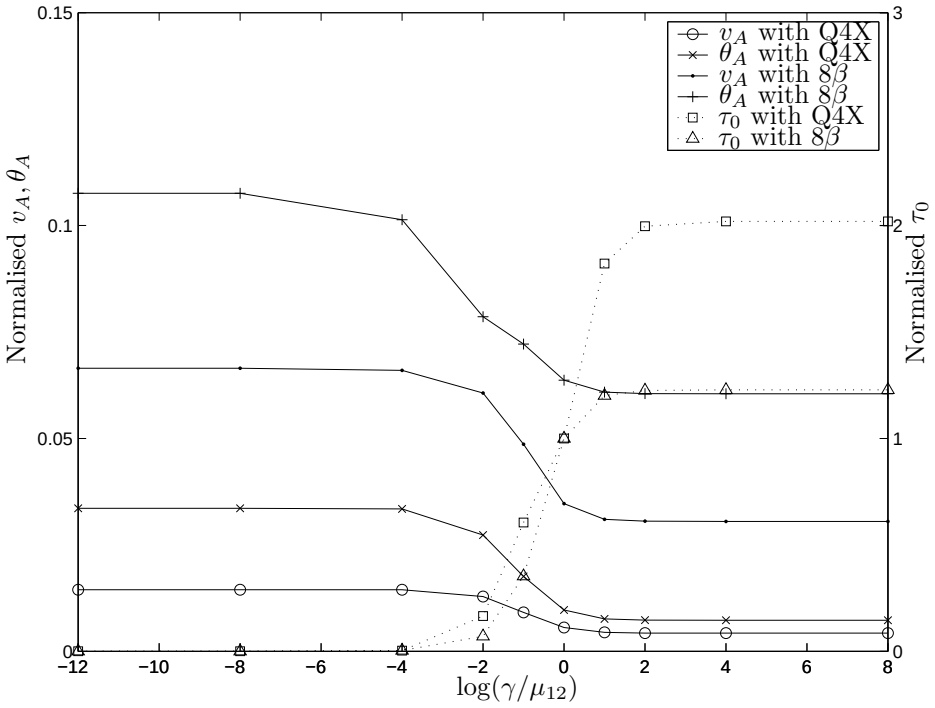

Figure 2.15: Orthotropic membrane cantilever: Effect of γ for a 30 degree ply arrangement (distorted mesh)

Chapter 3

Piezoelectric elements with drilling degrees of freedom

3.1 Summary

In this chapter, several new planar four node piezoelectric elements with drilling degrees of freedom are presented. Firstly, two families of variational formulations accounting for piezoelectricity and in-plane rotations are derived. The first family retains the skew-symmetric part of the stress tensor, while in the second, the skew part of stress is eliminated from the functional. The performance of the finite elements derived from the variational formulations presented in this chapter are then investigated. The resulting new elements are shown to be accurate and robust in comparison with a number of existing elements, for several benchmark test problems.

3.1.1 Another brief word on notation

As explained in Section 2.1.1, the symbolic designation traditionally used by researchers working in piezoelectric finite element development, e.g. see [64, 65, 66] is now reverted to. In particular, the symbols used to denote mechanical quantities and properties are different to those employed in Chapter 2. Once again, the symbols are defined during the course of the chapter.

We continue to employ the same tensor notation as that introduced in Chapter 2, which is similar to that employed by, for example, Pimpinelli [20] and Cannarozzi and Ubertini [66].

3.2 Introduction

In recent years, the use of smart materials has become widespread and almost commonplace. The technology employed in piezoelectric applications in particular, has reached a mature level, and piezoelectric materials are frequently used in engineering applications.

Piezoelectric materials transfer electric energy to mechanical energy and *vice versa*, and can therefore be used as either actuators or sensors, or both. Applications include ultrasonic transducers for sonar and medical purposes, compact ultrasonic piezoelectric motors, structural monitoring and/or active damping elements, and even ignition systems.

Analytical closed-form solutions to problems involving piezoelectric materials are often difficult to compute, unless geometries and boundary conditions are relatively simple, see for example Heyliger [67] and Kapuria *et al.* [68]. A general numerical method for the solution of piezoelectric problems is therefore essential. (Analytical solutions are, however, very useful as benchmark problems.)

The finite element method has become a standard modelling utility for various physical processes, including piezoelectricity. Development of piezoelectric finite elements has progressed significantly since the early paper of Allik and Hughes [69]. In fact, Benjeddou [70] presented a survey article in which over 100 recent papers from the open literature are reviewed, indicating the research interest in the field.

The original implementation of Allik and Hughes, and many of the finite elements since, (see Benjeddou for examples), have been based on formulations interpolating for only kinematic–like variables, i.e. displacement and electric potential. These elements are often stiff, inaccurate and sensitive to mesh distortion. To alleviate these problems, mixed and hybrid variational formulations have been developed (see for example Yang [71]), with original contributions in variational formulations for piezoelectric media credited to EerNisse and Holland [72, 73]. Various hybrid and mixed finite elements have since been developed, with notable contributions by Cannarozzi and Ubertini [66] and Sze and co-workers [64, 65, 74, 75, 76].

Independent of the development of piezoelectric finite elements, many advances have been made in the development of elastic finite elements. One of the significant contributions has been the addition of in-plane rotations, or drilling degrees of freedom (DOFs). Drilling DOFs are particularly important in shell elements, since the result is a shell element with six DOFs per node, which allows for the modelling of beam-slab connections and folded plates. An introduction into, and a brief history of, elements with drilling DOFs and their variational formulation can be found in Chapter 2, and will therefore not be repeated here.

The aim of this chapter is to combine the theory, developed for elastic elements with drilling DOFs, with some recent advances in piezoelectric finite element technology. The result is two new families of accurate, piezoelectric finite elements with drilling DOFs.

We endeavour to, not only improve on element accuracy, but importantly, improve on the modelling capabilities of existing piezoelectric finite elements. In fact, the piezoelectric elements developed herein are used in a topology optimization environment, together with elastic elements possessing drilling DOFs, see Chapter 5 and [77]. Their accuracy can also be exploited in fracture analyses. Aside from the improved accuracy, these elements can be employed to calculate through-thickness phenomena in thick piezoelectric shells. The variational formulations can also be used to generate three dimensional solid elements with drilling DOFs. These solid elements would possess three displacement, three rotational and one potential DOF per node.

The remainder of this chapter is set out as follows. In Section 3.3, the equations governing the linear electroelastic problem are presented. Section 3.4 introduces a number of new

variational formulations accounting for piezoelectricity and in-plane rotations. In Section 3.5 the interpolations used in the finite element implementations are briefly highlighted. Section 3.6 details the finite element implementation of our variational formulations. The partitioned submatrices arising from the finite element implementations are presented in Section 3.7. Section 3.8 contains the results of a numerical evaluation of the new elements. Finally, in Section 3.9 some closing remarks are offered.

3.3 Governing equations

In this section, the equations governing the linear electroelastic problem are presented in strong form. Let $\bar{\Omega}$ be a closed and bounded domain occupied by a body in three dimensional space. The interior part of $\bar{\Omega}$ is denoted by Ω and it's boundary by $\partial\Omega$, $\Omega \cup \partial\Omega = \bar{\Omega}$. The measure of Ω is V and the measure of $\partial\Omega$ is S. $\mathcal{V}$ is the vector space associated with the Euclidean point space and $\mathcal{L}$ the space of all linear applications of $\mathcal{V}$ into $\mathcal{V}$, which possesses inner product $\boldsymbol{A} \cdot \boldsymbol{B} = \mathrm{tr}(\boldsymbol{A}^t\boldsymbol{B})$, $\boldsymbol{A}, \boldsymbol{B} \in \mathcal{L}$ and $\boldsymbol{A}^t$ the transpose of $\boldsymbol{A}$ (see Pimpinelli [20]). Reference will also be made to subsets of $\mathcal{L}$, namely $\mathcal{S}$ and $\mathcal{W}$ which contain, respectively symmetric and skew-symmetric tensors in $\mathcal{L}$.

The boundary $\partial\Omega$, is split into four parts, $\partial\Omega_u$, $\partial\Omega_t$, $\partial\Omega_\phi$ and $\partial\Omega_d$ such that $\partial\Omega_u \cup \partial\Omega_t = \partial\Omega_\phi \cup \partial\Omega_d = \partial\Omega$ and $\partial\Omega_u \cap \partial\Omega_t = \partial\Omega_\phi \cap \partial\Omega_d = \emptyset$. On $\partial\Omega_u$ displacements $\bar{\boldsymbol{u}}$ are prescribed, while on $\partial\Omega_t$ the traction $\bar{\boldsymbol{t}}$ is prescribed. Similarly, on $\partial\Omega_\phi$ the prescribed potentials are $\bar{\phi}$ and on $\partial\Omega_d$ the density of the electric charge $\bar{d}$ is prescribed.

The Euclidean decomposition of second-rank tensors is frequently employed, e.g.

$$\boldsymbol{T} = \mathrm{symm}\boldsymbol{T} + \mathrm{skew}\boldsymbol{T}, \tag{3.1}$$

where

$$\mathrm{symm}\boldsymbol{T} = \frac{1}{2}(\boldsymbol{T} + \boldsymbol{T}^t), \tag{3.2}$$

$$\mathrm{skew}\boldsymbol{T} = \frac{1}{2}(\boldsymbol{T} - \boldsymbol{T}^t). \tag{3.3}$$

The linear electroelastic problem is governed by the following conditions at all points $\boldsymbol{x} \in \bar{\Omega}$.

3.3.1 Constitutive equations

There exist four equivalent versions of the electroelastic constitutive equations, depending on the choice of independent variables (see for example Ikeda [78]). The constitutive equations, in terms of strain and electric field are:

$$\begin{aligned} \boldsymbol{T} &= \boldsymbol{c}_E\boldsymbol{S} - \boldsymbol{e}^t\boldsymbol{E}, \\ \boldsymbol{D} &= \boldsymbol{e}\boldsymbol{S} + \boldsymbol{\epsilon}_S\boldsymbol{E}, \end{aligned} \tag{3.4}$$

where $\boldsymbol{T}$ and $\boldsymbol{S}$ are the stress and strain tensors, $\boldsymbol{D}$ is the electric flux density, also referred to as electric displacement (see for example Wu *et al.* [65]), and $\boldsymbol{E}$ denotes the electric

field. Furthermore, $\boldsymbol{c}_E$ is a fourth order tensor of elastic stiffness, measured at constant electric field as indicated by the subscript 'E'. $\boldsymbol{\epsilon}_S$ is the second order permittivity tensor at constant strain, and $\boldsymbol{e}$ is a third order electroelastic, or piezoelectric, coupling tensor. Both $\boldsymbol{c}_E$ and $\boldsymbol{\epsilon}_S$ are symmetric and positive definite. As described by Cannarozzi and Ubertini [66], $\boldsymbol{e}$ is such that the product $\boldsymbol{e}^t\boldsymbol{a}$ is a second order symmetric tensor for each vector $\boldsymbol{a}$, with $\boldsymbol{e}^t$ defined as $\boldsymbol{A}\cdot\boldsymbol{e}^t\boldsymbol{a} = \boldsymbol{e}\boldsymbol{A}\cdot\boldsymbol{a}$, and $\boldsymbol{A}$ a symmetric second order tensor. Incidentally, the constitutive relations in terms of strain and electric field were used in the original finite element implementations [69].

Since the derivation of the other forms of the constitutive equations, through Legendre transformation, are well known (see for example [66, 78]) they will simply be stated here without further elaboration.

In terms of strain $\boldsymbol{S}$ and electric flux density $\boldsymbol{D}$, the relations are

$$\begin{aligned} \boldsymbol{T} &= \boldsymbol{c}_D\boldsymbol{S} - \boldsymbol{h}^t\boldsymbol{D}, \\ \boldsymbol{E} &= -\boldsymbol{h}\boldsymbol{S} + \boldsymbol{\chi}_S\boldsymbol{D}, \end{aligned} \tag{3.5}$$

and the constitutive terms are computed as

$$\boldsymbol{c}_D = \boldsymbol{c}_E + \boldsymbol{e}^t\boldsymbol{\epsilon}_S^{-1}\boldsymbol{e}, \quad \boldsymbol{h} = \boldsymbol{\epsilon}_S^{-1}\boldsymbol{e}, \quad \boldsymbol{\chi}_S = \boldsymbol{\epsilon}_S^{-1}. \tag{3.6}$$

Rewriting in terms of stress $\boldsymbol{T}$ and electric field $\boldsymbol{E}$, get

$$\begin{aligned} \boldsymbol{S} &= \boldsymbol{s}_E\boldsymbol{T} + \boldsymbol{d}^t\boldsymbol{E}, \\ \boldsymbol{D} &= \boldsymbol{d}\boldsymbol{T} + \boldsymbol{\epsilon}_T\boldsymbol{E}, \end{aligned} \tag{3.7}$$

with

$$\boldsymbol{s}_E = \boldsymbol{c}_E^{-1}, \quad \boldsymbol{d} = \boldsymbol{e}\boldsymbol{c}_E^{-1}, \quad \boldsymbol{\epsilon}_T = \boldsymbol{\epsilon}_S + \boldsymbol{e}\boldsymbol{c}_E^{-1}\boldsymbol{e}^t. \tag{3.8}$$

Finally, with stress $\boldsymbol{T}$ and electric flux density $\boldsymbol{D}$ selected as independent variables, the result is

$$\begin{aligned} \boldsymbol{S} &= \boldsymbol{s}_D\boldsymbol{T} + \boldsymbol{g}^t\boldsymbol{D}, \\ \boldsymbol{E} &= -\boldsymbol{g}\boldsymbol{T} + \boldsymbol{\chi}_T\boldsymbol{D}, \end{aligned} \tag{3.9}$$

with

$$\boldsymbol{s}_D = (\boldsymbol{c}_E + \boldsymbol{e}^t\boldsymbol{\epsilon}_S^{-1}\boldsymbol{e})^{-1}, \quad \boldsymbol{g} = \boldsymbol{\epsilon}_S^{-1}\boldsymbol{e}\boldsymbol{s}_D, \quad \boldsymbol{\chi}_T = \boldsymbol{\epsilon}_S^{-1} - \boldsymbol{\epsilon}_S^{-1}\boldsymbol{e}\boldsymbol{s}_D\boldsymbol{e}^t\boldsymbol{\epsilon}_S^{-1}. \tag{3.10}$$

The tensors $\boldsymbol{c}_D$, $\boldsymbol{s}_E$, $\boldsymbol{s}_D$, $\boldsymbol{\chi}_S$, $\boldsymbol{\chi}_T$ and $\boldsymbol{\epsilon}_T$ are all symmetric and positive definite, and $\boldsymbol{h}$, $\boldsymbol{d}$ and $\boldsymbol{g}$ are third order tensors with the same properties as $\boldsymbol{e}$. In the presentation of the constitutive equations a condensed notation, assuming symmetric stress and strain tensors is used for the sake of clarity. That is to say, in (3.4), (3.5), (3.7) and (3.9), $\boldsymbol{T} \equiv \text{symm}\boldsymbol{T}$ and $\boldsymbol{S} \equiv \text{symm}\boldsymbol{S}$. This is of importance, since the stress tensor in the formulations to follow are not *a priori* assumed to be symmetric.

3.3.2 Compatibility conditions

The strain-displacement and electric field-potential relationships, together with the displacement and electric potential boundary conditions are, respectively

$$\boldsymbol{S} = \text{symm}\boldsymbol{\nabla u} \quad \text{in } \Omega, \tag{3.11}$$
$$\boldsymbol{E} = -\nabla\phi \quad \text{in } \Omega, \tag{3.12}$$
$$\boldsymbol{u} = \bar{\boldsymbol{u}} \quad \text{on } \partial\Omega_u, \tag{3.13}$$
$$\phi = \bar{\phi} \quad \text{on } \partial\Omega_\phi, \tag{3.14}$$

where $\boldsymbol{u}$ is the displacement vector field, and ϕ represents the scalar electric potential field.

3.3.3 Equilibrium conditions

The static force equilibrium equations and Gauss's Law in differential form, together with the boundary conditions, are given by:

$$\text{div}\boldsymbol{T} + \boldsymbol{f} = \boldsymbol{0} \quad \text{in } \Omega, \tag{3.15}$$
$$\text{div}\boldsymbol{D} - q = 0 \quad \text{in } \Omega, \tag{3.16}$$
$$\text{symm}\boldsymbol{T}\,\boldsymbol{n} = \bar{\boldsymbol{t}} \quad \text{on } \partial\Omega_t, \tag{3.17}$$
$$\boldsymbol{D}\cdot\boldsymbol{n} = -\bar{d} \quad \text{on } \partial\Omega_d, \tag{3.18}$$

where $\boldsymbol{f}$ is a distributed body force, q is a distributed electric charge in Ω, and $\boldsymbol{n}$ is the unit outward normal vector on $\partial\Omega$. Usually q is taken as zero [71], but for completeness it will be included in the presentation to follow.

3.3.4 Rotational momentum balance conditions and definition of infinitesimal rotation

In the current formulation, the stress tensor $\boldsymbol{T}$ is not *a priori* assumed to be symmetric, and in-plane rotations are included. The following two additional conditions need to be satisfied:

$$\text{skew}\boldsymbol{T} = \boldsymbol{0} \quad \text{in } \Omega, \tag{3.19}$$
$$\boldsymbol{\psi} = \text{skew}\boldsymbol{\nabla u} \quad \text{in } \Omega, \tag{3.20}$$

where (3.19) represents the rotational momentum balance conditions and (3.20) is the definition of infinitesimal rotations in terms of displacement gradient.

3.4 Variational formulation

Hughes and Brezzi [18] presented a general framework within which to construct variational formulations for problems which include rotational freedom. This framework is outlined in

Section 2.4. The most general type is their Hu-Washizu-like variational formulation accounting for rotations and nonsymmetric stress tensors. The variational framework of Hughes and Brezzi is now generalised to account for the piezoelectric effect.

In the functionals to follow, unless otherwise stated, $\boldsymbol{u}, \phi, \boldsymbol{E}$ and $\boldsymbol{D}$ are the displacement, electric potential, electric field and electric flux density fields, respectively. The nonsymmetric stress tensor is denoted $\boldsymbol{T} \in \mathcal{L}$. The skew-symmetric infinitesimal spin or rotation tensor is $\boldsymbol{\psi} \in \mathcal{W}$, and $\boldsymbol{S} \in \mathcal{S}$ is the symmetric strain tensor. Where applicable, they are sufficiently regular and square integrable functions of $\boldsymbol{x}$. In particular, the rotations $\boldsymbol{\psi}$, strains $\boldsymbol{S}$, stresses $\boldsymbol{T}$, electric field $\boldsymbol{E}$, electric flux density $\boldsymbol{D}$, as well as the generalised derivatives $\boldsymbol{\nabla u}$ and $\boldsymbol{\nabla}\phi$ belong to the space of square integrable functions over Ω.

3.4.1 Hu-Washizu-like variational formulations

A Hu-Washizu-like variational formulation is now proposed. It is also shown how this leads to a Hellinger-Reissner-like functional, as well as functionals in an irreducible form. The aim is not to present a rigorous mathematical study of the presented formulations. Rather, in the latter part of this chapter, a numerical study of the discrete finite element implementation is presented.

Two formulation families are proposed. The first, designated here as M-Type, retains the skew-symmetric part of the stress tensor. Since part of the stress tensor is always retained, even in its simplest or irreducible form, M-Type functionals will result in a *mixed* formulation, even in the 'irreducible' form. In the second family, denoted K-Type, the skew-symmetric part of stress is eliminated. The result is an irreducible form which requires only *kinematic*–like interpolations, i.e. displacement and electric potential.

M-Type formulation based on functional Π^H_M

The following Hu-Washizu-like functional is proposed:

$$\begin{aligned}\Pi^H_M(\boldsymbol{u}, \boldsymbol{\psi}, \mathrm{symm}\boldsymbol{T}, \mathrm{skew}\boldsymbol{T}, \boldsymbol{S}, \phi, \boldsymbol{D}, \boldsymbol{E}) = \frac{1}{2}\int_\Omega \boldsymbol{c}_E\ \boldsymbol{S}\cdot\boldsymbol{S}\,\mathrm{d}V - \int_\Omega \boldsymbol{e}\ \boldsymbol{S}\cdot\boldsymbol{E}\,\mathrm{d}V \\ - \frac{1}{2}\int_\Omega \boldsymbol{\epsilon}_S\ \boldsymbol{E}\cdot\boldsymbol{E}\,\mathrm{d}V + \int_\Omega (\mathrm{symm}\boldsymbol{\nabla u} - \boldsymbol{S})\cdot\mathrm{symm}\boldsymbol{T}\,\mathrm{d}V + \int_\Omega (\mathrm{skew}\boldsymbol{\nabla u} - \boldsymbol{\psi})\cdot\mathrm{skew}\boldsymbol{T}\,\mathrm{d}V \\ + \int_\Omega (\boldsymbol{\nabla}\phi + \boldsymbol{E})\cdot\boldsymbol{D}\,\mathrm{d}V - \frac{1}{2}\gamma^{-1}\int_\Omega |\mathrm{skew}\boldsymbol{T}|^2\,\mathrm{d}V - \int_\Omega \boldsymbol{f}\cdot\boldsymbol{u}\,\mathrm{d}V + \int_\Omega q\,\phi\,\mathrm{d}V \\ - \int_{\partial\Omega_t} \bar{\boldsymbol{t}}\cdot\boldsymbol{u}\,\mathrm{d}S + \int_{\partial\Omega_d} \bar{d}\,\phi\,\mathrm{d}S - \int_{\partial\Omega_u} (\boldsymbol{u}-\bar{\boldsymbol{u}})\cdot(\boldsymbol{T}\,\boldsymbol{n})\,\mathrm{d}S - \int_{\partial\Omega_\phi} (\phi-\bar{\phi})(\boldsymbol{D}\cdot\boldsymbol{n})\,\mathrm{d}S,\end{aligned} \tag{3.21}$$

where the subscript 'M' emphasises that the functional is of M-type and the superscript 'H' that it is a Hu-Washizu-like functional. The term $\frac{1}{2}\gamma^{-1}\int_\Omega |\mathrm{skew}\boldsymbol{T}|^2\,\mathrm{d}V$ was shown to preserve the ellipticity of the discrete problem in linear elastostatics [18]. In (3.21), the term $\boldsymbol{Tn}$ in the boundary term on $\partial\Omega_u$ was found to be the Lagrange multiplier which enforces

the prescribed displacements, where $\boldsymbol{T} \equiv \text{symm}\boldsymbol{T} + \text{skew}\boldsymbol{T}$. The condition of stationarity gives rise to the following variational equation:

$$\begin{aligned}
\delta\Pi_M^H = 0 = &\int_\Omega \boldsymbol{c}_E\boldsymbol{S}\cdot\delta\boldsymbol{S}\,\mathrm{d}V - \int_\Omega \boldsymbol{e}\boldsymbol{S}\cdot\delta\boldsymbol{E}\,\mathrm{d}V - \int_\Omega \boldsymbol{e}^t\boldsymbol{E}\cdot\delta\boldsymbol{S}\,\mathrm{d}V - \int_\Omega \boldsymbol{\epsilon}_S\boldsymbol{E}\cdot\delta\boldsymbol{E}\,\mathrm{d}V \\
&+ \int_\Omega (\text{symm}\boldsymbol{\nabla}\boldsymbol{u} - \boldsymbol{S})\cdot\text{symm}\delta\boldsymbol{T}\,\mathrm{d}V + \int_\Omega \text{symm}\boldsymbol{T}\cdot\text{symm}\boldsymbol{\nabla}\delta\boldsymbol{u} - \text{symm}\boldsymbol{T}\cdot\delta\boldsymbol{S}\,\mathrm{d}V \\
&+ \int_\Omega (\text{skew}\boldsymbol{\nabla}\boldsymbol{u} - \boldsymbol{\psi})\cdot\text{skew}\delta\boldsymbol{T}\,\mathrm{d}V + \int_\Omega \text{skew}\boldsymbol{T}\cdot\text{skew}\boldsymbol{\nabla}\delta\boldsymbol{u} - \text{skew}\boldsymbol{T}\cdot\delta\boldsymbol{\psi}\,\mathrm{d}V \\
&+ \int_\Omega (\boldsymbol{\nabla}\phi + \boldsymbol{E})\cdot\delta\boldsymbol{D}\,\mathrm{d}V + \int_\Omega \boldsymbol{D}\cdot\boldsymbol{\nabla}\delta\phi + \boldsymbol{D}\cdot\delta\boldsymbol{E}\,\mathrm{d}V - \int_\Omega \gamma^{-1}\text{skew}\boldsymbol{T}\cdot\text{skew}\delta\boldsymbol{T}\,\mathrm{d}V \\
&- \int_\Omega \boldsymbol{f}\cdot\delta\boldsymbol{u}\,\mathrm{d}V + \int_\Omega q\delta\phi\,\mathrm{d}V - \int_{\partial\Omega_t} \bar{\boldsymbol{t}}\cdot\delta\boldsymbol{u}\,\mathrm{dS} + \int_{\partial\Omega_d} \bar{d}\delta\phi\,\mathrm{dS} \\
&- \int_{\partial\Omega_u} [(\boldsymbol{u} - \bar{\boldsymbol{u}})\cdot(\delta\boldsymbol{T}\boldsymbol{n}) - (\boldsymbol{T}\boldsymbol{n})\cdot\delta\boldsymbol{u}]\,\mathrm{dS} \\
&- \int_{\partial\Omega_\phi} \left[(\phi - \bar{\phi})(\delta\boldsymbol{D}\cdot\boldsymbol{n}) - (\boldsymbol{D}\cdot\boldsymbol{n})\delta\phi\right]\,\mathrm{dS}.
\end{aligned} \tag{3.22}$$

Applying the Gauss-Green identities, given by

$$\int_\Omega \boldsymbol{u}\cdot\text{div}\boldsymbol{T}\,\mathrm{d}V = -\int_\Omega \boldsymbol{T}\cdot\boldsymbol{\nabla}\boldsymbol{u}\,\mathrm{d}V + \int_{\partial\Omega} \boldsymbol{u}\cdot\boldsymbol{T}\boldsymbol{n}\,\mathrm{dS} \tag{3.23}$$

$$\int_\Omega \phi\,\text{div}\boldsymbol{D}\,\mathrm{d}V = -\int_\Omega \boldsymbol{D}\cdot\boldsymbol{\nabla}\phi\,\mathrm{d}V + \int_{\partial\Omega} \phi(\boldsymbol{D}\cdot\boldsymbol{n})\,\mathrm{dS}, \tag{3.24}$$

and gathering like terms results in

$$\begin{aligned}
0 = \delta\Pi_M^H = &\int_\Omega (\boldsymbol{c}_E\,\boldsymbol{S} - \boldsymbol{e}^t\,\boldsymbol{E} - \text{symm}\boldsymbol{T})\cdot\delta\boldsymbol{S}\,\mathrm{d}V - \int_\Omega (\boldsymbol{e}\,\boldsymbol{S} + \boldsymbol{\epsilon}_S\,\boldsymbol{E} - \boldsymbol{D})\cdot\delta\boldsymbol{E}\,\mathrm{d}V \\
&+ \int_\Omega (\text{symm}\boldsymbol{\nabla}\boldsymbol{u} - \boldsymbol{S})\cdot\text{symm}\delta\boldsymbol{T}\,\mathrm{d}V + \int_\Omega (\text{skew}\boldsymbol{\nabla}\boldsymbol{u} - \boldsymbol{\psi} - \gamma^{-1}\text{skew}\boldsymbol{T})\cdot\text{skew}\delta\boldsymbol{T}\,\mathrm{d}V \\
&- \int_\Omega \text{skew}\boldsymbol{T}\cdot\delta\boldsymbol{\psi}\,\mathrm{d}V + \int_\Omega (\boldsymbol{\nabla}\phi + \boldsymbol{E})\cdot\delta\boldsymbol{D}\,\mathrm{d}V - \int_\Omega (\text{div}\boldsymbol{T} + \boldsymbol{f})\cdot\delta\boldsymbol{u}\,\mathrm{d}V \\
&- \int_\Omega (\text{div}\boldsymbol{D} - q)\delta\phi\,\mathrm{d}V + \int_{\partial\Omega_t} (\boldsymbol{T}\,\boldsymbol{n} - \bar{\boldsymbol{t}})\cdot\delta\boldsymbol{u}\,\mathrm{dS} + \int_{\partial\Omega_d} (\boldsymbol{D}\cdot\boldsymbol{n} + \bar{d})\delta\phi\,\mathrm{dS} \\
&- \int_{\partial\Omega_u} (\boldsymbol{u} - \bar{\boldsymbol{u}})\cdot(\delta\boldsymbol{T}\,\boldsymbol{n})\,\mathrm{dS} - \int_{\partial\Omega_\phi} (\phi - \bar{\phi})(\delta\boldsymbol{D}\cdot\boldsymbol{n})\,\mathrm{dS}.
\end{aligned} \tag{3.25}$$

All of the necessary Euler-Lagrange equations appear in (3.25). The variation $\delta\boldsymbol{\psi}$ enforces $\text{skew}\boldsymbol{T} = \boldsymbol{0}$ in Ω, while $\text{skew}\delta\boldsymbol{T}$ enforces compatibility between rotations and the skew part of the displacement gradient.

K-Type formulation based on functional Π_K^H

The skew-symmetric part of the stress tensor can be eliminated using the Euler-Lagrange equation $\gamma^{-1}\text{skew}\boldsymbol{T} = \text{skew}\boldsymbol{\nabla u} - \boldsymbol{\psi}$ in Ω, which appears in (3.25) as demonstrated by Hughes and Brezzi [18], to obtain the K-type Hu-Washizu-like functional:

$$\begin{aligned}\Pi_K^H(\boldsymbol{u},\boldsymbol{\psi},\text{symm}\boldsymbol{T},\boldsymbol{S},\phi,\boldsymbol{D},\boldsymbol{E}) &= \frac{1}{2}\int_\Omega \boldsymbol{c}_E\ \boldsymbol{S}\cdot\boldsymbol{S}\,\mathrm{d}V - \int_\Omega \boldsymbol{e}\ \boldsymbol{S}\cdot\boldsymbol{E}\,\mathrm{d}V \\ &- \frac{1}{2}\int_\Omega \boldsymbol{\epsilon}_S\ \boldsymbol{E}\cdot\boldsymbol{E}\,\mathrm{d}V + \int_\Omega(\text{symm}\boldsymbol{\nabla u}-\boldsymbol{S})\cdot\text{symm}\boldsymbol{T}\,\mathrm{d}V + \int_\Omega(\boldsymbol{\nabla}\phi+\boldsymbol{E})\cdot\boldsymbol{D}\,\mathrm{d}V \\ &+ \frac{1}{2}\gamma\int_\Omega|\text{skew}\boldsymbol{\nabla u}-\boldsymbol{\psi}|^2\,\mathrm{d}V - \int_\Omega \boldsymbol{f}\cdot\boldsymbol{u}\,\mathrm{d}V - \int_\Omega q\,\phi\,\mathrm{d}V - \int_{\partial\Omega_t}\bar{\boldsymbol{t}}\cdot\boldsymbol{u}\,\mathrm{dS} \\ &+ \int_{\partial\Omega_d}\bar{d}\,\phi\,\mathrm{dS} - \int_{\partial\Omega_u}(\boldsymbol{u}-\bar{\boldsymbol{u}})\cdot(\boldsymbol{T}\,\boldsymbol{n})\,\mathrm{dS} - \int_{\partial\Omega_\phi}(\phi-\bar{\phi})(\boldsymbol{D}\cdot\boldsymbol{n})\,\mathrm{dS}.\end{aligned} \tag{3.26}$$

Note that in this case, the stress term $\boldsymbol{T}$, in the Lagrange multiplier enforcing the displacement boundary conditions on $\partial\Omega_u$ is calculated as $\boldsymbol{T} = \text{symm}\boldsymbol{T} + \text{skew}\boldsymbol{T}$, where $\text{skew}\boldsymbol{T} = \gamma(\text{skew}\boldsymbol{\nabla u} - \boldsymbol{\psi})$. The first variation (and gathering like terms) results in

$$\begin{aligned}\delta\Pi_K^H = 0 = &\int_\Omega(\boldsymbol{c}_E\boldsymbol{S} - \boldsymbol{e}^t\boldsymbol{E} - \text{symm}\boldsymbol{T})\cdot\delta\boldsymbol{S}\,\mathrm{d}V - \int_\Omega(\boldsymbol{e}\boldsymbol{S} + \boldsymbol{\epsilon}_S\boldsymbol{E} - \boldsymbol{D})\cdot\delta\boldsymbol{S}\,\mathrm{d}V \\ &+ \int_\Omega(\text{symm}\boldsymbol{\nabla u}-\boldsymbol{S})\cdot\text{symm}\delta\boldsymbol{T}\,\mathrm{d}V - \int_\Omega(\gamma(\text{skew}\boldsymbol{\nabla u}-\boldsymbol{\psi}))\cdot\delta\boldsymbol{\psi}\,\mathrm{d}V \\ &+ \int_\Omega(\boldsymbol{\nabla}\psi+\boldsymbol{E})\cdot\delta\boldsymbol{D}\,\mathrm{d}V - \int_\Omega -(\text{symm}\boldsymbol{T}+\gamma(\text{skew}\boldsymbol{\nabla u}-\boldsymbol{\psi}))\cdot(\boldsymbol{\nabla}\delta\boldsymbol{u}) + \boldsymbol{f}\cdot\delta\boldsymbol{u}\,\mathrm{d}V \\ &- \int_\Omega -\boldsymbol{D}\cdot\boldsymbol{\nabla}\delta\phi - q\delta\phi\,\mathrm{d}V - \int_{\partial\Omega_t}\bar{\boldsymbol{t}}\cdot\delta\boldsymbol{u}\,\mathrm{dS} + \int_{\partial\Omega_d}\bar{d}\delta\phi\,\mathrm{dS} \\ &- \int_{\partial\Omega_u}\left[(\boldsymbol{u}-\bar{\boldsymbol{u}})\cdot(\delta\boldsymbol{T}\boldsymbol{n}) - (\boldsymbol{T}\boldsymbol{n})\cdot\delta\boldsymbol{u}\right]\,\mathrm{dS} - \int_{\partial\Omega_\phi}\left[(\phi-\bar{\phi})(\delta\boldsymbol{D}\cdot\boldsymbol{n}) - (\boldsymbol{D}\cdot\boldsymbol{n})\delta\phi\right]\,\mathrm{dS}.\end{aligned} \tag{3.27}$$

After applying the Gauss-Green identities, the following result is achieved:

$$\begin{aligned}\delta\Pi_K^H = 0 = &\int_\Omega(\boldsymbol{c}_E\ \boldsymbol{S} - \boldsymbol{e}^t\ \boldsymbol{E} - \text{symm}\boldsymbol{T})\cdot\delta\boldsymbol{S}\,\mathrm{d}V - \int_\Omega(\boldsymbol{e}\ \boldsymbol{S} + \boldsymbol{\epsilon}_S\ \boldsymbol{E} - \boldsymbol{D})\cdot\delta\boldsymbol{E}\,\mathrm{d}V \\ &+ \int_\Omega(\text{symm}\boldsymbol{\nabla u}-\boldsymbol{S})\cdot\text{symm}\delta\boldsymbol{T}\,\mathrm{d}V - \int_\Omega(\gamma(\text{skew}\boldsymbol{\nabla u}-\boldsymbol{\psi}))\cdot\delta\boldsymbol{\psi}\,\mathrm{d}V \\ &+ \int_\Omega(\boldsymbol{\nabla}\phi+\boldsymbol{E})\cdot\delta\boldsymbol{D}\,\mathrm{d}V - \int_\Omega(\text{div}\boldsymbol{T}+\boldsymbol{f})\cdot\delta\boldsymbol{u}\,\mathrm{d}V - \int_\Omega(\text{div}\boldsymbol{D}-q)\delta\phi\,\mathrm{d}V \\ &+ \int_{\partial\Omega_t}(\boldsymbol{T}\,\boldsymbol{n}-\bar{\boldsymbol{t}})\cdot\delta\boldsymbol{u}\,\mathrm{dS} + \int_{\partial\Omega_d}(\boldsymbol{D}\cdot\boldsymbol{n}+\bar{d})\delta\phi\,\mathrm{dS} \\ &- \int_{\partial\Omega_u}(\boldsymbol{u}-\bar{\boldsymbol{u}})\cdot(\delta\boldsymbol{T}\,\boldsymbol{n})\,\mathrm{dS} - \int_{\partial\Omega_\phi}(\phi-\bar{\phi})(\delta\boldsymbol{D}\cdot\boldsymbol{n})\,\mathrm{dS},\end{aligned} \tag{3.28}$$

which again contains all the necessary Euler equations. Here, the variation $\delta\boldsymbol{\psi}$ simultaneously enforces $\text{skew}\boldsymbol{T} = \boldsymbol{0}$ in Ω and compatibility between rotations and the skew part of displacement gradient.

In the remainder of this section, it is demonstrated how these two Hu-Washizu like functionals can be used to derive (two) irreducible functionals, (two) fully mixed Hellinger-Reissner like functionals and (four) degenerate Hellinger-Reissner like functionals.

The two preceding formulations were presented in some detail. For brevity, the presentation of the variational formulations of the remaining proposed functionals will be abbreviated. Only the functional and the final resulting variational equations containing the Euler-Lagrange equations will be presented.

3.4.2 Irreducible formulations

In order to simplify the formulation for finite element implementation, the irreducible forms emanating from Π_M^H and Π_K^H are now derived. In the context of this work, by 'irreducible' it is implied that the fewest independent variables for a given functional family are used. Of course, $\boldsymbol{u}$ and ϕ are the only independent variables required to fully describe the electroelastic problem since all other variables can be derived from these.[1] However, the 'irreducible' finite elements with drilling DOFs presented herein also require the in-plane rotation field $\boldsymbol{\psi}$ to be included as an independent variable. Furthermore, the M-type functionals intentionally retain skew$\boldsymbol{T}$, even in irreducible form.

M-Type formulation based on functional Π_M

The irreducible form resulting from Π_M^H can be derived by substituting the mechanical and electrical compatibilities (3.11) and (3.12) respectively into Π_M^H. Therefore, $\boldsymbol{S} = \text{symm}\boldsymbol{\nabla u}$, and $\boldsymbol{E} = -\boldsymbol{\nabla}\phi$ are substituted into (3.21).

The resulting functional, which retains the skew-symmetric part of stress as an independent variable, together with displacements, electric potentials and in-plane rotations, is:

$$\begin{aligned}\Pi_M(\boldsymbol{u},\boldsymbol{\psi},\text{skew}\boldsymbol{T},\phi) = \frac{1}{2}\int_\Omega \boldsymbol{c}_E\ \text{symm}\boldsymbol{\nabla u}\cdot\text{symm}\boldsymbol{\nabla u}\,\mathrm{d}V + \int_\Omega \boldsymbol{e}\ \text{symm}\boldsymbol{\nabla u}\cdot\boldsymbol{\nabla}\phi\,\mathrm{d}V \\ -\frac{1}{2}\int_\Omega \boldsymbol{\epsilon}_S\ \boldsymbol{\nabla}\phi\cdot\boldsymbol{\nabla}\phi\,\mathrm{d}V + \int_\Omega(\text{skew}\boldsymbol{\nabla u}-\boldsymbol{\psi})\cdot\text{skew}\boldsymbol{T}\,\mathrm{d}V - \frac{1}{2}\gamma^{-1}\int_\Omega|\text{skew}\boldsymbol{T}|^2\,\mathrm{d}V \\ -\int_\Omega \boldsymbol{f}\cdot\boldsymbol{u}\,\mathrm{d}V + \int_\Omega q\,\phi\,\mathrm{d}V - \int_{\partial\Omega_t}\bar{\boldsymbol{t}}\cdot\boldsymbol{u}\,\mathrm{dS} + \int_{\partial\Omega_d}\bar{d}\,\phi\,\mathrm{dS},\end{aligned} \tag{3.29}$$

where both $\boldsymbol{u}$ and ϕ are admissible, and therefore satisfy the essential boundary conditions. Since the aforementioned substitution effectively eliminates strain and electric field as independent variables, the compatibility between strain and displacement gradient and electric field and potential gradient are enforced in a strong sense. Furthermore the symmetric part of stress as well as electric flux density are also eliminated from the functional upon this substitution. Therefore the constitutive relations in (3.4) are also assumed to hold in a strong

[1] Not the fully story, stress and electric flux density or strain and electric field (or combinations) could also theoretically be used as the independent variables.

sense [16, 55]. After some algebra, the first variation of Π_M reduces to

$$\begin{aligned}\delta\Pi_M = 0 = &\int_\Omega (\text{skew}\boldsymbol{\nabla u} - \boldsymbol{\psi} - \gamma^{-1}\text{skew}\boldsymbol{T}) \cdot \text{skew}\delta\boldsymbol{T}\, \text{d}V - \int_\Omega \text{skew}\boldsymbol{T} \cdot \delta\boldsymbol{\psi}\, \text{d}V \\ &- \int_\Omega (\text{div}\boldsymbol{T} + \boldsymbol{f}) \cdot \delta\boldsymbol{u}\, \text{d}V - \int_\Omega (\text{div}\boldsymbol{D} - q)\delta\phi\, \text{d}V + \int_{\partial\Omega_t} (\boldsymbol{T}\,\boldsymbol{n} - \bar{\boldsymbol{t}}) \cdot \delta\boldsymbol{u}\, \text{dS} \\ &+ \int_{\partial\Omega_d} (\boldsymbol{D} \cdot \boldsymbol{n} + \bar{d})\delta\phi\, \text{dS},\end{aligned} \tag{3.30}$$

which again contains all the necessary Euler-Lagrange equations.

K-Type formulation: Functional Π_K

The K-type equivalent irreducible functional is derived using similar substitutions of the compatibility conditions, this time into Π_K^H. The emerging functional, with only displacements, in-plane rotations and electric potential as independent variables, can be shown to be:

$$\begin{aligned}\Pi_K(\boldsymbol{u}, \boldsymbol{\psi}, \phi) = &\frac{1}{2}\int_\Omega \boldsymbol{c}_E \text{symm}\boldsymbol{\nabla u} \cdot \text{symm}\boldsymbol{\nabla u}\, \text{d}V + \int_\Omega \boldsymbol{e}\text{symm}\boldsymbol{\nabla u} \cdot \boldsymbol{\nabla}\phi\, \text{d}V \\ &- \frac{1}{2}\int_\Omega \boldsymbol{\epsilon}_S \boldsymbol{\nabla}\phi \cdot \boldsymbol{\nabla}\phi\, \text{d}V + \frac{1}{2}\gamma\int_\Omega |\text{skew}\boldsymbol{\nabla u} - \boldsymbol{\psi}|^2\, \text{d}V - \int_\Omega \boldsymbol{f} \cdot \boldsymbol{u}\, \text{d}V \\ &+ \int_\Omega q\phi\, \text{d}V - \int_{\partial\Omega_t} \bar{\boldsymbol{t}} \cdot \boldsymbol{u}\, \text{dS} + \int_{\partial\Omega_d} \bar{d}\phi\, \text{dS},\end{aligned} \tag{3.31}$$

where both $\boldsymbol{u}$ and ϕ are again admissible functions. Once again, the constitutive and compatibility conditions are enforced in a strong sense. After applying the Gauss-Green identities and grouping like terms, the resulting variational equation is given by:

$$\begin{aligned}\delta\Pi_K = 0 = &-\int_\Omega \gamma(\text{skew}\boldsymbol{\nabla u} - \boldsymbol{\psi}) \cdot \delta\boldsymbol{\psi}\, \text{d}V - \int_\Omega (\text{div}\boldsymbol{T} + \boldsymbol{f}) \cdot \delta\boldsymbol{u}\, \text{d}V - \int_\Omega (\text{div}\boldsymbol{D} - q)\delta\phi\, \text{d}V \\ &+ \int_{\partial\Omega_t} (\boldsymbol{T}\boldsymbol{n} - \bar{\boldsymbol{t}}) \cdot \delta\boldsymbol{u}\, \text{dS} + \int_{\partial\Omega_d} (\boldsymbol{D} \cdot \boldsymbol{n} + \bar{d})\delta\phi\, \text{dS}.\end{aligned} \tag{3.32}$$

Recognising $\gamma(\text{skew}\boldsymbol{\nabla u} - \boldsymbol{\psi})$ as the skew-symmetric part of stress, once again all the necessary Euler equations are contained in (3.32).

3.4.3 Fully mixed Hellinger-Reissner-like formulations

Strain $\boldsymbol{S}$ and electric field $\boldsymbol{E}$ can both be eliminated from the Hu-Washizu-like functionals by substituting the constitutive relations in (3.9) into functionals Π_M^H and Π_K^H, resulting in fully mixed Hellinger-Reissner-like functionals. Of course, since strain and electric field are eliminated from the functional, their compatibility conditions are assumed *a priori*.

M-Type formulation based on functional Π_M^{TD}

The constitutive relations in terms of stress $\boldsymbol{T}$ and electric flux density $\boldsymbol{D}$ are substituted into Π_M^H, and the functional Π_M^{TD} is introduced. The superscripts 'T' and 'D' represent the additional independent variables (supplemental to the kinematic variables):

$$\begin{aligned}\Pi_M^{TD}(\boldsymbol{u},\boldsymbol{\psi},\text{symm}\boldsymbol{T},\text{skew}\boldsymbol{T},\phi,\boldsymbol{D}) = &-\frac{1}{2}\int_\Omega \boldsymbol{s}_D\ \text{symm}\boldsymbol{T}\cdot\text{symm}\boldsymbol{T}\,\mathrm{d}V - \int_\Omega \boldsymbol{g}\ \text{symm}\boldsymbol{T}\cdot\boldsymbol{D}\,\mathrm{d}V\\ &+\frac{1}{2}\int_\Omega \boldsymbol{\chi}_T\ \boldsymbol{D}\cdot\boldsymbol{D}\,\mathrm{d}V + \int_\Omega \text{symm}\boldsymbol{\nabla u}\cdot\text{symm}\boldsymbol{T}\,\mathrm{d}V + \int_\Omega \boldsymbol{\nabla}\phi\cdot\boldsymbol{D}\,\mathrm{d}V\\ &+\int_\Omega(\text{skew}\boldsymbol{\nabla u}-\boldsymbol{\psi})\cdot\text{skew}\boldsymbol{T}\,\mathrm{d}V - \frac{1}{2}\gamma^{-1}\int_\Omega|\text{skew}\boldsymbol{T}|^2\,\mathrm{d}V - \int_\Omega \boldsymbol{f}\cdot\boldsymbol{u}\,\mathrm{d}V\\ &+\int_\Omega q\,\phi\,\mathrm{d}V - \int_{\partial\Omega_t}\bar{\boldsymbol{t}}\cdot\boldsymbol{u}\,\mathrm{dS} + \int_{\partial\Omega_d}\bar{d}\,\phi\,\mathrm{dS} - \int_{\partial\Omega_u}(\boldsymbol{u}-\bar{\boldsymbol{u}})\cdot(\boldsymbol{T}\,\boldsymbol{n})\,\mathrm{dS}\\ &-\int_{\partial\Omega_\phi}(\phi-\bar{\phi})(\boldsymbol{D}\cdot\boldsymbol{n})\,\mathrm{dS}.\end{aligned} \tag{3.33}$$

After applying the Gauss-Green identities, the result of the first variation is

$$\begin{aligned}\delta\Pi_M^{TD} = 0 = &-\int_\Omega(\boldsymbol{s}_D\ \text{symm}\boldsymbol{T} + \boldsymbol{g}^t\ \boldsymbol{D} - \text{symm}\boldsymbol{\nabla u})\cdot\text{symm}\delta\boldsymbol{T}\,\mathrm{d}V\\ &+\int_\Omega(\text{skew}\boldsymbol{\nabla u}-\boldsymbol{\psi}-\gamma^{-1}\text{skew}\boldsymbol{T})\cdot\text{skew}\delta\boldsymbol{T}\,\mathrm{d}V\\ &+\int_\Omega(-\boldsymbol{g}\ \text{symm}\boldsymbol{T} + \boldsymbol{\chi}_T\ \boldsymbol{D} + \boldsymbol{\nabla}\phi)\cdot\delta\boldsymbol{D}\,\mathrm{d}V - \int_\Omega \text{skew}\boldsymbol{T}\cdot\delta\boldsymbol{\psi}\,\mathrm{d}V\\ &-\int_\Omega(\text{div}\boldsymbol{T}+\boldsymbol{f})\cdot\delta\boldsymbol{u}\,\mathrm{d}V - \int_\Omega(\text{div}\boldsymbol{D}-q)\delta\phi\,\mathrm{d}V + \int_{\partial\Omega_t}(\boldsymbol{T}\,\boldsymbol{n}-\bar{\boldsymbol{t}})\cdot\delta\boldsymbol{u}\,\mathrm{dS}\\ &+\int_{\partial\Omega_d}(\boldsymbol{D}\cdot\boldsymbol{n}+\bar{d})\delta\phi\,\mathrm{dS} - \int_{\partial\Omega_u}(\boldsymbol{u}-\bar{\boldsymbol{u}})\cdot(\delta\boldsymbol{T}\,\boldsymbol{n})\,\mathrm{dS} - \int_{\partial\Omega_\phi}(\phi-\bar{\phi})(\delta\boldsymbol{D}\cdot\boldsymbol{n})\,\mathrm{dS},\end{aligned} \tag{3.34}$$

where the Euler equation $\boldsymbol{s}_D\ \text{symm}\boldsymbol{T} + \boldsymbol{g}^t\ \boldsymbol{D} = \text{symm}\boldsymbol{\nabla u}$ weakly enforces the relationship between strain derived from compatibility conditions (3.11), and strain based on stress and electric flux density from constitutive equations (3.9). Similarly, $-\boldsymbol{g}\ \text{symm}\boldsymbol{T}+\boldsymbol{\chi}_T\ \boldsymbol{D} = -\boldsymbol{\nabla}\phi$ enforces weakly the relationship between compatibility (3.12) and constitutive equations (3.9) for electric field.

K-Type formulation: Functional Π_K^{TD}

The corresponding K-type fully-mixed functional can be derived by either making the substitutions of constitutive equations described previously to arrive at the Π_M^{TD} functional, or through elimination of the skew-symmetric part of stress by substitution of $\text{skew}\boldsymbol{T} = \gamma(\text{skew}\boldsymbol{\nabla u}-\boldsymbol{\psi})$ which appears as one of the Euler equations in (3.34) into Π_M^{TD}. In either

case, the resulting functional is

$$\begin{aligned}\Pi_K^{TD}(\boldsymbol{u},\boldsymbol{\psi},\text{symm}\boldsymbol{T},\phi,\boldsymbol{D}) = &-\frac{1}{2}\int_\Omega \boldsymbol{s}_D\text{symm}\boldsymbol{T}\cdot\text{symm}\boldsymbol{T}\,\mathrm{d}V - \int_\Omega \boldsymbol{g}\text{symm}\boldsymbol{T}\cdot\boldsymbol{D}\,\mathrm{d}V\\ &+\frac{1}{2}\int_\Omega \boldsymbol{\chi}_T\boldsymbol{D}\cdot\boldsymbol{D}\,\mathrm{d}V + \int_\Omega \text{symm}\boldsymbol{\nabla u}\cdot\text{symm}\boldsymbol{T}\,\mathrm{d}V + \int_\Omega \boldsymbol{\nabla}\phi\cdot\boldsymbol{D}\,\mathrm{d}V\\ &+\frac{1}{2}\gamma\int_\Omega |\text{skew}\boldsymbol{\nabla u}-\boldsymbol{\psi}|^2\,\mathrm{d}V - \int_\Omega \boldsymbol{f}\cdot\boldsymbol{u}\,\mathrm{d}V + \int_\Omega q\phi\,\mathrm{d}V\\ &-\int_{\partial\Omega_t}\bar{\boldsymbol{t}}\cdot\boldsymbol{u}\,\mathrm{dS} + \int_{\partial\Omega_d}\bar{d}\phi\,\mathrm{dS} - \int_{\partial\Omega_u}(\boldsymbol{u}-\bar{\boldsymbol{u}})\cdot(\boldsymbol{T}\boldsymbol{n})\,\mathrm{dS}\\ &-\int_{\partial\Omega_\phi}(\phi-\bar{\phi})(\boldsymbol{D}\cdot\boldsymbol{n})\,\mathrm{dS}.\end{aligned} \tag{3.35}$$

Once again, like terms are collected after taking the first variation, and apply the Gauss-Green identities to arrive at the variational equation:

$$\begin{aligned}\delta\Pi_K^{TD} = 0 = &-\int_\Omega(\boldsymbol{s}_D\text{symm}\boldsymbol{T} + \boldsymbol{g}^t\boldsymbol{D} - \text{symm}\boldsymbol{\nabla u})\cdot\text{symm}\delta\boldsymbol{T}\,\mathrm{d}V\\ &+(-\boldsymbol{g}\text{symm}\boldsymbol{T} + \boldsymbol{\chi}_T\boldsymbol{D} + \boldsymbol{\nabla}\phi)\cdot\delta\boldsymbol{D}\,\mathrm{d}V - \int_\Omega\gamma(\text{skew}\boldsymbol{\nabla u}-\boldsymbol{\psi})\cdot\delta\boldsymbol{\psi}\,\mathrm{d}V\\ &-\int_\Omega(\text{div}\boldsymbol{T}+\boldsymbol{f})\cdot\delta\boldsymbol{u}\,\mathrm{d}V - \int_\Omega(\text{div}\boldsymbol{D}-q)\delta\phi\,\mathrm{d}V + \int_{\partial\Omega_t}(\boldsymbol{T}\boldsymbol{n}-\bar{\boldsymbol{t}})\cdot\delta\boldsymbol{u}\,\mathrm{dS}\\ &+\int_{\partial\Omega_d}(\boldsymbol{D}\cdot\boldsymbol{n}+\bar{d})\delta\phi\,\mathrm{dS} - \int_{\partial\Omega_u}(\boldsymbol{u}-\bar{\boldsymbol{u}})\cdot(\delta\boldsymbol{T}\boldsymbol{n})\,\mathrm{dS} - \int_{\partial\Omega_\phi}(\phi-\bar{\phi})(\delta\boldsymbol{D}\cdot\boldsymbol{n})\,\mathrm{dS}.\end{aligned} \tag{3.36}$$

Again, the variation on $\boldsymbol{\psi}$ simultaneously enforces compatibility between the skew-symmetric part of the displacement gradient and the rotation field, and the symmetry conditions for stress. Once again all weak relationships necessary, are contained in (3.36).

3.4.4 Degenerate Hellinger-Reissner-like formulations

It is also possible to derive functionals with only stress $\boldsymbol{T}$ *or* electric flux density $\boldsymbol{D}$ assumed, additionally to $\boldsymbol{u}$ and ϕ, using the remaining forms of the constitutive equations, given in (3.5) and (3.7). Since only stress or electric flux density are assumed, these functionals will be referred to as degenerate.

M-Type formulation: Functional Π_M^D

If strain (and the symmetric part of stress) are eliminated from Π_M^H by substituting $\boldsymbol{S} = \text{symm}\boldsymbol{\nabla u}$, and if electric field is eliminated by substituting the second equation of (3.5) into Π_M^H, the M-type Hellinger-Reissner like functional which results is:

$$\begin{aligned}\Pi_M^D(\boldsymbol{u},\boldsymbol{\psi},\text{skew}\boldsymbol{T},\phi,\boldsymbol{D}) = \frac{1}{2}\int_\Omega \boldsymbol{c}_D\,\text{symm}\boldsymbol{\nabla u}\cdot\text{symm}\boldsymbol{\nabla u}\,\text{d}V - \int_\Omega \boldsymbol{h}\,\text{symm}\boldsymbol{\nabla u}\cdot\boldsymbol{D}\,\text{d}V\\ + \frac{1}{2}\int_\Omega \boldsymbol{\chi}_S\,\boldsymbol{D}\cdot\boldsymbol{D}\,\text{d}V + \int_\Omega(\text{skew}\boldsymbol{\nabla u}-\boldsymbol{\psi})\cdot\text{skew}\boldsymbol{T}\,\text{d}V + \int_\Omega \boldsymbol{\nabla}\phi\cdot\boldsymbol{D}\,\text{d}V\\ - \frac{1}{2}\gamma^{-1}\int_\Omega|\text{skew}\boldsymbol{T}|^2\,\text{d}V - \int_\Omega \boldsymbol{f}\cdot\boldsymbol{u}\,\text{d}V + \int_\Omega q\,\phi\,\text{d}V - \int_{\partial\Omega_t}\bar{\boldsymbol{t}}\cdot\boldsymbol{u}\,\text{dS}\\ + \int_{\partial\Omega_d}\bar{d}\,\phi\,\text{dS} - \int_{\partial\Omega_\phi}(\phi-\bar{\phi})(\boldsymbol{D}\cdot\boldsymbol{n})\,\text{dS},\end{aligned} \tag{3.37}$$

where the displacement field $\boldsymbol{u}$ is admissible. In this case, the compatibility between strain and displacement gradient $\boldsymbol{S} = \text{symm}\boldsymbol{\nabla u}$, as well as the constitutive relationship between stress and stain and electric flux density, $\text{symm}\boldsymbol{T} = \boldsymbol{c}_D\boldsymbol{S} - \boldsymbol{h}^t\boldsymbol{D}$ are assumed to be enforced in a strong sense.

Yet again, the first variation is computed, and after applying integration by parts, the resulting variational statement is

$$\begin{aligned}\delta\Pi_M^D = 0 = \int_\Omega(\text{skew}\boldsymbol{\nabla u}-\boldsymbol{\psi}-\gamma^{-1}\text{skew}\boldsymbol{T})\cdot\text{skew}\delta\boldsymbol{T}\,\text{d}V\\ - \int_\Omega(\boldsymbol{h}\text{symm}\boldsymbol{\nabla u}-\boldsymbol{\chi}_S\boldsymbol{D}-\boldsymbol{\nabla}\phi)\cdot\delta\boldsymbol{D}\,\text{d}V - \int_\Omega\text{skew}\boldsymbol{T}\cdot\delta\boldsymbol{\psi}\,\text{d}V\\ - \int_\Omega(\text{div}\boldsymbol{T}+\boldsymbol{f})\cdot\delta\boldsymbol{u}\,\text{d}V - \int_\Omega(\text{div}\boldsymbol{D}-q)\delta\phi\,\text{d}V + \int_{\partial\Omega_t}(\boldsymbol{T}\boldsymbol{n}-\bar{\boldsymbol{t}})\cdot\delta\boldsymbol{u}\,\text{dS}\\ + \int_{\partial\Omega_d}(\boldsymbol{D}\cdot\boldsymbol{n}+\bar{d})\delta\phi\,\text{dS} - \int_{\partial\Omega_\phi}(\phi-\bar{\phi})(\delta\boldsymbol{D}\cdot\boldsymbol{n})\,\text{dS}.\end{aligned} \tag{3.38}$$

Once again (3.38) enforces all the necessary relations in a weak sense. In particular the arbitrary variation on $\boldsymbol{D}$ weakly enforces the relationship between electric field in terms of potential gradient and electric field in terms of its constitutive definition in (3.5).

K-Type formulation: Functional Π_K^D

Once again, the skew-symmetric part of stress can be eliminated from Π_M^D by substituting the Euler equation in terms of the skew-stress, which appears in (3.38), to produce Π_K^D. Alternatively, Π_K^D can be derived from Π_K^H by making the appropriate substitutions, described in the derivation of Π_M^D. The K-type functional with displacement, electric potential, in-plane rotations and electric flux density as independent variables is found to be:

$$\begin{aligned}\Pi_K^D(\boldsymbol{u},\boldsymbol{\psi},\phi,\boldsymbol{D}) =& \frac{1}{2}\int_\Omega \boldsymbol{c}_D\text{symm}\boldsymbol{\nabla u}\cdot\text{symm}\boldsymbol{\nabla u}\,\mathrm{d}V - \int_\Omega \boldsymbol{h}\text{symm}\boldsymbol{\nabla u}\cdot\boldsymbol{D}\,\mathrm{d}V \\ &+\frac{1}{2}\int_\Omega \boldsymbol{\chi}_S\boldsymbol{D}\cdot\boldsymbol{D}\,\mathrm{d}V + \int_\Omega \boldsymbol{\nabla}\phi\cdot\boldsymbol{D}\,\mathrm{d}V + \frac{1}{2}\gamma\int_\Omega |\text{skew}\boldsymbol{\nabla u}-\boldsymbol{\psi}|^2\,\mathrm{d}V \\ &-\int_\Omega \boldsymbol{f}\cdot\boldsymbol{u}\,\mathrm{d}V + \int_\Omega q\phi\,\mathrm{d}V - \int_{\partial\Omega_t}\bar{\boldsymbol{t}}\cdot\boldsymbol{u}\,\mathrm{dS} + \int_{\partial\Omega_d}\bar{d}\phi\,\mathrm{dS} \\ &-\int_{\partial\Omega_\phi}(\phi-\bar{\phi})(\boldsymbol{D}\cdot\boldsymbol{n})\,\mathrm{dS},\end{aligned} \tag{3.39}$$

where $\boldsymbol{u}$ is again admissible. Following the same process as previously, after taking the first variation, applying the Gauss-Green identities, and collecting like terms, the resulting variational statement is given by

$$\begin{aligned}\delta\Pi_K^D = 0 =& -\int_\Omega(\boldsymbol{h}\text{symm}\boldsymbol{\nabla u}-\boldsymbol{\chi}_S\boldsymbol{D}-\boldsymbol{\nabla}\phi)\cdot\delta\boldsymbol{D}\,\mathrm{d}V - \int_\Omega\gamma(\text{skew}\boldsymbol{\nabla u}-\boldsymbol{\psi})\cdot\delta\boldsymbol{\psi}\,\mathrm{d}V \\ &-\int_\Omega(\text{div}\boldsymbol{T}+\boldsymbol{f})\cdot\delta\boldsymbol{u}\,\mathrm{d}V - \int_\Omega(\text{div}\boldsymbol{D}-q)\delta\phi\,\mathrm{d}V + \int_{\partial\Omega_t}(\boldsymbol{T}\boldsymbol{n}-\bar{\boldsymbol{t}})\cdot\delta\boldsymbol{u}\,\mathrm{dS} \\ &+\int_{\partial\Omega_d}(\boldsymbol{D}\cdot\boldsymbol{n}+\bar{d})\delta\phi\,\mathrm{dS} - \int_{\partial\Omega_\phi}(\phi-\bar{\phi})(\delta\boldsymbol{D}\cdot\boldsymbol{n})\,\mathrm{dS},\end{aligned} \tag{3.40}$$

which yet again contains all the necessary Euler-Lagrange equations.

M-Type formulation: Functional Π_M^T

If on the other hand, electric field (and electric flux density) are eliminated from Π_M^H by substituting $\boldsymbol{E}=-\boldsymbol{\nabla}\phi$, and if strain is eliminated by substituting the first equation of (3.7) into Π_M^H, a functional with symm$\boldsymbol{T}$ assumed is achieved.

$$\begin{aligned}\Pi_M^T(\boldsymbol{u},\boldsymbol{\psi},\text{symm}\boldsymbol{T},\text{skew}\boldsymbol{T},\phi) =& -\frac{1}{2}\int_\Omega \boldsymbol{s}_E\,\text{symm}\boldsymbol{T}\cdot\text{symm}\boldsymbol{T}\,\mathrm{d}V + \int_\Omega \boldsymbol{d}\,\text{symm}\boldsymbol{T}\cdot\boldsymbol{\nabla}\phi\,\mathrm{d}V \\ &-\frac{1}{2}\int_\Omega \boldsymbol{\epsilon}_T\,\boldsymbol{\nabla}\phi\cdot\boldsymbol{\nabla}\phi\,\mathrm{d}V + \int_\Omega \text{symm}\boldsymbol{\nabla u}\cdot\text{symm}\boldsymbol{T}\,\mathrm{d}V + \int_\Omega(\text{skew}\boldsymbol{\nabla u}-\boldsymbol{\psi})\cdot\text{skew}\boldsymbol{T}\,\mathrm{d}V \\ &-\frac{1}{2}\gamma^{-1}\int_\Omega|\text{skew}\boldsymbol{T}|^2\,\mathrm{d}V - \int_\Omega \boldsymbol{f}\cdot\boldsymbol{u}\,\mathrm{d}V + \int_\Omega q\,\phi\,\mathrm{d}V - \int_{\partial\Omega_t}\bar{\boldsymbol{t}}\cdot\boldsymbol{u}\,\mathrm{dS} \\ &+\int_{\partial\Omega_d}\bar{d}\,\phi\,\mathrm{dS} - \int_{\partial\Omega_u}(\boldsymbol{u}-\bar{\boldsymbol{u}})\cdot(\boldsymbol{T}\,\boldsymbol{n})\,\mathrm{dS},\end{aligned} \tag{3.41}$$

where ϕ is admissible. In this instance, the constitutive equation $\boldsymbol{D}=\boldsymbol{d}\text{symm}+\boldsymbol{\epsilon}_T\boldsymbol{E}$ and compatibility condition $\boldsymbol{E}=-\boldsymbol{\nabla}\phi$ require enforcement in a strong sense. Yet again, after some calculations, the first variation ultimately results in

$$\begin{aligned}\delta\Pi_M^T = 0 = &\int_\Omega -(\boldsymbol{s}_E\text{symm}\boldsymbol{T} - \boldsymbol{d}^t\boldsymbol{\nabla}\phi - \text{symm}\boldsymbol{\nabla}\boldsymbol{u})\cdot\text{symm}\delta\boldsymbol{T}\,\text{d}V - \int_\Omega \text{skew}\boldsymbol{T}\delta\boldsymbol{\psi}\,\text{d}V\\ &+\int_\Omega(\text{skew}\boldsymbol{\nabla}\boldsymbol{u} - \boldsymbol{\psi} - \gamma^{-1}\text{skew}\boldsymbol{T})\cdot\text{skew}\delta\boldsymbol{T} - \int_\Omega(\text{div}\boldsymbol{T}+\boldsymbol{f})\cdot\delta\boldsymbol{u}\,\text{d}V\\ &-\int_\Omega(\text{div}\boldsymbol{D}-q)\delta\phi\,\text{d}V + \int_{\partial\Omega_t}(\boldsymbol{T}\boldsymbol{n}-\bar{\boldsymbol{t}})\cdot\delta\boldsymbol{u}\,\text{dS} + \int_{\partial\Omega_d}(\boldsymbol{D}\cdot\boldsymbol{n}+\bar{d})\delta\phi\,\text{dS}\\ &-\int_{\partial\Omega_u}(\boldsymbol{u}-\bar{\boldsymbol{u}})\cdot(\delta\boldsymbol{T}\boldsymbol{n})\,\text{dS}.\end{aligned} \tag{3.42}$$

The variational statement in (3.42) once yet again weakly enforces all necessary relationships. In this instance, variations on symm$\boldsymbol{T}$ weakly enforces the relationship between strain derived from displacement gradient and strain contained in the constitutive equations in (3.7).

K-Type formulation: Functional Π_K^T

Finally, the K-type counterpart of (3.41) can be constructed by either eliminating the skew symmetric part of stress from Π_M^T or by making the appropriate substitutions in Π_K^H (see Figure 3.1 and Section 3.4.5 for details).

$$\begin{aligned}\Pi_K^T(\boldsymbol{u},\boldsymbol{\psi},\text{symm}\boldsymbol{T},\phi) = &-\frac{1}{2}\int_\Omega \boldsymbol{s}_E\text{symm}\boldsymbol{T}\cdot\text{symm}\boldsymbol{T}\,\text{d}V + \int_\Omega \boldsymbol{d}\text{symm}\boldsymbol{T}\cdot\boldsymbol{\nabla}\phi\,\text{d}V\\ &-\frac{1}{2}\int_\Omega \boldsymbol{\epsilon}_T\boldsymbol{\nabla}\phi\cdot\boldsymbol{\nabla}\phi\,\text{d}V + \int_\Omega \text{symm}\boldsymbol{\nabla}\boldsymbol{u}\cdot\text{symm}\boldsymbol{T}\,\text{d}V\\ &+\frac{1}{2}\gamma\int_\Omega|\text{skew}\boldsymbol{\nabla}\boldsymbol{u}-\boldsymbol{\psi}|^2\,\text{d}V - \int_\Omega \boldsymbol{f}\cdot\boldsymbol{u}\,\text{d}V + \int_\Omega q\phi\,\text{d}V\\ &-\int_{\partial\Omega_t}\bar{\boldsymbol{t}}\cdot\boldsymbol{u}\,\text{dS} + \int_{\partial\Omega_d}\bar{d}\phi\,\text{dS} - \int_{\partial\Omega_u}(\boldsymbol{u}-\bar{\boldsymbol{u}})\cdot(\boldsymbol{T}\boldsymbol{n})\,\text{dS},\end{aligned} \tag{3.43}$$

where ϕ is admissible. Following the same process as before, the first variation can be shown to reduce to

$$\begin{aligned}\delta\Pi_K^T = 0 = &\int_\Omega -(\boldsymbol{s}_E\text{symm}\boldsymbol{T} - \boldsymbol{d}^t\boldsymbol{\nabla}\phi - \text{symm}\boldsymbol{\nabla}\boldsymbol{u})\cdot\text{symm}\delta\boldsymbol{T}\,\text{d}V\\ &-\int_\Omega\gamma(\text{skew}\boldsymbol{\nabla}\boldsymbol{u}-\boldsymbol{\psi})\cdot\delta\boldsymbol{\psi}\,\text{d}V - \int_\Omega(\text{div}\boldsymbol{T}+\boldsymbol{f})\cdot\delta\boldsymbol{u}\,\text{d}V\\ &-\int_\Omega(\text{div}\boldsymbol{D}-q)\delta\phi\,\text{d}V + \int_{\partial\Omega_t}(\boldsymbol{T}\boldsymbol{n}-\bar{\boldsymbol{t}})\cdot\delta\boldsymbol{u}\,\text{dS} + \int_{\partial\Omega_d}(\boldsymbol{D}\cdot\boldsymbol{n}+\bar{d})\delta\phi\,\text{dS}\\ &-\int_{\partial\Omega_u}(\boldsymbol{u}-\bar{\boldsymbol{u}})\cdot(\delta\boldsymbol{T}\boldsymbol{n})\,\text{dS},\end{aligned} \tag{3.44}$$

which once yet again weakly enforces all necessary conditions.

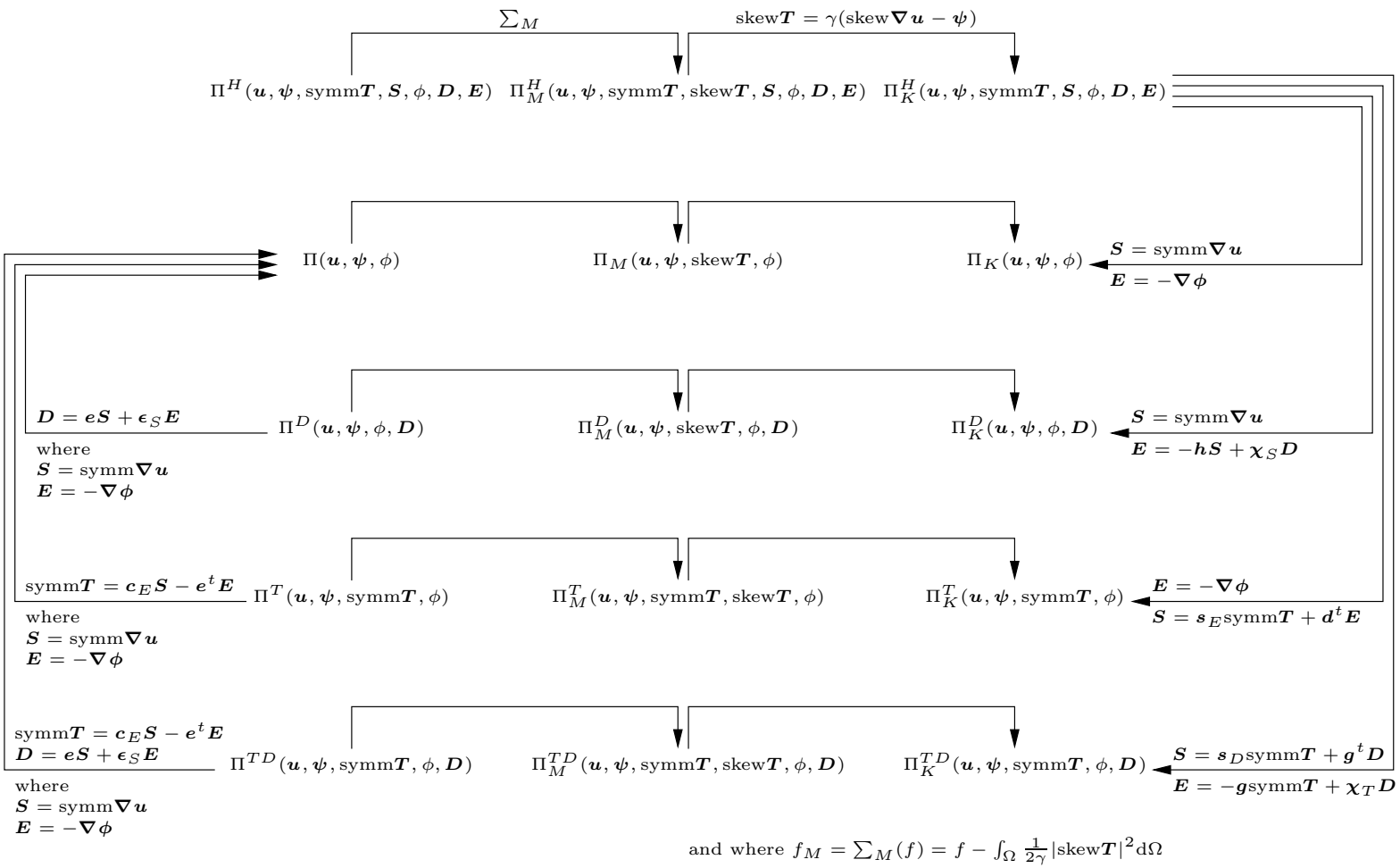

Figure 3.1: Relationships between the functionals.

In all, ten new functionals have been introduced in this section. At this point, a summary of the relationships between the functionals is appropriate, since not all of the relationships have explicitly been detailed in the foregoing.

3.4.5 Relationships between the functionals

In Figure 3.1 the relations between the various functionals are graphically depicted for the piezoelectricity problem. This figure is similar to Figure 2.3 presented in Section 2.4 for the elastostatic problem.

In total, 15 functionals are represented in Figure 3.1 arranged in five rows and three columns. The top row contains the Hu-Washizu like functionals while the irreducible functionals are represented in the second row. Rows three and four contain the degenerate Hellinger-Reissner like functionals. Finally, the fully mixed functionals are presented in the fifth row from the top (see Figure 3.2). The three families of functionals are contained in different columns. The Reissner like functionals (not explicitly presented in this chapter) are contained in the first column (from the left), the middle column contains the M-type functional while the K-type functionals are represented in the column on the right hand side.

As indicated in Figure 3.1, the only difference between the Reissner like functionals and the M-type functionals is the additional term $\int_\Omega \frac{1}{2\gamma}|\text{skew}\boldsymbol{T}|^2 \, \mathrm{d}V$. Furthermore, K-Type functionals can be derived from M-Type functionals by making the substitution $\text{skew}\boldsymbol{T} = \gamma(\text{skew}\boldsymbol{\nabla u} - \boldsymbol{\psi})$. These relations are indicated by the arrows above the respective columns.

In the preceding text, it has been shown that the irreducible, degenerate Hellinger-Reissner and fully mixed Hellinger-Reissner functionals can be derived from the Hu-Washizu like functional by making the substitutions as indicated by the arrows on the far right of Figure 3.2.

Finally it can also be shown that, within any of the three families (columns), both the degenerate and fully mixed Hellinger-Reissner like functionals can be used as a basis to derive the irreducible functionals. Specifically, if $\text{symm}\boldsymbol{T} = \boldsymbol{c}_E \ \text{symm}\boldsymbol{\nabla u} + \boldsymbol{e}^t \ \boldsymbol{\nabla\phi}$ and $\boldsymbol{D} = \boldsymbol{e} \ \text{symm}\boldsymbol{\nabla u} - \boldsymbol{\epsilon}_S \ \boldsymbol{\nabla\phi}$ are substituted into the fully mixed functionals, the corresponding irreducible functionals result. Similarly, if $\text{symm}\boldsymbol{T} = \boldsymbol{c}_E \ \text{symm}\boldsymbol{\nabla u} + \boldsymbol{e}^t \ \boldsymbol{\nabla\phi}$ is substituted into the degenerate functionals including stress, or if $\boldsymbol{D} = \boldsymbol{e} \ \text{symm}\boldsymbol{\nabla u} - \boldsymbol{\epsilon}_S \ \boldsymbol{\nabla\phi}$ is substituted into the degenerate functionals including electric flux density, the irreducible functionals also result. These relations are shown on the far left of Figure 3.1.

In this work, not all of the finite elements resulting from variational formulations of the 15 functionals depicted in Figure 3.1 have been implemented numerically. Figure 3.2 depicts the relations between the functionals in terms of their finite element implementation in this study.

As explained in Chapter 2, elastostatic formulations resulting from the functional of Reissner [40] are not suitable for implementation in discrete form, due to stability issues [18]. Numerical experiments confirmed that this is also the case for the piezoelectric problem. Furthermore, assumed strain (and electric field) finite elements are beyond the scope of this study. The Hu-Washizu like functionals in the top row of Figure 3.2 are therefore not implemented. The eight elements based on the remaining functionals are all implemented, and

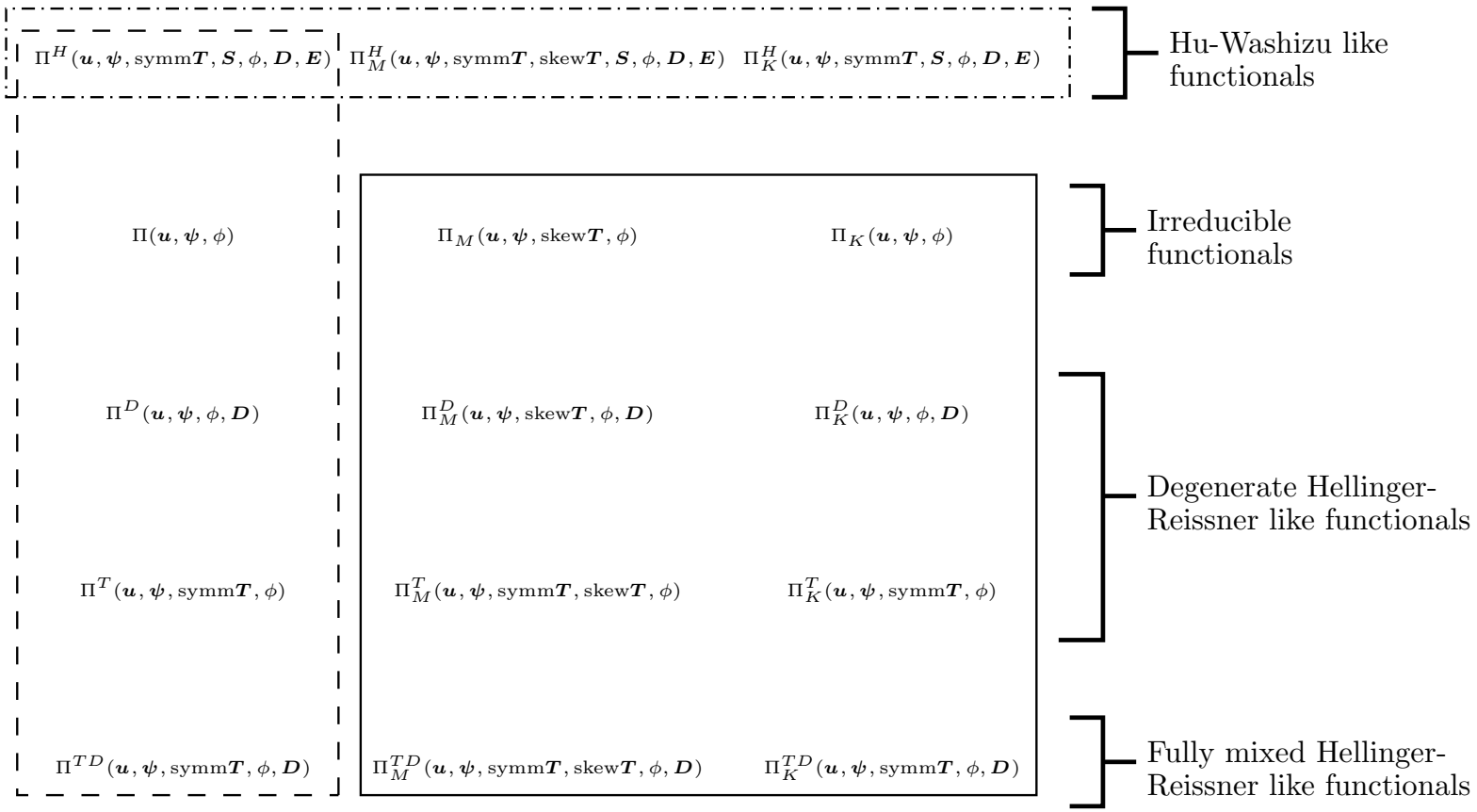

Figure 3.2: Relationships between the functionals in terms of their finite element implementation.

will be the focus of the remainder of this chapter.

3.5 Finite element interpolations

In this section the interpolations, used in the finite element implementation arising from the functionals presented in Section 3.4, are briefly discussed. The scalar potential and the independent rotation fields are interpolated as

$$\phi^h = \sum_e \sum_{i=1}^{4} N_i^e(\xi,\eta)\phi_i, \tag{3.45}$$

$$\psi^h = \sum_e \sum_{i=1}^{4} N_i^e(\xi,\eta)\psi_i, \tag{3.46}$$

respectively, with N_i^e the standard bilinear shape functions. The in-plane displacement approximation is taken as an Allman-type interpolation field, after Ibrahimbegovic *et al.* [21]

$$\left\{ \begin{array}{c} u_1 \\ u_2 \end{array} \right\} = \boldsymbol{u}^h = \sum_e \sum_{i=1}^{4} N_i^e(\xi,\eta)\boldsymbol{u}_i + \frac{l_{jk}}{8} \sum_e \sum_{i=5}^{8} NS_i^e(\xi,\eta)(\psi_k - \psi_j)\boldsymbol{n}_{jk}, \tag{3.47}$$

with NS_i the Serendipity shape functions. The hierarchical bubble shape function is not included. Furthermore, l_{jk} and $\boldsymbol{n}_{jk}$ denote the length and the outward unit normal vector on the element side associated with the corner nodes j and k (see Figure 3.3), i.e.

$$\boldsymbol{n}_{jk} = \left\{ \begin{array}{c} n_1 \\ n_2 \end{array} \right\} = \left\{ \begin{array}{c} \cos\alpha_{jk} \\ \sin\alpha_{jk} \end{array} \right\}, \tag{3.48}$$

and

$$l_{jk} = ((x_k - x_j)^2 + (y_k - y_j)^2)^{1/2}. \tag{3.49}$$

The indices in the above are explicitly given in Section 2.5.

The skew-symmetric stress field is chosen constant over the element, i.e.

$$\text{skew}\, \boldsymbol{T}^h = \sum_e T_0^e. \tag{3.50}$$

Using matrix notation, $\text{symm}\boldsymbol{\nabla}\boldsymbol{u}^e$ and $\text{skew}\boldsymbol{\nabla}\boldsymbol{u}^e$ are respectively given by

$$\text{symm}\boldsymbol{\nabla}\boldsymbol{u}^e = \boldsymbol{B}_i^e\boldsymbol{u}_i + \boldsymbol{G}_i^e\boldsymbol{\psi}_i, \tag{3.51}$$

and

$$\text{skew}\boldsymbol{\nabla}\boldsymbol{u}^e = \boldsymbol{b}_i^e\boldsymbol{u}_i + \boldsymbol{g}_i^e\boldsymbol{\psi}_i. \tag{3.52}$$

The operators arising from this interpolation are also summarised in Section 2.5, and are therefore not repeated here. The 'membrane locking correction', due to Taylor [38] is used, i.e. element strains are modified to become

$$\text{symm}\boldsymbol{\nabla}\tilde{\boldsymbol{u}}^e = \boldsymbol{B}_i^e\boldsymbol{u}_i + \left(\boldsymbol{G}_i^e - \frac{1}{\Omega^e} \int_{\Omega^e} \boldsymbol{G}_i^e \, \mathrm{d}V \right) \boldsymbol{\psi}_i. \tag{3.53}$$

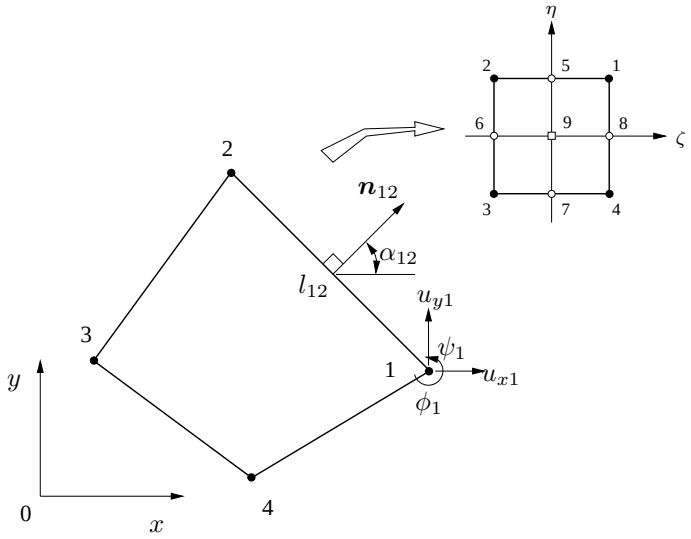

Figure 3.3: A planar 4-node piezoelectric element with drilling rotations.

For interpolations of stress and electric flux density, the necessary (but not sufficient) conditions for element stability are:

$$n_{\beta T} \geq n_u - m_u, \tag{3.54}$$

$$n_{\beta D} \geq n_\phi - m_\phi, \tag{3.55}$$

where $n_{\beta T}$ and $n_{\beta D}$ are the number of assumed stress and electric flux density modes, respectively. Furthermore, n_u and n_ϕ are the number of displacement and potential modes, respectively. The number of rigid body displacement modes is m_u, and m_ϕ represents the single (constant potential) distribution resulting in zero field. The equality conditions in (3.54) and (3.55) represent the optimal number of parameters in both cases.

For our planar elements with drilling degrees of freedom (DOFs), $n_u = 12$, and $n_\phi = 4$. The single potential distribution resulting in zero field means $m_\phi = 1$, and usually membrane elements possess three rigid body modes ($m_u = 3$). The optimal number of parameters required is therefore $n_{\beta T} = 9$ for stress and $n_{\beta D} = 3$ for flux density. One more than optimal, i.e. $n_{\beta D} = 4$, parameters are required for interpolation of the electric flux density in order to ensure the element is invariant [65]. Stability is achieved if no spurious zero energy modes appear, viz. if rank sufficiency of the mechanical stiffness and dielectric stiffness matrices is maintained [66].

Sze *et al.* [50, 51] presented a rank sufficient elastic element with drilling DOFs using only 8 interpolating stress modes, which appears to be one less than the optimal prescribed in (3.54). However, $n_{\beta T} = 8$ seems adequate, since m_u in (3.54) is in fact equal to 4 and not 3. The additional so-called θ_1–mode (in which rotations at each node are equal) is intrinsic to the reduced displacement interpolation. The strain corresponding to this state is zero.

Geyer and Groenwold [43] also presented a family of membrane elements with drilling DOFs, some of which employ only 8 stress modes for interpolation and retain stability. Elements with both 8 and 9 stress interpolating modes are tested.

The assumed electric flux density vector is interpolated using

$$\boldsymbol{D}^h = \sum_e \left[\begin{array}{cc} \boldsymbol{I}^e_{Dc} & \boldsymbol{A}^e_D \boldsymbol{P}^e_{Dh} \end{array} \right] \left\{ \begin{array}{c} \boldsymbol{\beta}^e_{Dc} \\ \boldsymbol{\beta}^e_{Dh} \end{array} \right\}, \tag{3.56}$$

where $\boldsymbol{I}^e_{Dc}$ is a 2×2 identity matrix to account for the constant flux density case and $\boldsymbol{\beta}^e_{Dc}$ are the corresponding parameters. $\boldsymbol{A}^e_D$ is a transformation matrix [65, 76, 79], and $\boldsymbol{P}^e_{Dh}$ represents the interpolation of the higher order part of charge density with $\boldsymbol{\beta}^e_{Dh}$ the corresponding parameters. $\boldsymbol{A}^e_D$ and $\boldsymbol{P}^e_{Dh}$ are given explicitly as

$$\boldsymbol{A}^e_D = \left[\begin{array}{cc} a_1 & a_3 \\ b_1 & b_3 \end{array} \right], \tag{3.57}$$

where for each element, a_i and b_i are based on the nodal coordinates x and y and are given by

$$\left[\begin{array}{cc} a_1 & b_1 \\ a_2 & b_2 \\ a_3 & b_3 \end{array} \right] = \frac{1}{4} \left[\begin{array}{cccc} -1 & 1 & 1 & -1 \\ 1 & -1 & 1 & -1 \\ -1 & -1 & 1 & 1 \end{array} \right] \left[\begin{array}{cc} x_1 & y_1 \\ x_2 & y_2 \\ x_3 & y_3 \\ x_4 & y_4 \end{array} \right]. \tag{3.58}$$

The interpolation based on the local $\xi - \eta$ coordinates is given by

$$\boldsymbol{P}^e_{Dh} = \left[\begin{array}{cc} \eta & 0 \\ 0 & \xi \end{array} \right]. \tag{3.59}$$

The interpolation for electric flux density $\boldsymbol{D}^h$ can therefore be given explicitly by

$$\boldsymbol{D}^h = \sum_e \left[\begin{array}{cccc} 1 & 0 & a_1\eta & a_3\xi \\ 0 & 1 & b_1\eta & b_3\xi \end{array} \right] \left\{ \begin{array}{c} \boldsymbol{\beta}^e_{Dc} \\ \boldsymbol{\beta}^e_{Dh} \end{array} \right\}. \tag{3.60}$$

The assumed symmetric part of stress is similarly interpolated as

$$\text{symm}\boldsymbol{T}^h = \sum_e \left[\begin{array}{cc} \boldsymbol{I}^e_{Tc} & \boldsymbol{A}^e_T \boldsymbol{P}^e_{Thn} \end{array} \right] \left\{ \begin{array}{c} \boldsymbol{\beta}^e_{Tc} \\ \boldsymbol{\beta}^e_{Th} \end{array} \right\}, \tag{3.61}$$

where $\boldsymbol{I}^e_{Tc}$ is a 3×3 identity matrix accounting for a constant stress state, with corresponding stress parameters $\boldsymbol{\beta}^e_{Tc}$. $\boldsymbol{A}^e_T$ is a transformation matrix given by

$$\boldsymbol{A}^e_T = \left[\begin{array}{ccc} a_1^2 & a_3^2 & 2a_1a_3 \\ b_1^2 & b_3^2 & 2b_1b_3 \\ a_1b_1 & a_3b_3 & a_1b_3 + a_3b_1 \end{array} \right]. \tag{3.62}$$

There are many other constraint matrices, (see for example Di and Ramm [61]), which can be used, but are not considered here for the sake of brevity. Two different higher order stress interpolations are implemented. The first has 8 (i.e. 5 non-constant) $\boldsymbol{\beta}_T$–parameters and the other 9 (6 non-constant). The element with the 8 $\boldsymbol{\beta}_T$–parameters has a higher order interpolation matrix given by

$$\boldsymbol{P}^e_{Th5} = \left[\begin{array}{ccccc} \eta & 0 & -\xi & 0 & \eta^2 \\ 0 & \xi & 0 & -\eta & -\xi^2 \\ 0 & 0 & \eta & \xi & 0 \end{array} \right], \tag{3.63}$$

which is similar to the field used by Sze and Ghali [50]. The element containing 9 $\boldsymbol{\beta}_T$–parameters has a matrix given by

$$\boldsymbol{P}^e_{Th6} = \begin{bmatrix} \eta & 0 & -\xi & 0 & \eta^2 & 0 \\ 0 & \xi & 0 & -\eta & 0 & \xi^2 \\ 0 & 0 & \eta & \xi & 0 & 0 \end{bmatrix}. \tag{3.64}$$

Alternative interpolations are given by Geyer and Groenwold [43].

3.6 Finite element implementation

For simplicity, in this section the boundary terms are neglected, but may be included in the usual manner. The body charge, q, terms are also neglected, as is usually done [71]. In what is to follow, $\boldsymbol{u}^h, \text{symm}\boldsymbol{T}^h, \text{skew}\boldsymbol{T}^h, \phi^h, \boldsymbol{D}^h$ represent the interpolations for displacement, symmetric and skew-symmetric stress, electric potential and electric flux density, respectively. The fields $\boldsymbol{u}^h$ and ϕ^h satisfy the necessary boundary conditions, and $\boldsymbol{\psi}^h$ denotes the interpolated rotation field.

In our paper [80], due to space considerations, only two elements derived from the foregoing variational formulations are presented. In this section however, all of eight new elements are presented.

3.6.1 Irreducible piezoelectric elements with drilling DOFs

Firstly the two simplest (irreducible) finite elements are presented. The element originating from the functional Π_M is denoted P4dM, while the K-type element derived from Π_K is denoted P4dK.

P4dM element based on Π_M

We proceed by writing the discrete form of the first variation of Π_M in a matrix-like form, similar to the notation used in [18, 21], as

$$\begin{aligned} 0 = &\int_{\Omega^h} (\text{symm}\boldsymbol{\nabla}\delta\boldsymbol{u}^h)^t \cdot \boldsymbol{c}_E \cdot (\text{symm}\boldsymbol{\nabla}\boldsymbol{u}^h)\, \mathrm{d}V + \int_{\Omega^h} (\boldsymbol{\nabla}\delta\phi^h)^t \cdot \boldsymbol{e} \cdot (\text{symm}\boldsymbol{\nabla}\boldsymbol{u}^h)\, \mathrm{d}V \\ &+ \int_{\Omega^h} (\text{symm}\boldsymbol{\nabla}\delta\boldsymbol{u}^h)^t \cdot \boldsymbol{e}^t \cdot (\boldsymbol{\nabla}\phi^h)\, \mathrm{d}V - \int_{\Omega^h} (\boldsymbol{\nabla}\delta\phi^h)^t \cdot \boldsymbol{\epsilon}_S \cdot (\boldsymbol{\nabla}\phi^h)\, \mathrm{d}V \\ &+ \int_{\Omega^h} (\text{skew}\delta\boldsymbol{T}^h)^t \cdot (\text{skew}\boldsymbol{\nabla}\boldsymbol{u}^h - \boldsymbol{\psi}^h)\, \mathrm{d}V + \int_{\Omega^h} (\text{skew}\boldsymbol{\nabla}\delta\boldsymbol{u}^h)^t \cdot \text{skew}\boldsymbol{T}^h \\ &- (\delta\boldsymbol{\psi}^h)^t \cdot \text{skew}\boldsymbol{T}^h\, \mathrm{d}V - \gamma^{-1} \int_{\Omega^h} (\text{skew}\delta\boldsymbol{T}^h)^t \cdot \text{skew}\boldsymbol{T}^h\, \mathrm{d}V - \int_{\Omega^h} (\delta\boldsymbol{u}^h)^t \cdot \boldsymbol{f}\, \mathrm{d}V. \end{aligned} \tag{3.65}$$

Employing the interpolations and operators presented in Section 3.5, (3.65) can be written in matrix notation, as:

$$\begin{bmatrix} \boldsymbol{K}^e_{uu} & \boldsymbol{K}^e_{u\phi} & \boldsymbol{h}^e \\ [\boldsymbol{K}^e_{u\phi}]^t & -\boldsymbol{K}^e_{\phi\phi} & \boldsymbol{0} \\ [\boldsymbol{h}^e]^t & \boldsymbol{0} & -\gamma^{-1}\Omega^e \end{bmatrix} \begin{Bmatrix} \boldsymbol{a} \\ \boldsymbol{\phi} \\ T^e_0 \end{Bmatrix} = \begin{Bmatrix} \boldsymbol{f} \\ \boldsymbol{0} \\ 0 \end{Bmatrix}; \quad \boldsymbol{a} = \begin{Bmatrix} \boldsymbol{u} \\ \boldsymbol{\psi} \end{Bmatrix}. \tag{3.66}$$

The skew symmetric part of the stress tensor can be eliminated on the element level using static condensation, so that the system of equations necessary to solve the problem are

$$\begin{bmatrix} \boldsymbol{K}^e_M \end{bmatrix} \begin{Bmatrix} \boldsymbol{a} \\ \boldsymbol{\phi} \end{Bmatrix} = \begin{Bmatrix} \boldsymbol{f} \\ \boldsymbol{0} \end{Bmatrix}, \tag{3.67}$$

where

$$\boldsymbol{K}^e_M = \begin{bmatrix} \boldsymbol{K}^e_{uu} + \frac{\gamma}{\Omega^e}\boldsymbol{h}^e[\boldsymbol{h}^e]^t & \boldsymbol{K}^e_{u\phi} \\ [\boldsymbol{K}^e_{u\phi}]^t & -\boldsymbol{K}^e_{\phi\phi} \end{bmatrix}. \tag{3.68}$$

Individual partitioned stiffness matrix terms are given in Section 3.7. Both $\boldsymbol{K}^e_{uu}$ and $\boldsymbol{K}^e_{u\phi}$ are evaluated using a 5-point numerical integration scheme, while $\boldsymbol{h}^e$ and $\boldsymbol{K}^e_{\phi\phi}$ employ a standard 4-point scheme. The top left (12×12) portion of the stiffness matrix represents the mechanical part. The 12×4 partition, denoted $\boldsymbol{K}^e_{u\phi}$, represents the piezoelectric part, and the bottom right portion, $-\boldsymbol{K}^e_{\phi\phi}$, the 4×4 dielectric part of the stiffness matrix.

The skew part of the stress tensor (constant over each element) can be recovered as a post-processing step, and is given by

$$T^e_0 = \gamma \frac{[\boldsymbol{h}^e]^t \boldsymbol{a}}{\Omega^e}. \tag{3.69}$$

P4dK element based on Π_K

The element arising from the irreducible K-type functional is now derived. To this end, the discrete form of $\delta\Pi_K$ can be written using the same notation as

$$\begin{aligned} 0 = &\int_{\Omega^h} (\text{symm}\boldsymbol{\nabla}\delta\boldsymbol{u}^h)^t \cdot \boldsymbol{c}_E \cdot (\text{symm}\boldsymbol{\nabla}\boldsymbol{u}^h)\, \mathrm{d}V + \int_{\Omega^h} (\boldsymbol{\nabla}\delta\phi^h)^t \cdot \boldsymbol{e} \cdot (\text{symm}\boldsymbol{\nabla}\boldsymbol{u}^h)\, \mathrm{d}V \\ &+ \int_{\Omega^h} (\text{symm}\boldsymbol{\nabla}\delta\boldsymbol{u}^h)^t \cdot \boldsymbol{e}^t \cdot (\boldsymbol{\nabla}\phi^h)\, \mathrm{d}V - \int_{\Omega^h} (\boldsymbol{\nabla}\delta\phi^h)^t \cdot \boldsymbol{\epsilon}_S \cdot (\boldsymbol{\nabla}\phi^h)\, \mathrm{d}V \\ &+ \gamma \int_{\Omega^h} (\text{skew}\boldsymbol{\nabla}\delta\boldsymbol{u}^h - \delta\boldsymbol{\psi}^h)^t \cdot (\text{skew}\boldsymbol{\nabla}\boldsymbol{u}^h - \boldsymbol{\psi}^h)\, \mathrm{d}V - \int_{\Omega^h} (\delta\boldsymbol{u}^h)^t \cdot \boldsymbol{f}\, \mathrm{d}V. \end{aligned} \tag{3.70}$$

The condensed matrix form of (3.70) can be directly written as:

$$\begin{bmatrix} \boldsymbol{K}^e_K \end{bmatrix} \begin{Bmatrix} \boldsymbol{a} \\ \boldsymbol{\phi} \end{Bmatrix} = \begin{Bmatrix} \boldsymbol{f} \\ \boldsymbol{0} \end{Bmatrix}, \tag{3.71}$$

where the expanded stiffness matrix is explicitly given by:

$$\begin{bmatrix} \boldsymbol{K}^e_K \end{bmatrix} = \begin{bmatrix} \boldsymbol{K}^e_{uu} + \boldsymbol{P}^e & \boldsymbol{K}^e_{u\phi} \\ [\boldsymbol{K}^e_{u\phi}]^t & -\boldsymbol{K}^e_{\phi\phi} \end{bmatrix}. \tag{3.72}$$

The individual partitioned stiffness matrices are again given in Section 3.7. In particular, the matrix $\boldsymbol{P}^e$, which represents the second last term in (3.70), is evaluated using a single point integration scheme.

3.6.2 Fully mixed piezoelectric element with drilling DOFs

The matrix form of the two fully-mixed finite elements can be derived similarly. The two elements are denoted P4dMnTD and P4dKnTD, originating from the M- and K-type fully mixed functionals, respectively. The n in the element denotation reflects the number of stress β parameters.

P4dMnTD element based on Π_M^{TD}

Considering first the M-type element based on Π_M^{TD}, the discrete form of the first variation of the functional can be written as:

$$\begin{aligned}
0 = &- \int_{\Omega^h} (\text{symm}\delta\boldsymbol{T}^h)^t \cdot \boldsymbol{s}_D \cdot (\text{symm}\boldsymbol{T}^h)\, \mathrm{d}V - \int_{\Omega^h} (\delta\boldsymbol{D}^h)^t \cdot \boldsymbol{g} \cdot (\text{symm}\boldsymbol{T}^h)\, \mathrm{d}V \\
&- \int_{\Omega^h} (\text{symm}\delta\boldsymbol{T}^h)^t \cdot \boldsymbol{g}^t \cdot (\boldsymbol{D}^h)\, \mathrm{d}V + \int_{\Omega^h} (\delta\boldsymbol{D}^h)^t \cdot \boldsymbol{\chi}_T \cdot (\boldsymbol{D}^h)\, \mathrm{d}V \\
&+ \int_{\Omega^h} (\text{symm}\delta\boldsymbol{T}^h)^t \cdot (\text{symm}\boldsymbol{\nabla}\boldsymbol{u}^h)\, \mathrm{d}V + \int_{\Omega^h} (\text{symm}\boldsymbol{\nabla}\delta\boldsymbol{u}^h)^t \cdot (\text{symm}\boldsymbol{T}^h)\, \mathrm{d}V \\
&+ \int_{\Omega^h} (\delta\boldsymbol{D}^h)^t \cdot (\boldsymbol{\nabla}\phi^h)\, \mathrm{d}V + \int_{\Omega^h} (\boldsymbol{\nabla}\delta\phi^h)^t \cdot (\delta\boldsymbol{D}^h)\, \mathrm{d}V \\
&+ \int_{\Omega^h} (\text{skew}\delta\boldsymbol{T}^h)^t \cdot (\text{skew}\boldsymbol{\nabla}\boldsymbol{u}^h - \boldsymbol{\psi}^h)\, \mathrm{d}V \\
&+ \int_{\Omega^h} (\text{skew}\boldsymbol{\nabla}\delta\boldsymbol{u}^h)^t \cdot \text{skew}\boldsymbol{T}^h - (\delta\boldsymbol{\psi}^h)^t \cdot \text{skew}\boldsymbol{T}^h\, \mathrm{d}V \\
&- \gamma^{-1} \int_{\Omega^h} (\text{skew}\delta\boldsymbol{T}^h)^t \cdot \text{skew}\boldsymbol{T}^h\, \mathrm{d}V - \int_{\Omega^h} (\delta\boldsymbol{u}^h)^t \cdot \boldsymbol{f}\, \mathrm{d}V.
\end{aligned} \tag{3.73}$$

The discrete version of the formulation can again be rewritten in matrix form as

$$\begin{bmatrix}
\boldsymbol{0} & \boldsymbol{0} & \boldsymbol{h}^e & \boldsymbol{K}^e_{uT} & \boldsymbol{0} \\
\boldsymbol{0} & \boldsymbol{0} & \boldsymbol{0} & \boldsymbol{0} & \boldsymbol{K}^e_{\phi D} \\
[\boldsymbol{h}^e]^t & \boldsymbol{0} & -\gamma^{-1}\Omega^e & \boldsymbol{0} & \boldsymbol{0} \\
[\boldsymbol{K}^e_{uT}]^t & \boldsymbol{0} & \boldsymbol{0} & -\boldsymbol{K}^{TDe}_{TT} & -\boldsymbol{K}^{TDe}_{TD} \\
\boldsymbol{0} & [\boldsymbol{K}^e_{\phi D}]^t & \boldsymbol{0} & -[\boldsymbol{K}^{TDe}_{TD}]^t & \boldsymbol{K}^{TDe}_{DD}
\end{bmatrix}
\begin{Bmatrix} \boldsymbol{a} \\ \boldsymbol{\phi} \\ T^e_0 \\ \boldsymbol{\beta}^{TDe}_T \\ \boldsymbol{\beta}^{TDe}_D \end{Bmatrix}
= \begin{Bmatrix} \boldsymbol{f} \\ \boldsymbol{0} \\ 0 \\ \boldsymbol{0} \\ \boldsymbol{0} \end{Bmatrix}. \tag{3.74}$$

This matrix form can be further condensed by eliminating T^e_0, $\boldsymbol{\beta}^{TDe}_T$ and $\boldsymbol{\beta}^{TDe}_D$ using static condensation to arrive at:

$$\begin{bmatrix} \boldsymbol{K}^{TDe}_M \end{bmatrix} \begin{Bmatrix} \boldsymbol{a} \\ \boldsymbol{\phi} \end{Bmatrix} = \begin{Bmatrix} \boldsymbol{f} \\ \boldsymbol{0} \end{Bmatrix}, \tag{3.75}$$

where the stress and electric flux density β-parameters can be shown to be

$$\left\{ \begin{array}{c} \boldsymbol{\beta}_T^{TDe} \\ \boldsymbol{\beta}_D^{TDe} \end{array} \right\} = \left[\begin{array}{cc} \boldsymbol{K}_{TT}^{TDe} & \boldsymbol{K}_{TD}^{TDe} \\ [\boldsymbol{K}_{TD}^{TDe}]^t & -\boldsymbol{K}_{DD}^{TDe} \end{array} \right]^{-1} \left[\begin{array}{cc} [\boldsymbol{K}_{uT}^{e}]^t & \boldsymbol{0} \\ \boldsymbol{0} & [\boldsymbol{K}_{\phi D}^{e}]^t \end{array} \right] \left\{ \begin{array}{c} \boldsymbol{a} \\ \boldsymbol{\phi} \end{array} \right\}, \tag{3.76}$$

T_0^e is again given by (3.69), and the stiffness matrix for this element can be written as

$$\boldsymbol{K}_M^{TDe} = \left[\begin{array}{cc} \frac{\gamma}{\Omega^e} \boldsymbol{h}^e [\boldsymbol{h}^e]^t & \boldsymbol{0} \\ \boldsymbol{0} & \boldsymbol{0} \end{array} \right] + \left[\begin{array}{cc} \boldsymbol{K}_{uT}^{e} & \boldsymbol{0} \\ \boldsymbol{0} & \boldsymbol{K}_{\phi D}^{e} \end{array} \right] \left[\begin{array}{cc} \boldsymbol{K}_{TT}^{TDe} & \boldsymbol{K}_{TD}^{TDe} \\ [\boldsymbol{K}_{TD}^{TDe}]^t & -\boldsymbol{K}_{DD}^{TDe} \end{array} \right]^{-1} \left[\begin{array}{cc} [\boldsymbol{K}_{uT}^{e}]^t & \boldsymbol{0} \\ \boldsymbol{0} & [\boldsymbol{K}_{\phi D}^{e}]^t \end{array} \right]. \tag{3.77}$$

Again, individual partitioned stiffness matrix terms are given in Section 3.7. The partitioned submatrices $\boldsymbol{K}_{uT}^e$, $\boldsymbol{K}_{TT}^{TDe}$ and $\boldsymbol{K}_{TD}^{TDe}$ are calculated using a 5-point integration scheme, while $\boldsymbol{K}_{\phi D}^e$ and $\boldsymbol{K}_{DD}^{TDe}$ are evaluated using a 4-point scheme. The number of stress parameters in $\boldsymbol{\beta}_T^e$ (either 8 or 9) is denoted n in the element designation P4dMnTD.

P4dKnTD element based on Π_K^{TD}

Focusing now on the K-type fully mixed element, the discrete form of the variational equation derived from Π_K^{TD} can be derived as:

$$\begin{aligned} 0 = &- \int_{\Omega^h} (\text{symm}\delta\boldsymbol{T}^h)^t \cdot \boldsymbol{s}_D \cdot (\text{symm}\boldsymbol{T}^h)\, \text{d}V - \int_{\Omega^h} (\delta\boldsymbol{D}^h)^t \cdot \boldsymbol{g} \cdot (\text{symm}\boldsymbol{T}^h)\, \text{d}V \\ &- \int_{\Omega^h} (\text{symm}\delta\boldsymbol{T}^h)^t \cdot \boldsymbol{g}^t \cdot (\boldsymbol{D}^h)\, \text{d}V + \int_{\Omega^h} (\delta\boldsymbol{D}^h)^t \cdot \boldsymbol{\chi}_T \cdot (\boldsymbol{D}^h)\, \text{d}V \\ &+ \int_{\Omega^h} (\text{symm}\delta\boldsymbol{T}^h)^t \cdot (\text{symm}\boldsymbol{\nabla}\boldsymbol{u}^h)\, \text{d}V + \int_{\Omega^h} (\text{symm}\boldsymbol{\nabla}\delta\boldsymbol{u}^h)^t \cdot (\text{symm}\boldsymbol{T}^h)\, \text{d}V \\ &+ \int_{\Omega^h} (\delta\boldsymbol{D}^h)^t \cdot (\boldsymbol{\nabla}\phi^h)\, \text{d}V + \int_{\Omega^h} (\boldsymbol{\nabla}\delta\phi^h)^t \cdot (\delta\boldsymbol{D}^h)\, \text{d}V \\ &+ \gamma \int_{\Omega^h} (\text{skew}\boldsymbol{\nabla}\delta\boldsymbol{u}^h - \delta\boldsymbol{\psi}^h)^t \cdot (\text{skew}\boldsymbol{\nabla}\boldsymbol{u}^h - \boldsymbol{\psi}^h)\, \text{d}V - \int_{\Omega^h} (\delta\boldsymbol{u}^h)^t \cdot \boldsymbol{f}\, \text{d}V. \end{aligned} \tag{3.78}$$

The matrix form of the discrete variational equation becomes

$$\left[\begin{array}{cccc} \boldsymbol{P}^e & \boldsymbol{0} & \boldsymbol{K}_{uT}^e & \boldsymbol{0} \\ \boldsymbol{0} & \boldsymbol{0} & \boldsymbol{0} & \boldsymbol{K}_{\phi D}^e \\ [\boldsymbol{K}_{uT}^e]^t & \boldsymbol{0} & -\boldsymbol{K}_{TT}^{TDe} & -\boldsymbol{K}_{TD}^{TDe} \\ \boldsymbol{0} & [\boldsymbol{K}_{\phi D}^e]^t & -[\boldsymbol{K}_{TD}^{TDe}]^t & \boldsymbol{K}_{DD}^{TDe} \end{array} \right] \left[\begin{array}{c} \boldsymbol{a} \\ \boldsymbol{\phi} \\ \boldsymbol{\beta}_T^{TDe} \\ \boldsymbol{\beta}_D^{TDe} \end{array} \right] = \left[\begin{array}{c} \boldsymbol{f} \\ \boldsymbol{0} \\ \boldsymbol{0} \\ \boldsymbol{0} \end{array} \right]. \tag{3.79}$$

The stiffness matrix can be compacted by condensing $\boldsymbol{\beta}_T^{TDe}$ and $\boldsymbol{\beta}_D^{TDe}$ out on the element level, resulting in:

$$\left[\boldsymbol{K}_K^{TDe} \right] \left\{ \begin{array}{c} \boldsymbol{a} \\ \boldsymbol{\phi} \end{array} \right\} = \left\{ \begin{array}{c} \boldsymbol{f} \\ \boldsymbol{0} \end{array} \right\}, \tag{3.80}$$

with the β-parameters, given by (3.76) and the stiffness matrix given by

$$\boldsymbol{K}_K^{TDe} = \begin{bmatrix} \boldsymbol{P}^e & \boldsymbol{0} \\ \boldsymbol{0} & \boldsymbol{0} \end{bmatrix} + \begin{bmatrix} \boldsymbol{K}_{uT}^e & \boldsymbol{0} \\ \boldsymbol{0} & \boldsymbol{K}_{\phi D}^e \end{bmatrix} \begin{bmatrix} \boldsymbol{K}_{TT}^{TDe} & \boldsymbol{K}_{TD}^{TDe} \\ (\boldsymbol{K}_{TD}^{TDe})^t & -\boldsymbol{K}_{DD}^{TDe} \end{bmatrix}^{-1} \begin{bmatrix} [\boldsymbol{K}_{uT}^e]^t & \boldsymbol{0} \\ \boldsymbol{0} & [\boldsymbol{K}_{\phi D}^e]^t \end{bmatrix}. \tag{3.81}$$

Once again, individual stiffness sub-matrices are given explicitly in Section 3.7. The integration schemes used are as given previously, and again the number of stress β-parameters n, is included in the element designation.

3.6.3 Degenerate assumed flux density piezoelectric element with drilling DOFs

The degenerate assumed flux density piezoelectric elements with drilling DOFs, emanating from functions Π_M^D and Π_K^D, denoted P4dMD and P4dKD, respectively are now detailed.

P4dMD element based on Π_M^D

Considering the M-type degenerate element formulation with assumed electric flux density, the discrete version of the resulting variational equation can be written as

$$\begin{aligned} 0 = &\int_{\Omega^h} (\text{symm}\boldsymbol{\nabla}\delta\boldsymbol{u}^h)^t \cdot \boldsymbol{c}_D \cdot (\text{symm}\boldsymbol{\nabla}\boldsymbol{u}^h)\,\mathrm{d}V - \int_{\Omega^h} (\delta\boldsymbol{D}^h)^t \cdot \boldsymbol{h} \cdot (\text{symm}\boldsymbol{\nabla}\boldsymbol{u}^h)\,\mathrm{d}V \\ &- \int_{\Omega^h} (\text{symm}\boldsymbol{\nabla}\delta\boldsymbol{u}^h)^t \cdot \boldsymbol{h}^t \cdot (\boldsymbol{D}^h)\,\mathrm{d}V + \int_{\Omega^h} (\delta\boldsymbol{D}^h)^t \cdot \boldsymbol{\chi}_S \cdot (\boldsymbol{D}^h)\,\mathrm{d}V \\ &+ \int_{\Omega^h} (\delta\boldsymbol{D}^h)^t \cdot (\boldsymbol{\nabla}\phi^h)\,\mathrm{d}V + \int_{\Omega^h} (\boldsymbol{\nabla}\delta\phi^h)^t \cdot (\boldsymbol{D}^h)\,\mathrm{d}V \\ &+ \int_{\Omega^h} (\text{skew}\delta\boldsymbol{T}^h)^t \cdot (\text{skew}\boldsymbol{\nabla}\boldsymbol{u}^h - \boldsymbol{\psi}^h)\,\mathrm{d}V + \int_{\Omega^h} (\text{skew}\boldsymbol{\nabla}\delta\boldsymbol{u}^h)^t \cdot \text{skew}\boldsymbol{T}^h \\ &- (\delta\boldsymbol{\psi}^h)^t \cdot \text{skew}\boldsymbol{T}^h\,\mathrm{d}V - \gamma^{-1}\int_{\Omega^h} (\text{skew}\delta\boldsymbol{T}^h)^t \cdot \text{skew}\boldsymbol{T}^h\,\mathrm{d}V - \int_{\Omega^h} (\delta\boldsymbol{u}^h)^t \cdot \boldsymbol{f}\,\mathrm{d}V. \end{aligned} \tag{3.82}$$

This equation can once again be rewritten in matrix form using the element operators, detailed in Section 3.4.4, as

$$\begin{bmatrix} \boldsymbol{K}_{uu}^{De} & \boldsymbol{0} & \boldsymbol{h}^e & -\boldsymbol{K}_{uD}^e \\ \boldsymbol{0} & \boldsymbol{0} & \boldsymbol{0} & \boldsymbol{K}_{\phi D}^e \\ [\boldsymbol{h}^e]^t & \boldsymbol{0} & -\gamma^{-1}\Omega^e & \boldsymbol{0} \\ -[\boldsymbol{K}_{uD}^e]^t & [\boldsymbol{K}_{\phi D}^e]^t & \boldsymbol{0} & \boldsymbol{K}_{DD}^{De} \end{bmatrix} \begin{Bmatrix} \boldsymbol{a} \\ \boldsymbol{\phi} \\ T_0^e \\ \boldsymbol{\beta}_D^{De} \end{Bmatrix} = \begin{Bmatrix} \boldsymbol{f} \\ \boldsymbol{0} \\ 0 \\ \boldsymbol{0} \end{Bmatrix}. \tag{3.83}$$

The expanded matrix form given in (3.83) can be written in terms of only kinematic-like variables by condensing out all additional terms as

$$\left[\ \boldsymbol{K}_M^{De}\ \right]\left\{\begin{array}{c}\boldsymbol{a}\\ \boldsymbol{\phi}\end{array}\right\}=\left\{\begin{array}{c}\boldsymbol{f}\\ \boldsymbol{0}\end{array}\right\}, \tag{3.84}$$

where the electric flux density β-parameters are

$$\boldsymbol{\beta}_D^{De}=[\boldsymbol{K}_{DD}^{De}]^{-1}[(\boldsymbol{K}_{uD}^{e})^t-(\boldsymbol{K}_{\phi D}^{e})^t]\left\{\begin{array}{c}\boldsymbol{a}\\ \boldsymbol{\phi}\end{array}\right\}, \tag{3.85}$$

and the condensed stiffness matrix is given by

$$\boldsymbol{K}_M^{De}=\left[\begin{array}{cc}\boldsymbol{K}_{uu}^{De}+\frac{\gamma}{\Omega^e}\boldsymbol{h}^e[\boldsymbol{h}^e]^t & \boldsymbol{0}\\ \boldsymbol{0} & \boldsymbol{0}\end{array}\right]-\left[\begin{array}{c}\boldsymbol{K}_{uD}^{e}\\ -\boldsymbol{K}_{\phi D}^{e}\end{array}\right][\boldsymbol{K}_{DD}^{De}]^{-1}\left[\ (\boldsymbol{K}_{uD}^{e})^t-(\boldsymbol{K}_{\phi D}^{e})^t\ \right]. \tag{3.86}$$

The sub-matrices $\boldsymbol{K}_{uu}^{De}$ and $\boldsymbol{K}_{uD}^{e}$ are both evaluated using a 5-point integration scheme, while $\boldsymbol{K}_{DD}^{De}$ is computed using a standard 4-point scheme. Expressions for these matrices are explicitly given in Section 3.7.

P4dKD element based on Π_K^D

The K-type equivalent variational equation with assumed electric flux density can be calculated as

$$\begin{aligned}0=&\int_{\Omega^h}(\mathrm{symm}\boldsymbol{\nabla}\delta\boldsymbol{u}^h)^t\cdot\boldsymbol{c}_D\cdot(\mathrm{symm}\boldsymbol{\nabla}\boldsymbol{u}^h)\,\mathrm{d}V-\int_{\Omega^h}(\delta\boldsymbol{D}^h)^t\cdot\boldsymbol{h}\cdot(\mathrm{symm}\boldsymbol{\nabla}\boldsymbol{u}^h)\,\mathrm{d}V\\&-\int_{\Omega^h}(\mathrm{symm}\boldsymbol{\nabla}\delta\boldsymbol{u}^h)^t\cdot\boldsymbol{h}^t\cdot(\boldsymbol{D}^h)\,\mathrm{d}V+\int_{\Omega^h}(\delta\boldsymbol{D}^h)^t\cdot\boldsymbol{\chi}_S\cdot(\boldsymbol{D}^h)\,\mathrm{d}V\\&+\int_{\Omega^h}(\delta\boldsymbol{D}^h)^t\cdot(\boldsymbol{\nabla}\phi^h)\,\mathrm{d}V+\int_{\Omega^h}(\boldsymbol{\nabla}\delta\phi^h)^t\cdot(\boldsymbol{D}^h)\,\mathrm{d}V\\&+\gamma\int_{\Omega^h}(\mathrm{skew}\boldsymbol{\nabla}\delta\boldsymbol{u}^h-\delta\boldsymbol{\psi}^h)^t\cdot(\mathrm{skew}\boldsymbol{\nabla}\boldsymbol{u}^h-\boldsymbol{\psi}^h)\,\mathrm{d}V-\int_{\Omega^h}(\delta\boldsymbol{u}^h)^t\cdot\boldsymbol{f}\,\mathrm{d}V.\end{aligned} \tag{3.87}$$

The matrix form of (3.87) becomes

$$\left[\begin{array}{ccc}\boldsymbol{K}_{uu}^{De}+\boldsymbol{P}^e & \boldsymbol{0} & -\boldsymbol{K}_{uD}^{e}\\ \boldsymbol{0} & \boldsymbol{0} & \boldsymbol{K}_{\phi D}^{e}\\ -[\boldsymbol{K}_{uD}^{e}]^t & [\boldsymbol{K}_{\phi D}^{e}]^t & \boldsymbol{K}_{DD}^{De}\end{array}\right]\left\{\begin{array}{c}\boldsymbol{a}\\ \boldsymbol{\phi}\\ \boldsymbol{\beta}_D^{De}\end{array}\right\}=\left\{\begin{array}{c}\boldsymbol{f}\\ \boldsymbol{0}\\ \boldsymbol{0}\end{array}\right\}. \tag{3.88}$$

Again, the matrix form in (3.88) is simplified to include only kinematic variables as

$$\left[\ \boldsymbol{K}_K^{De}\ \right]\left\{\begin{array}{c}\boldsymbol{a}\\ \boldsymbol{\phi}\end{array}\right\}=\left\{\begin{array}{c}\boldsymbol{f}\\ \boldsymbol{0}\end{array}\right\}, \tag{3.89}$$

where the same electric flux density β-parameters as (3.85) result. In this case, the simplified stiffness matrix is

$$\boldsymbol{K}_K^{De} = \begin{bmatrix} \boldsymbol{K}_{uu}^{De} + \boldsymbol{P}^e & \boldsymbol{0} \\ \boldsymbol{0} & \boldsymbol{0} \end{bmatrix} - \begin{bmatrix} \boldsymbol{K}_{uD}^e \\ -\boldsymbol{K}_{\phi D}^e \end{bmatrix} [\boldsymbol{K}_{DD}^{De}]^{-1} \begin{bmatrix} (\boldsymbol{K}_{uD}^e)^t - (\boldsymbol{K}_{\phi D}^e)^t \end{bmatrix}, \tag{3.90}$$

with individual stiffness matrix terms presented in Section 3.7. The same integration schemes as used previously are again employed here to evaluate individual sub-matrices.

3.6.4 Degenerate assumed stress piezoelectric elements with drilling DOFs

Finally, the assumed stress degenerate mixed elements are presented. These elements are denoted P4dMnT and P4dKnT, and arise from Π_M^T and Π_K^T, respectively. Again, the n in the element designation denotes the number of stress parameters employed. Of course 'assumed stress' refers specifically to the assumed symmetric part of stress since all M-type elements contain an assumed skew-symmetric stress.

P4dMnT element based on Π_M^T

The assumed stress degenerate Hellinger-Reissner like variational equation in discrete form is given by

$$\begin{aligned} 0 = &- \int_{\Omega^h} (\text{symm}\delta\boldsymbol{T}^h)^t \cdot \boldsymbol{s}_E \cdot (\text{symm}\boldsymbol{T}^h)\, \text{d}V + \int_{\Omega^h} (\boldsymbol{\nabla}\delta\phi^h)^t \cdot \boldsymbol{d} \cdot (\text{symm}\boldsymbol{T}^h)\, \text{d}V \\ &+ \int_{\Omega^h} (\text{symm}\delta\boldsymbol{T}^h)^t \cdot \boldsymbol{d}^t \cdot (\boldsymbol{\nabla}\phi^h)\, \text{d}V - \int_{\Omega^h} (\boldsymbol{\nabla}\delta\phi^h)^t \cdot \boldsymbol{\epsilon}_T \cdot (\boldsymbol{\nabla}\phi^h)\, \text{d}V \\ &+ \int_{\Omega^h} (\text{symm}\delta\boldsymbol{T}^h)^t \cdot (\text{symm}\boldsymbol{\nabla}\boldsymbol{u}^h)\, \text{d}V + \int_{\Omega^h} (\text{symm}\boldsymbol{\nabla}\delta\boldsymbol{u}^h)^t \cdot (\text{symm}\boldsymbol{T}^h)\, \text{d}V \\ &+ \int_{\Omega^h} (\text{skew}\delta\boldsymbol{T}^h)^t \cdot (\text{skew}\boldsymbol{\nabla}\boldsymbol{u}^h - \boldsymbol{\psi}^h)\, \text{d}V + \int_{\Omega^h} (\text{skew}\boldsymbol{\nabla}\delta\boldsymbol{u}^h)^t \cdot \text{skew}\boldsymbol{T}^h \\ &- (\delta\boldsymbol{\psi}^h)^t \cdot \text{skew}\boldsymbol{T}^h\, \text{d}V - \gamma^{-1} \int_{\Omega^h} (\text{skew}\delta\boldsymbol{T}^h)^t \cdot \text{skew}\boldsymbol{T}^h\, \text{d}V - \int_{\Omega^h} (\delta\boldsymbol{u}^h)^t \cdot \boldsymbol{f}\, \text{d}V. \end{aligned} \tag{3.91}$$

Yet again, the expression in (3.91) can be rewritten in matrix form as

$$\begin{bmatrix} \boldsymbol{0} & \boldsymbol{0} & \boldsymbol{h}^e & \boldsymbol{K}_{uT}^e \\ \boldsymbol{0} & -\boldsymbol{K}_{\phi\phi}^{Te} & \boldsymbol{0} & \boldsymbol{K}_{\phi T}^e \\ [\boldsymbol{h}^e]^t & \boldsymbol{0} & -\gamma^{-1}\Omega^e & \boldsymbol{0} \\ [\boldsymbol{K}_{uT}^e]^t & [\boldsymbol{K}_{\phi T}^e]^t & \boldsymbol{0} & -\boldsymbol{K}_{TT}^{Te} \end{bmatrix} \begin{Bmatrix} \boldsymbol{a} \\ \boldsymbol{\phi} \\ T_0^e \\ \boldsymbol{\beta}_T^{Te} \end{Bmatrix} = \begin{Bmatrix} \boldsymbol{f} \\ \boldsymbol{0} \\ 0 \\ \boldsymbol{0} \end{Bmatrix}. \tag{3.92}$$

The matrix form in (3.92) is again rewritten in simplified form as

$$\left[\ \boldsymbol{K}_M^{Te}\ \right]\left\{\begin{array}{c}\boldsymbol{a}\\ \boldsymbol{\phi}\end{array}\right\}=\left\{\begin{array}{c}\boldsymbol{f}\\ \boldsymbol{0}\end{array}\right\}, \tag{3.93}$$

where the stress β-parameters are found to be

$$\boldsymbol{\beta}_M^T=[\boldsymbol{K}_{TT}^{Te}]^{-1}[(\boldsymbol{K}_{uT}^e)^t+(\boldsymbol{K}_{\phi T}^e)^t]\left\{\begin{array}{c}\boldsymbol{a}\\ \boldsymbol{\phi}\end{array}\right\}. \tag{3.94}$$

Finally, the condensed stiffness matrix is written as

$$\boldsymbol{K}_M^{Te}=\left[\begin{array}{cc}\frac{\gamma}{\Omega^e}\boldsymbol{h}^e[\boldsymbol{h}^e]^t & \boldsymbol{0}\\ \boldsymbol{0} & -\boldsymbol{K}_{\phi\phi}^{Te}\end{array}\right]+\left[\begin{array}{c}\boldsymbol{K}_{uT}^e\\ \boldsymbol{K}_{\phi T}^e\end{array}\right][\boldsymbol{K}_{TT}^{Te}]^{-1}\left[\begin{array}{cc}(\boldsymbol{K}_{uT}^e)^t & (\boldsymbol{K}_{\phi T}^e)^t\end{array}\right]. \tag{3.95}$$

The submatrices $\boldsymbol{K}_{TT}^{Te}$ and $\boldsymbol{K}_{\phi T}^e$ are evaluated with a 5-point integration scheme, while the term $\boldsymbol{K}_{\phi\phi}^{Te}$ employs a 4-point scheme. Expressions for these terms are contained in Section 3.7.

P4dKnT element based on Π_K^T

The last element implementation is based on the assumed stress K-type Hellinger-Reissner like functional. The first variation of Π_K^T can be expressed in discrete form as

$$\begin{aligned}0=&-\int_{\Omega^h}(\mathrm{symm}\delta\boldsymbol{T}^h)^t\cdot\boldsymbol{s}_E\cdot(\mathrm{symm}\boldsymbol{T}^h)\,\mathrm{d}V+\int_{\Omega^h}(\boldsymbol{\nabla}\delta\phi^h)^t\cdot\boldsymbol{d}\cdot(\mathrm{symm}\boldsymbol{T}^h)\,\mathrm{d}V\\&+\int_{\Omega^h}(\mathrm{symm}\delta\boldsymbol{T}^h)^t\cdot\boldsymbol{d}^t\cdot(\boldsymbol{\nabla}\phi^h)\,\mathrm{d}V-\int_{\Omega^h}(\boldsymbol{\nabla}\delta\phi^h)^t\cdot\boldsymbol{\epsilon}_T\cdot(\boldsymbol{\nabla}\phi^h)\,\mathrm{d}V\\&+\int_{\Omega^h}(\mathrm{symm}\delta\boldsymbol{T}^h)^t\cdot(\mathrm{symm}\boldsymbol{\nabla}\boldsymbol{u}^h)\,\mathrm{d}V+\int_{\Omega^h}(\mathrm{symm}\boldsymbol{\nabla}\delta\boldsymbol{u}^h)^t\cdot(\mathrm{symm}\boldsymbol{T}^h)\,\mathrm{d}V\\&+\gamma\int_{\Omega^h}(\mathrm{skew}\boldsymbol{\nabla}\delta\boldsymbol{u}^h-\delta\boldsymbol{\psi}^h)^t\cdot(\mathrm{skew}\boldsymbol{\nabla}\boldsymbol{u}^h-\boldsymbol{\psi}^h)\,\mathrm{d}V-\int_{\Omega^h}(\delta\boldsymbol{u}^h)^t\cdot\boldsymbol{f}\,\mathrm{d}V.\end{aligned} \tag{3.96}$$

This expression can once yet again be written in matrix form as

$$\left[\begin{array}{ccc}\boldsymbol{P}^e & \boldsymbol{0} & \boldsymbol{K}_{uT}^e\\ \boldsymbol{0} & -\boldsymbol{K}_{\phi\phi}^{Te} & \boldsymbol{K}_{\phi T}^e\\ [\boldsymbol{K}_{uT}^e]^t & [\boldsymbol{K}_{\phi T}^e]^t & -\boldsymbol{K}_{TT}^{Te}\end{array}\right]\left\{\begin{array}{c}\boldsymbol{a}\\ \boldsymbol{\phi}\\ \boldsymbol{\beta}_T^{Te}\end{array}\right\}=\left\{\begin{array}{c}\boldsymbol{f}\\ \boldsymbol{0}\\ \boldsymbol{0}\end{array}\right\}. \tag{3.97}$$

The matrix form of (3.97) is finally simplified to

$$\left[\ \boldsymbol{K}_K^{Te}\ \right]\left\{\begin{array}{c}\boldsymbol{a}\\ \boldsymbol{\phi}\end{array}\right\}=\left\{\begin{array}{c}\boldsymbol{f}\\ \boldsymbol{0}\end{array}\right\}, \tag{3.98}$$

where the condensed stress β-parameters are given by (3.94), and the simplified element stiffness matrix is given by

$$\boldsymbol{K}_K^{Te} = \begin{bmatrix} \boldsymbol{P}^e & \boldsymbol{0} \\ \boldsymbol{0} & -\boldsymbol{K}_{\phi\phi}^{Te} \end{bmatrix} + \begin{bmatrix} \boldsymbol{K}_{uT}^e \\ \boldsymbol{K}_{\phi T}^e \end{bmatrix} [\boldsymbol{K}_{TT}^{Te}]^{-1} \begin{bmatrix} (\boldsymbol{K}_{uT}^e)^t & (\boldsymbol{K}_{\phi T}^e)^t \end{bmatrix}. \tag{3.99}$$

The components of the stiffness matrix are yet again presented in Section 3.7.

3.7 Partitioned stiffness matrices

In Section 3.6 expressions for the individual partitioned sub-matrices were omitted. For the convenience of the reader, it was chosen instead to present all partitioned sub-matrices together for easier reference. The partitioned stiffness matrices are therefore all given here in matrix form by:

$$\boldsymbol{K}_{uu}^{e\ (5)} = \int_{\Omega^e} [\boldsymbol{B}_u^e \quad \boldsymbol{G}_u^e]^t \boldsymbol{c}_E [\boldsymbol{B}_u^e \quad \boldsymbol{G}_u^e]\, \mathrm{d}V, \tag{3.100}$$

$$\boldsymbol{K}_{u\phi}^{e\ (5)} = \int_{\Omega^e} [\boldsymbol{B}_u^e \quad \boldsymbol{G}_u^e]^t \boldsymbol{e}^t [\boldsymbol{B}_\phi^e]\, \mathrm{d}V, \tag{3.101}$$

$$\boldsymbol{K}_{\phi\phi}^{e\ (4)} = \int_{\Omega^e} [\boldsymbol{B}_\phi^e]^t \boldsymbol{\epsilon}_S [\boldsymbol{B}_\phi^e]\, \mathrm{d}V, \tag{3.102}$$

$$\boldsymbol{h}^{e\ (4)} = \int_{\Omega^e} [\boldsymbol{b}^e \quad \boldsymbol{g}^e]^t\, \mathrm{d}V, \tag{3.103}$$

$$\boldsymbol{K}_{uu}^{De\ (5)} = \int_{\Omega^e} [\boldsymbol{B}_u^e \quad \boldsymbol{G}_u^e]^t \boldsymbol{c}_D [\boldsymbol{B}_u^e \quad \boldsymbol{G}_u^e]\, \mathrm{d}V, \tag{3.104}$$

$$\boldsymbol{K}_{uD}^{e\ (5)} = \int_{\Omega^e} [\boldsymbol{B}_u^e \quad \boldsymbol{G}_u^e]^t \boldsymbol{h}^t [\boldsymbol{P}_D^e]\, \mathrm{d}V, \tag{3.105}$$

$$\boldsymbol{K}_{\phi D}^{e\ (4)} = \int_{\Omega^e} [\boldsymbol{B}_\phi^e]^t [\boldsymbol{P}_D^e]\, \mathrm{d}V, \tag{3.106}$$

$$\boldsymbol{K}_{DD}^{De\ (4)} = \int_{\Omega^e} [\boldsymbol{P}_D^e]^t \boldsymbol{\chi}_S [\boldsymbol{P}_D^e]\, \mathrm{d}V, \tag{3.107}$$

$$\boldsymbol{K}_{\phi T}^{e\ (5)} = \int_{\Omega^e} [\boldsymbol{B}_\phi^e]^t \boldsymbol{d} [\boldsymbol{P}_T^e]\, \mathrm{d}V, \tag{3.108}$$

$$\boldsymbol{K}_{\phi\phi}^{Te\ (4)} = \int_{\Omega^e} [\boldsymbol{B}_\phi^e]^t \boldsymbol{\epsilon}_T [\boldsymbol{B}_\phi^e]\, \mathrm{d}V, \tag{3.109}$$

$$\boldsymbol{K}_{uT}^{e\ (5)} = \int_{\Omega^e} [\boldsymbol{B}_u^e \quad \boldsymbol{G}_u^e]^t [\boldsymbol{P}_T^e]\, \mathrm{d}V, \tag{3.110}$$

$$\boldsymbol{K}_{TT}^{Te\ (5)} = \int_{\Omega^e} [\boldsymbol{P}_T^e]^t \boldsymbol{s}_E [\boldsymbol{P}_T^e]\, \mathrm{d}V, \tag{3.111}$$

$$\boldsymbol{K}_{TD}^{TDe\ (5)} = \int_{\Omega^e} [\boldsymbol{P}_T^e]^t \boldsymbol{g}^t [\boldsymbol{P}_D^e]\, \mathrm{d}V, \tag{3.112}$$

$$\boldsymbol{K}_{TT}^{TDe\ (5)} = \int_{\Omega^e} [\boldsymbol{P}_T^e]^t \boldsymbol{s}_D [\boldsymbol{P}_T^e]\, \mathrm{d}V, \tag{3.113}$$

$$\boldsymbol{K}_{DD}^{TDe\ (4)} = \int_{\Omega^e} [\boldsymbol{P}_D^e]^t \boldsymbol{\chi}_T [\boldsymbol{P}_D^e]\, \mathrm{d}V, \tag{3.114}$$

and finally,

$$\boldsymbol{P}^{e\ (1)} = \gamma \int_{\Omega^e} [\boldsymbol{b}^e \quad \boldsymbol{g}^e]^t [\boldsymbol{b}^e \quad \boldsymbol{g}^e]\, \mathrm{d}V. \tag{3.115}$$

The superscript in parentheses $^{(\cdot)}$ represents the number of integration points used to perform the numerical integration over the element area. (The elements are assumed to be homogeneous and have constant area profile through the thickness. Analytical through thickness integration is thus employed.)

3.8 Numerical evaluation

In this section, the developed piezoelectric finite elements are assessed numerically and compared with existing elements. The effect of selected parameters are also quantified. Unlike in our paper where, for brevity, only the two elements were reported on, in this section the performance of all eight new elements is evaluated. The elements used in the comparison are denoted as follows:

Elements without drilling DOFs

Existing elements from literature were implemented, against which our new elements are benchmarked. These existing elements are denoted as follows:

- P4 – A standard, planar 4 node, quadrilateral piezoelectric element without drilling DOFs. Only the displacement $\boldsymbol{u}$ and the potential ϕ interpolated for, see for example [69].
- P4D – A mixed 4 node element with only electric flux density $\boldsymbol{D}$ assumed additionally to displacement and electric potential, as proposed in [76]. The same electric flux density interpolation (with four β-parameters) as in Section 3.5 is employed.
- P4T – A mixed 4 node element with only stress $\boldsymbol{T}$ assumed additionally to displacement and electric potential, as proposed in [76]. In this case, an interpolation with only five stress β-parameters is required. The standard stress interpolation of, for instance Di and Ramm [61] is employed.
- P4TD – A mixed 4 node element with both stress $\boldsymbol{T}$ and electric flux density $\boldsymbol{D}$ assumed additionally to displacement and electric potential, as proposed in [65]. An interpolation for electric flux density with four β parameters and five stress β-parameters is employed.

'Irreducible' elements with drilling DOFs:

- P4dM – A 4 node element with drilling DOFs, derived from functional Π_M in (3.29), and with stiffness matrix given by (3.68).

- P4dK – A 4 node element with drilling DOFs, derived from functional Π_K in (3.31), and with stiffness matrix given by (3.72).

'Degenerate' Hellinger-Reissner like elements:

- P4dMD – A 4 node assumed electric flux density element with drilling DOFs, derived from functional Π_M^D in (3.37), and with stiffness matrix given by (3.86).
- P4dKD – A 4 node assumed electric flux density element with drilling DOFs, derived from functional Π_K^D in (3.39), and with stiffness matrix given by (3.90).
- P4dMnT – A 4 node assumed stress element with drilling DOFs, derived from functional Π_M^T in (3.41), and with stiffness matrix given by (3.95), and number of stress parameters given by n.
- P4dKnT – A 4 node assumed stress element with drilling DOFs, derived from functional Π_K^T in (3.43), and with stiffness matrix given by (3.99), and number of stress parameters given by n.

Fully mixed Hellinger-Reissner like elements:

- P4dMnTD – A fully mixed 4 node element, based on functional Π_M^{TD} given in (3.33), with stiffness matrix given in (3.77). The number of stress interpolation parameters is given by n.
- P4dKnTD – A fully mixed 4 node element, based on functional Π_M^{TD} given in (3.35), with stiffness matrix given in (3.81). The number of stress interpolation parameters is given by n.

In the test problems to follow, unless otherwise stated, the material constants of PZT-4 given by Sze *et al.* [64] are employed so that our piezoelectric elements may be compared to theirs. To this end, the following material constants are used:

$$c_{11} = 139 \times 10^3, \quad c_{33} = 113 \times 10^3, \quad c_{13} = 74.3 \times 10^3, \quad c_{55} = 25.6 \times 10^3 \text{ (in N/mm}^2\text{)}$$
$$e_{15} = 13.44 \times 10^6, \quad e_{31} = -6.98 \times 10^6, \quad e_{33} = 13.84 \times 10^6 \text{ (in pC/mm}^2\text{)}$$
$$\epsilon_{11} = 6.00 \times 10^9, \quad \epsilon_{33} = 5.47 \times 10^9 \text{ (in pC/(GVmm))}.$$

The units of length, force, stress, charge, electric displacement and electric potential, respectively, are taken as mm, N, N/mm^2, pC, pC/mm^2 and GV. This unusual unit choice alleviates the ill effects resulting from the poor scaling of the global stiffness matrix. The poling direction in the test problems to follow, unless otherwise stated, is taken as the global y–direction. The constitutive equations which result are

$$\begin{Bmatrix} T_{xx} \\ T_{yy} \\ T_{xy} \\ D_x \\ D_y \end{Bmatrix} = \begin{bmatrix} c_{11} & c_{13} & 0 & 0 & -e_{31} \\ c_{13} & c_{33} & 0 & 0 & -e_{33} \\ 0 & 0 & c_{55} & -e_{15} & 0 \\ 0 & 0 & e_{15} & \epsilon_{11} & 0 \\ e_{31} & e_{33} & 0 & 0 & \epsilon_{33} \end{bmatrix} \begin{Bmatrix} S_{xx} \\ S_{yy} \\ S_{xy} \\ E_x \\ E_y \end{Bmatrix}. \tag{3.116}$$

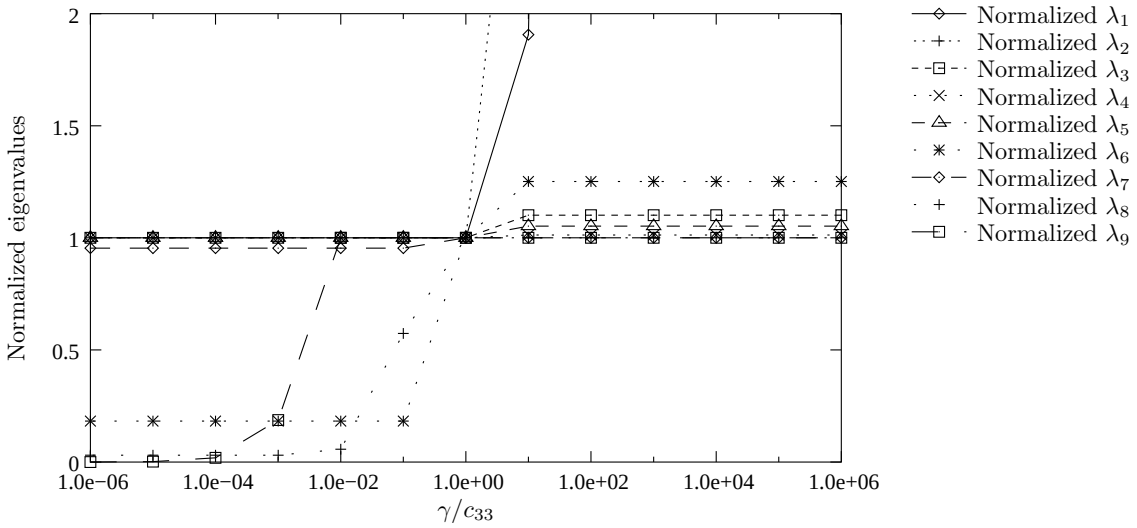

Figure 3.4: Effect of γ on eigenvalues (normalised with respect to their values at $\gamma/c_{33} = 1$).

Constants used in the analytical solutions of some of the tests to follow, are given by

$$\begin{bmatrix} s_{11} & s_{13} & g_{31} \\ s_{13} & s_{33} & g_{33} \\ -g_{31} & -g_{33} & \beta_{33} \end{bmatrix} = \begin{bmatrix} c_{11} & c_{13} & -e_{31} \\ c_{13} & c_{33} & -e_{33} \\ e_{31} & e_{33} & \epsilon_{33} \end{bmatrix}^{-1} . \tag{3.117}$$

3.8.1 Effect of γ

The elements developed in the foregoing are dependant on the problem-dependent penalty parameter γ. The effect of γ has been the focus of a number of recent studies, see Chapter 2 and [43, 58, 81] for examples. For linear elastic isotropic Dirichlet problems, the formulation is reported to be relatively insensitive to the value of γ [18, 21, 45], and it was proposed that $\gamma = \mu$, the shear modulus. Under different conditions, e.g. orthotropy (as in the case of piezoelectric materials) or dynamic problems, a greater sensitivity to γ is expected. For dynamic problems, for example, Hughes *et al.* [82] propose a value of $\gamma = \mu/10$.

To determine an appropriate value for γ, an eigenvalue analysis of an undistorted (square) P4dM element is performed. Although results are only reported for the P4dM element, the trends depicted in Figures 3.4 and 3.5 are typical for all of our new elements. Figure 3.4 depicts the effect of γ on the non-zero eigenvalues, arranged in descending order. The eigenvalues are normalised with respect to their values at $\gamma = c_{33}$. It is clear that the 'softer' modes are most sensitive to γ at values of $\gamma/c_{33} < 1$. For values of $\gamma/c_{33} > 1$, on the other hand, the 'harder' modes are significantly more sensitive, in particular λ_1 and λ_2, indicative of a locking-like phenomena. This results from the terms in the stiffness matrix containing γ dominating the response.

In order to determine the effect of γ on the accuracy of the current formulations, a representative test problem is studied for an array of γ values. The 10 element cantilever, depicted

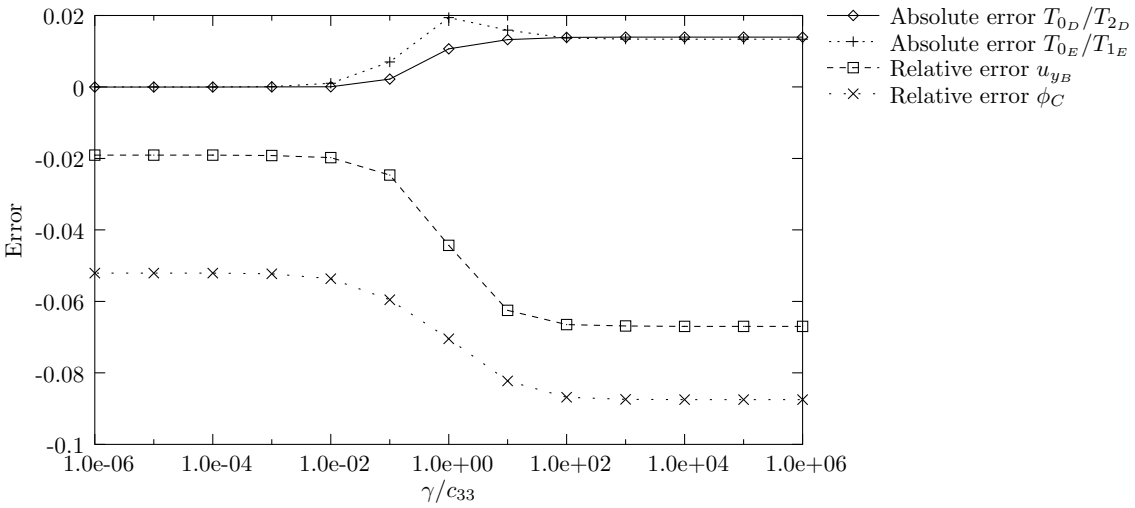

Figure 3.5: Effect of γ on skew part of stress and other accuracy measures.

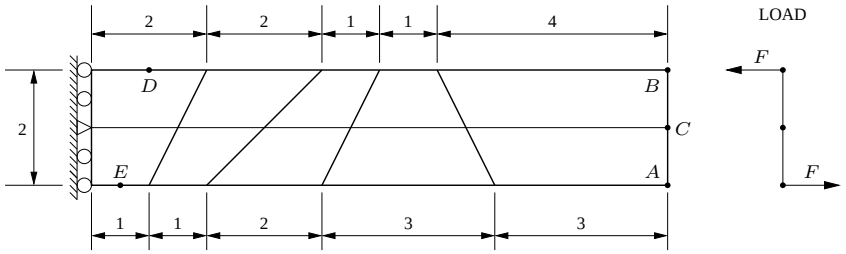

Figure 3.6: Ten element piezoelectric cantilever beam subjected to pure bending.

Figure 3.6, is selected for this study. In Figure 3.5 some accuracy measures are plotted as a function of γ/c_{33}.

Figure 3.5 shows how the accuracy of u_{yB}, the y–displacement at point B and of ϕ_C, the electric potential at C (see Figure 3.6), decrease at values of $\gamma/c_{33} > 1$. Also plotted is an indication of the error on the skew-symmetric part of stress, T_0 as suggested in Chapter 2 and [58]. The plotted values are normalised with respect to principle stresses at points D and E. T_{0D} and T_{0E} are the constant skew-symmetric part of stress in the elements containing points D and E, respectively. T_{2D} is the second (compressive) principle stress calculated at D and T_{1E} is the first principle stress at E. Since the skew-symmetric part of stress should be zero, both T_{0D}/T_{2D} and T_{0E}/T_{1E} should in turn be zero. Notably, the error on the skew-symmetric stress increases with larger values of γ/c_{33}. To avoid operating in the regime where the gradient change of the accuracy measures occurs, it is suggested that a value of $\gamma/c_{33} = 10^{-2}$ be used.

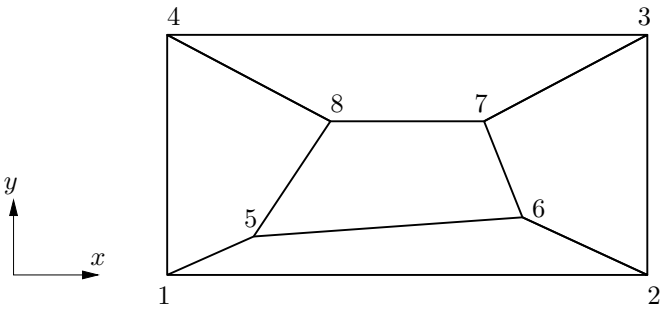

Coordinates:

Vertex	x	y
1	0.2	0.
2	0.44	0.
3	0.44	0.12
4	0.2	0.12
5	0.24	0.02
6	0.38	0.03
7	0.36	0.08
8	0.28	0.08

Figure 3.7: Mesh for piezoelectric patch test.

3.8.2 Eigenvalue analysis

Since a reduced order integration scheme is employed during stiffness calculations and a nonstandard γ value is used, element rank sufficiency needs to be verified by means of an eigenvalue analysis. The eigenvalues of 2×2, undistorted (square) elements are computed. (Eigenvalue analyses should in general be carried out on undistorted elements, since distortion may actually suppress zero energy modes due to the inaccuracies of an approximate integration scheme.)

In the case of planar piezoelectric elements, the mechanical partition of the stiffness matrix should contain only 3 zero eigenvalues corresponding to the 3 rigid body modes. An eigenvalue analysis of the dielectric part of the element stiffness matrix should reveal a single zero eigenvalue, corresponding to the constant potential distribution resulting in zero electric field. For the sake of brevity, the eigenvalues are not reported here. It was, however verified that each element possesses the proper number of non-zero eigenvalues.

3.8.3 Patch test

The patch test is a standard method to test for element convergence, as well as any possible implementation or programming errors. The test is performed with the geometry and mesh suggested by Sze *et al.* [64], as shown in Figure 3.7. Kinematic (displacement and potential) terms on the boundary are prescribed, corresponding to:

$$u_x = s_{11}\sigma_0 x, \qquad u_y = s_{13}\sigma_0 y, \qquad \phi = g_{31}\sigma_0 y, \tag{3.118}$$

with σ_0 a stress parameter. The corresponding stress and electric displacement can be shown to be constant, and are given by

$$T_{xx} = \sigma_0, \qquad T_{yy} = T_{xy} = D_x = D_y = 0. \tag{3.119}$$

Compliance with the conditions above was verified for each of the elements used in this study. A force patch test, with prescribed boundary forces corresponding to (3.119), was also conducted.

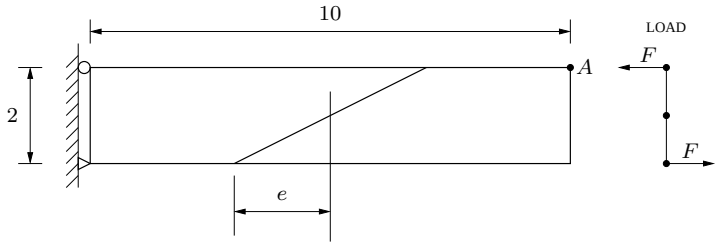

Figure 3.8: Two element piezoelectric cantilever beam subjected to pure bending.

3.8.4 Two element beam

The two element beam bending test is used to quantify the effect of distortion on element accuracy. Figure 3.8 depicts a cantilever beam of length L=10 and height h=2, modelled using two elements with a common distortion e. The electric potential of all nodes at $y = -1$ is prescribed to be zero. The exact solution for this problem was presented by Sze *et al.* [64]. The analytical solutions to this problem include:

$$u_x = -s_{11}\sigma_0 xy, \quad u_y = \frac{s_{13}\sigma_0}{2}\left(\frac{h^2}{4} - y^2\right) + \frac{s_{11}}{2}\sigma_0 x^2, \quad \phi = \frac{g_{31}\sigma_0}{2}\left(\frac{h^2}{4} - y^2\right), \quad T_x = -\sigma_0 y,$$

$$T_y = T_{xy} = D_x = D_y = 0, \qquad M = \int_{-h/2}^{h/2} yT_x \mathrm{d}y = -\frac{h^3\sigma_0}{12} = -hF.$$

Figure 3.9 depicts the relative error of the y–displacement at point A, i.e. $u_{y_A}/u_{y\text{Exact}} - 1$, for the various elements being tested. Considering the irreducible elements, the superior accuracy and stability of the P4dM and P4dK elements over the standard P4 elements is clear. The displacement accuracy of the assumed flux density elements are similar to that of the irreducible, and are actually slightly less accurate than the irreducible elements. Although the elements with 8 β-parameters perform slightly better than the elements with 9 β-parameters, the assumed stress elements surprisingly severely overestimate the tip displacements for the non-distorted mesh. The P4TD fully mixed elements without drilling degrees of freedom achieve an accuracy comparable to the elements developed by Sze *et al.* [64]. It is also demonstrated that the P4dM8TD and P4dK8TD elements are accurate and stable, even at extreme mesh distortions. In fact, for this problem these elements perform slightly better than the stabilised plane element developed by Sze *et al.* [64], as shown in Figure 3.9.

Figure 3.10 depicts the absolute error on the electric potential at point A, ϕ_A. In contrast to the displacement results, the elements without drilling DOFs all achieve a better accuracy on electric potential than the elements of the same family with drilling DOFs. However, considering the irreducible elements (which are the least numerically expensive and are the easiest to implement) the accuracy gained on the displacement is far more significant than that lost on electric potential. Unfortunately Sze *et al.* [64] did not report on this quantity, so comparison with their element was not possible. Having said than, the parabolic 'through-thickness' potential distribution of the exact solution can, of course, not be captured using

bilinear potential interpolations with the current mesh. The result is that for a regular mesh, zero electric field is predicted and therefore relatively large errors on displacement accrue due to the inherent coupling (as is apparent with the assumed stress elements).

This test is therefore repeated with a mesh consisting of two elements along the length (as before), but this time with two elements through the thickness (four elements in total). Although the effects of the mesh distortion are more pronounced for the aspect ratio of the elements in this test, this in our opinion, is a more reasonable mesh for this problem, since the physics of the problem can be approximated by all elements used in the comparison. That is to say, the parabolic potential distribution can be approximated using the bilinear potential interpolations of the aforementioned elements.

The displacement results are depicted in Figure 3.11. A significant improvement is achieved for the assumed stress degenerate elements, especially at zero distortion. All the elements with assumed stress (degenerate and full-mixed) perform similarly well. Once again the superior accuracy of our new irreducible elements with drilling DOFs over the standard P4 elements is noted. Our new elements also perform better than the existing P4D assumed flux density elements.

Figure 3.12 depicts the absolute error on ϕ_A for our four element beam problem. For this measure, a marked improvement is once again noted for the degenerate assumed stress elements with drilling DOFs. For this mesh, the standard P4T element only out-performs our new elements at extreme mesh distortions ($e > 2$). The electric potential of all fully mixed elements (with and without drilling DOFs) achieve similar accuracy. Although the irreducible and assumed flux density exhibit a slightly superior accuracy on electric potential when compared to the assumed stress and fully mixed elements, this slight accuracy improvement comes at the expense of a significant loss of accuracy on displacement accuracy.

3.8.5 Ten element beam

The same beam geometry as used in the two and four element test (with identical boundary conditions) is modelled, but this time with ten irregular elements as shown in Figure 3.6. Displacements and electric potentials are evaluated at points A, B and C and stresses and electric flux densities are calculated directly at points D and E. This problem was used by Wu *et al.* [65] to verify the accuracy of their P4TD element. Results are presented in Table 3.1.

Again, considering the irreducible elements used in this comparison, the the superior accuracy with respect most fields of the elements with drilling DOFs relative to P4 is evident. Our assumed flux density degenerate elements significantly out-perform the standard P4D elements on almost all measures. The performance of the assumed stress elements with and without drilling DOFs is similar, as is the performance of the fully mixed elements. In fact, the performance of the assumed stress family of elements is similar to the family of fully mixed elements with the notable exception of electric flux density accuracy. The inclusion of the independent interpolation for electric flux density therefore appears to significantly improve the accuracy of electrical quantities (potential and electric flux density).

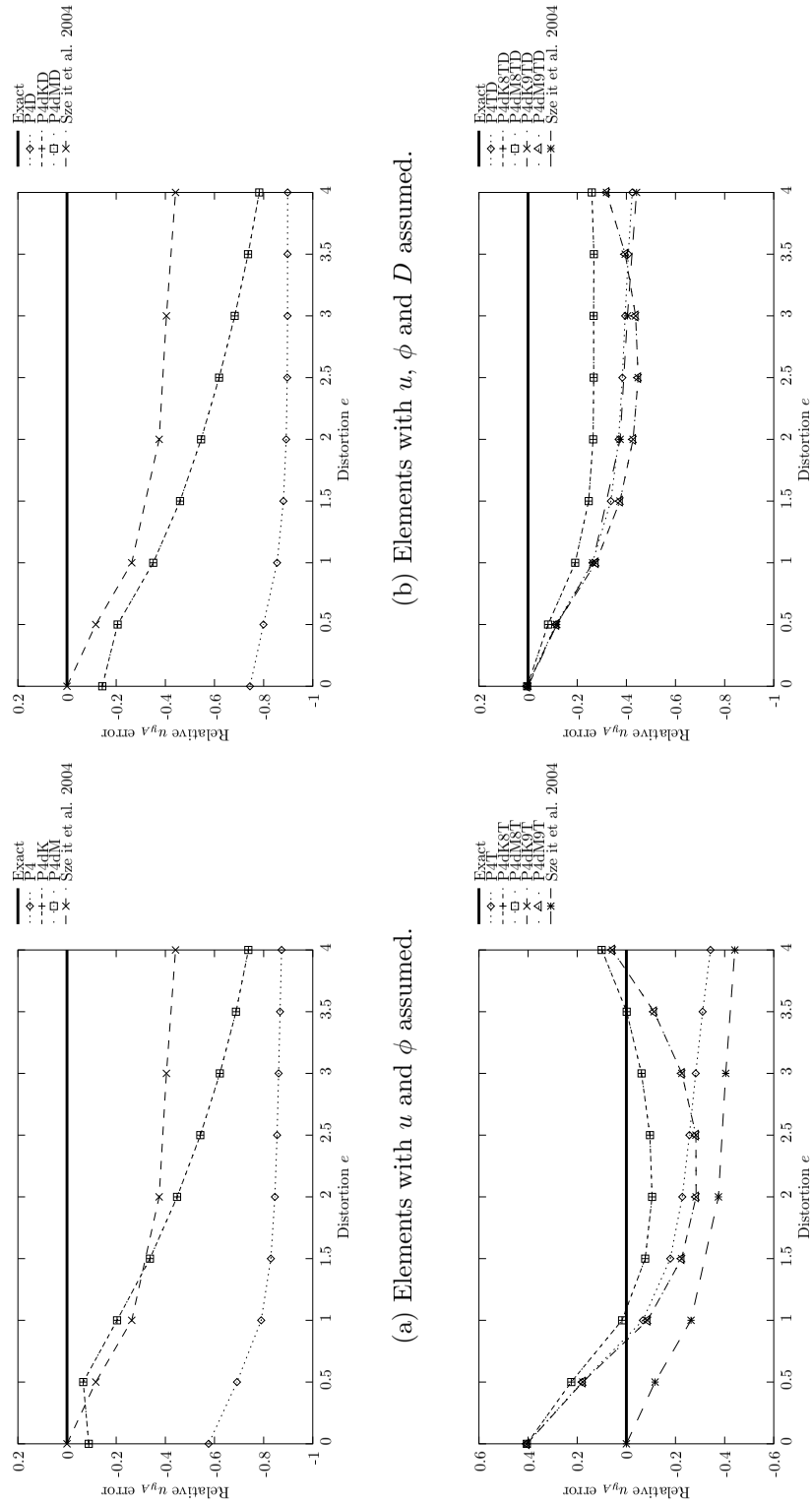

(a) Elements with u and ϕ assumed.

(b) Elements with u, ϕ and D assumed.

(c) Elements with u, ϕ and T assumed.

(d) Elements with u, ϕ, D and T assumed.

Figure 3.9: Two element piezoelectric beam subjected to pure bending: Effect of distortion on v_A.

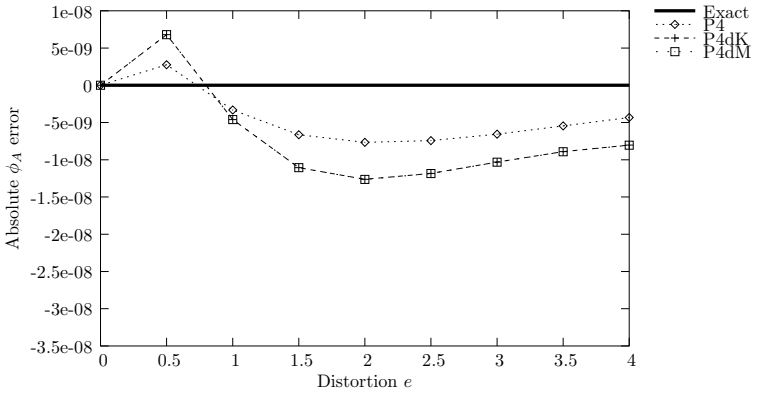

(a) Elements with u and ϕ assumed.

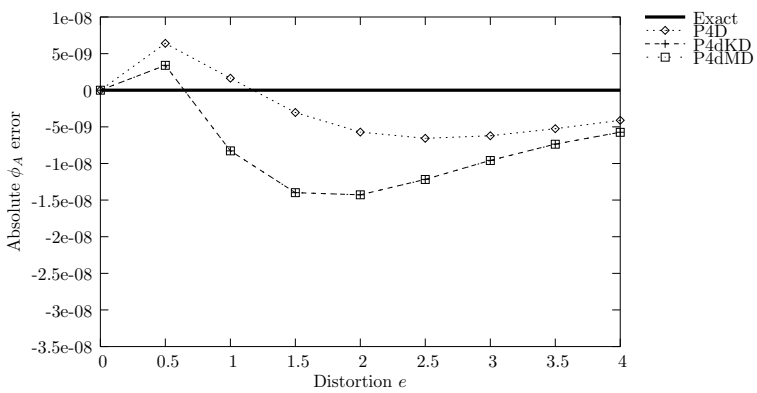

(b) Elements with u, ϕ and D assumed.

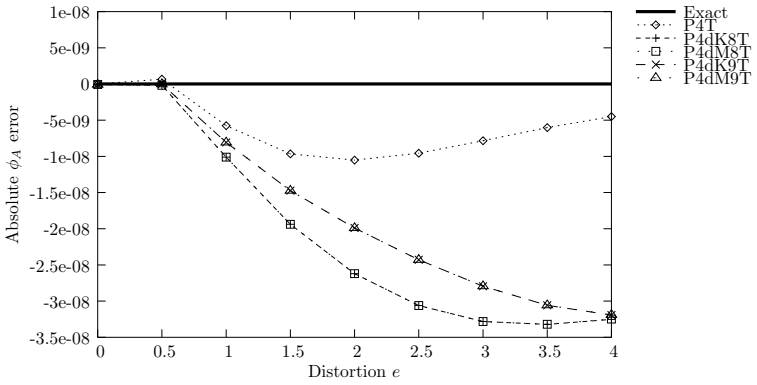

(c) Elements with u, ϕ and T assumed.

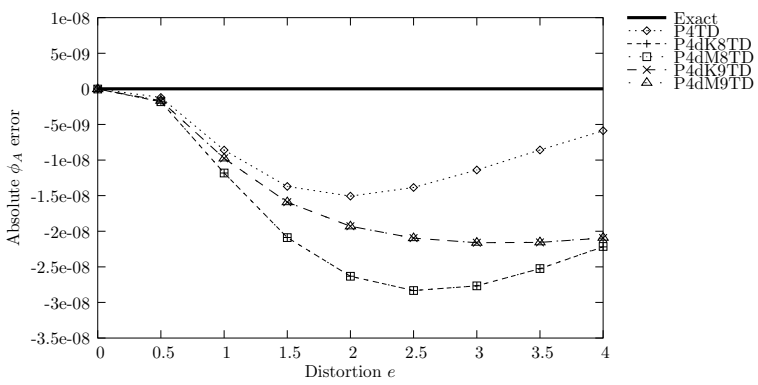

(d) Elements with u, ϕ, D and T assumed.

Figure 3.10: Two element piezoelectric beam subjected to pure bending: Effect of distortion on ϕ_A.

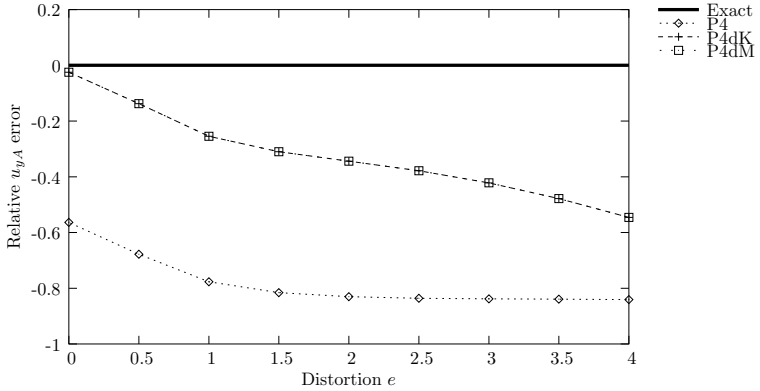

(a) Elements with u and ϕ assumed.

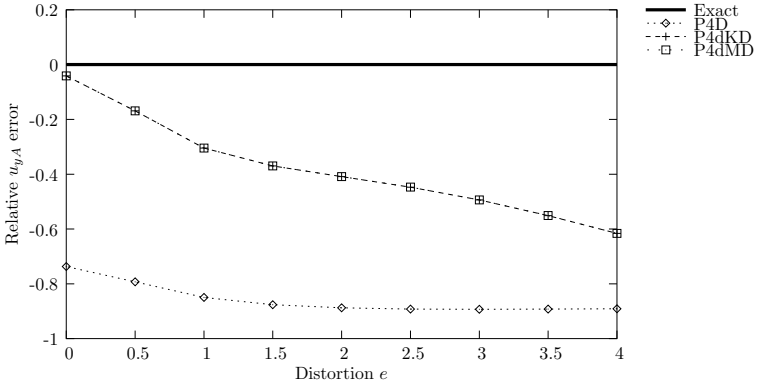

(b) Elements with u, ϕ and D assumed.

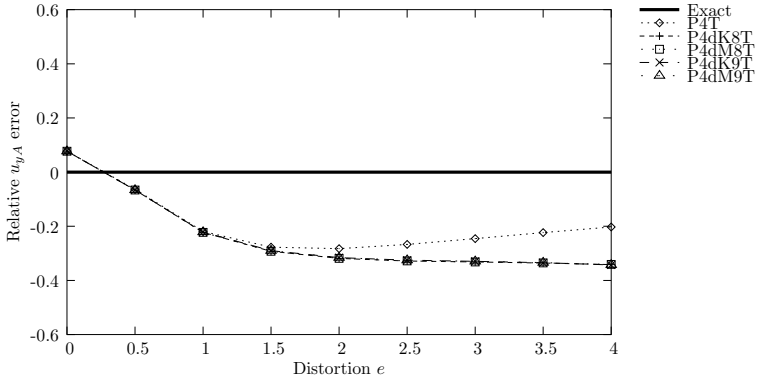

(c) Elements with u, ϕ and T assumed.

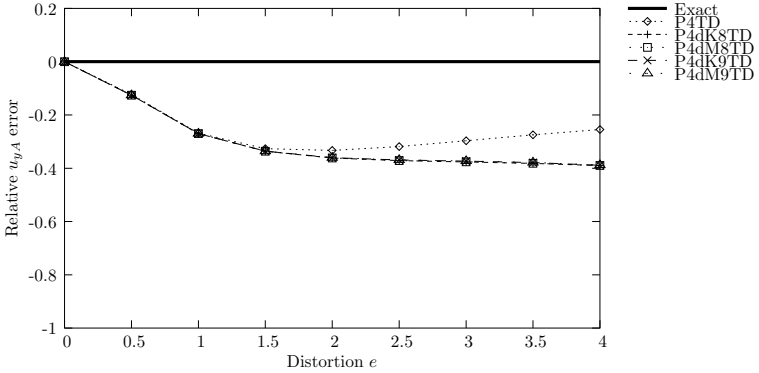

(d) Elements with u, ϕ, D and T assumed.

Figure 3.11: Four element piezoelectric beam subjected to pure bending: Effect of distortion on v_A.

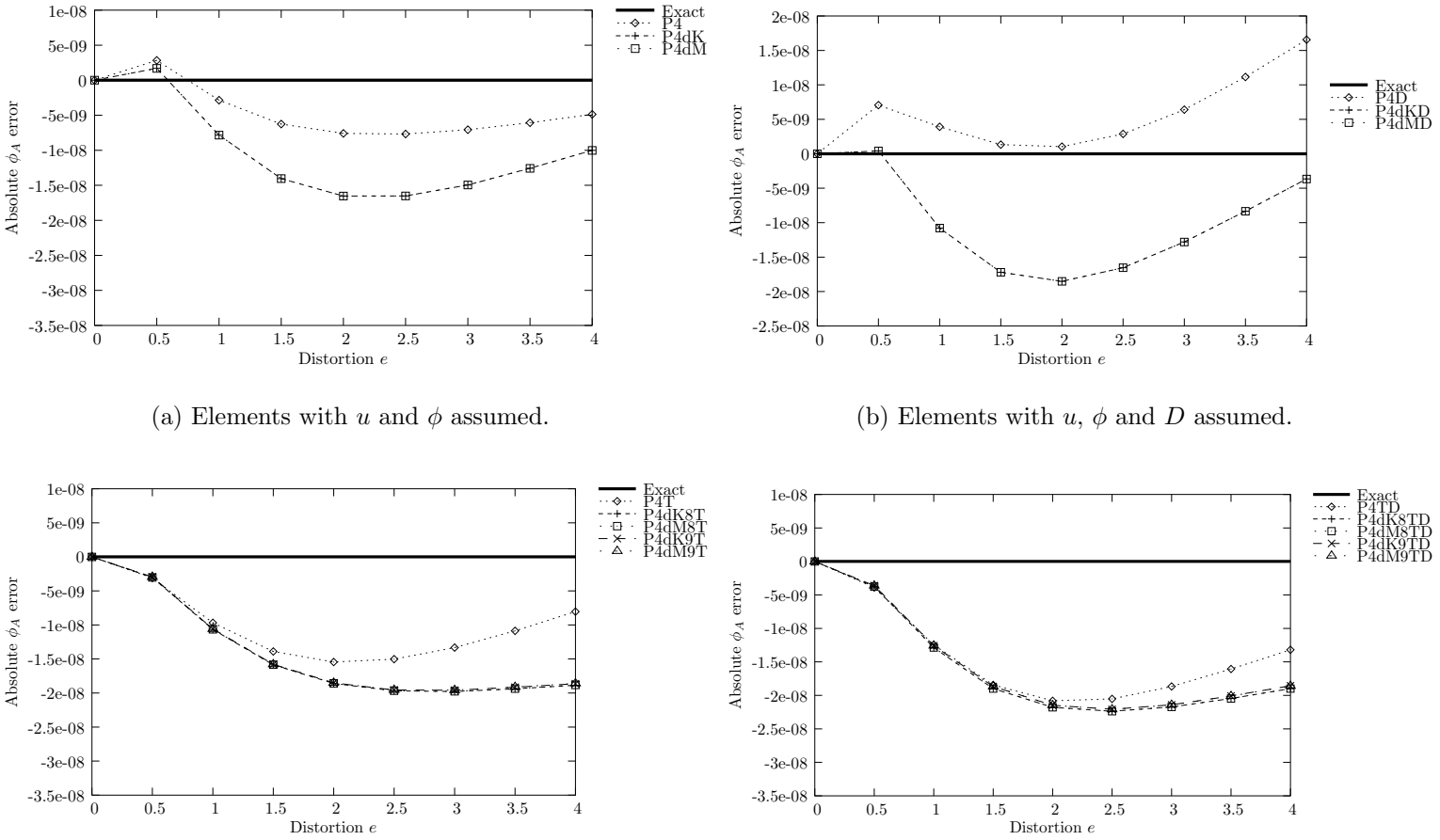

(a) Elements with u and ϕ assumed.

(b) Elements with u, ϕ and D assumed.

(c) Elements with u, ϕ and T assumed.

(d) Elements with u, ϕ, D and T assumed.

Figure 3.12: Four element piezoelectric beam subjected to pure bending: Effect of distortion on ϕ_A.

Table 3.1: Ten element piezoelectric cantilever subject to pure bending.

	Relative % error u_{xB}	Relative % error u_{yB}	Relative % error ϕ_C	Relative % error T_{xD}	Relative % error T_{xE}	Absolute error D_{yD}	Absolute error D_{yE}
P4	-40.4175	-36.1072	-48.1191	-21.3819	-5.2331	90.1438	-10.0964
P4dM	-3.4094	-1.3680	-5.3626	9.2982	18.1271	97.7308	-102.4166
P4dK	-3.4102	-1.3691	-5.3643	9.2977	18.1313	97.7287	-102.3594
P4D	-50.1581	-44.4320	-68.7544	-28.2890	-14.1054	32.5175	67.5230
P4dMD	-8.5244	-6.7333	-6.7703	7.5064	18.6191	-5.0939	7.6408
P4dKD	-8.5248	-6.7340	-6.7723	7.5049	18.6171	-5.0934	7.6520
P4T	1.0322	2.9902	7.5749	-7.1865	-6.9662	174.6776	-218.2058
P4dM8T	0.4151	2.2293	7.2564	-5.5496	-2.1303	183.0845	-231.3944
P4dK8T	0.4148	2.2295	7.2527	-5.5553	-2.1301	183.0898	-231.3809
P4dM9T	0.4814	2.2079	7.1959	-10.0337	-2.0298	130.5465	-225.8105
P4dK9T	0.4812	2.2082	7.1938	-10.0357	-2.0308	130.6023	-225.7964
P4TD	-5.7885	-4.0462	1.7121	0.7077	0.4331	-6.6586	7.4355
P4dM8TD	-6.4972	-4.8806	1.2997	1.9039	7.1635	-4.7693	8.3963
P4dK8TD	-6.4976	-4.8809	1.2964	1.8987	7.1609	-4.7642	8.4026
P4dM9TD	-6.4364	-4.8969	1.0597	-0.9267	7.1655	-4.3515	8.4282
P4dK9TD	-6.4368	-4.8971	1.0582	-0.9300	7.1626	-4.3471	8.4343

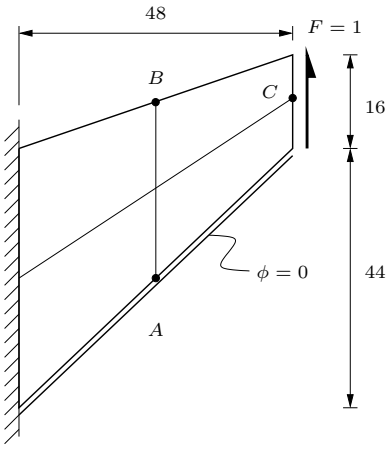

Figure 3.13: Piezoelectric Cook's membrane.

3.8.6 Cook's membrane

The final pathological test of element accuracy under mechanical actuation is depicted in Figure 3.13. The geometry and loading is similar to the popular Cook's membrane consisting of a swept and tapered beam with distributed tip load. The lower surface is prescribed to have a voltage of 0V. Since no analytical solution exists for this problem, the predicted solutions are compared to a finite element approximation with a sufficiently fine mesh. The best known values of u_{yC} and ϕ_C, computed by performing a detailed finite element analysis with a refined mesh, are 2.109×10^{-4}mm and 1.732×10^{-8}GV, respectively. Figure 3.14 depicts the magnitude of the relative error on u_{yC}, the y–displacement of point C, for different mesh refinements on a log scale. The accuracy of the irreducible and assumed flux density elements with drilling DOFs compared to their standard P4 and P4D counterparts is once again illustrated. In this case, the assumed stress elements achieve a far greater accuracy than the other elements, with the P4T element achieving the best displacement accuracy of all elements. All of the fully mixed elements with and without drilling DOFs perform similarly well.

Figure 3.15 depicts the magnitude of the relative error on ϕ_C, the electric potential at point C. The accuracy of electric potential within the four individual element families is similar, and a far less marked distinction between elements with and without drilling DOFs is apparent. Invariably upon comparing Figures 3.14 and 3.15, elements with superior displacement accuracy exhibit poorer potential accuracy and vice versa. Furthermore, the respective elements' loss of accuracy on electric potential appears to be less substantial than the accuracy gained on displacement accuracy.

Table 3.2 presents the relative percentage errors on the first principle stress at point A, T_{1A} and the magnitude of the electric flux density at B, $|D_B|$. The best known values for T_{1A} and $|D_B|$ are 0.21613 N/mm^2 and 22.409 pC/mm^2, respectively. In this case, the irreducible elements with drilling DOFs achieve the best approximations for both T_{1A} and $|D_B|$ with the exception of $|D_B|$ for the 2×2 discretisation. Again, the accuracy of the elements with drilling DOFs within the irreducible and assumed flux density families is illustrated.

Furthermore, as before the assumed stress and fully mixed families achieve similar accuracies regardless of whether drilling DOFs are included or not. Our new elements with 9 stress β-parameters appear to perform very well.

Table 3.2: Relative percentage error on stress and electric displacement for Cook's membrane.

	2×2 mesh		4×4 mesh		8×8 mesh	
	T_{1A}	$\lvert D_B \rvert$	T_{1A}	$\lvert D_B \rvert$	T_{1A}	$\lvert D_B \rvert$
P4	-44.6706	-80.3136	-19.8108	-68.3021	-3.7775	-33.9002
P4dM	-9.2049	-38.4155	-0.7867	-9.7136	-0.7298	-6.7096
P4dK	-9.1978	-38.4299	-0.7834	-9.7162	-0.7291	-6.7099
P4D	-50.8613	-77.1129	-20.2323	-86.1091	-3.8591	-38.5268
P4dMD	-19.7603	-42.8530	-3.7775	-19.5042	-1.2428	-8.9451
P4dKD	-19.7569	-42.8726	-3.7756	-19.5085	-1.2423	-8.9457
P4T	-21.4767	1.0435	-6.9101	-17.2497	-2.1175	-10.3702
P4dM8T	-28.7225	-4.0746	-8.2523	-24.1994	-2.3955	-12.9287
P4dK8T	-28.7176	-4.0162	-8.2527	-24.1880	-2.3958	-12.9280
P4dM9T	-19.8624	-1.8967	-6.2470	-25.8652	-1.8419	-11.9210
P4dK9T	-19.8634	-1.8251	-6.2477	-25.8541	-1.8422	-11.9204
P4TD	-20.9579	-45.4065	-6.0842	-23.5878	-1.6060	-10.6112
P4dM8TD	-35.3104	-48.9795	-7.3783	-25.3382	-2.1842	-11.6869
P4dK8TD	-35.3060	-48.9936	-7.3791	-25.3460	-2.1843	-11.6889
P4dM9TD	-18.2960	-47.2924	-4.7375	-25.4509	-1.3131	-11.6292
P4dK9TD	-18.2993	-47.3067	-4.7382	-25.4583	-1.3132	-11.6312

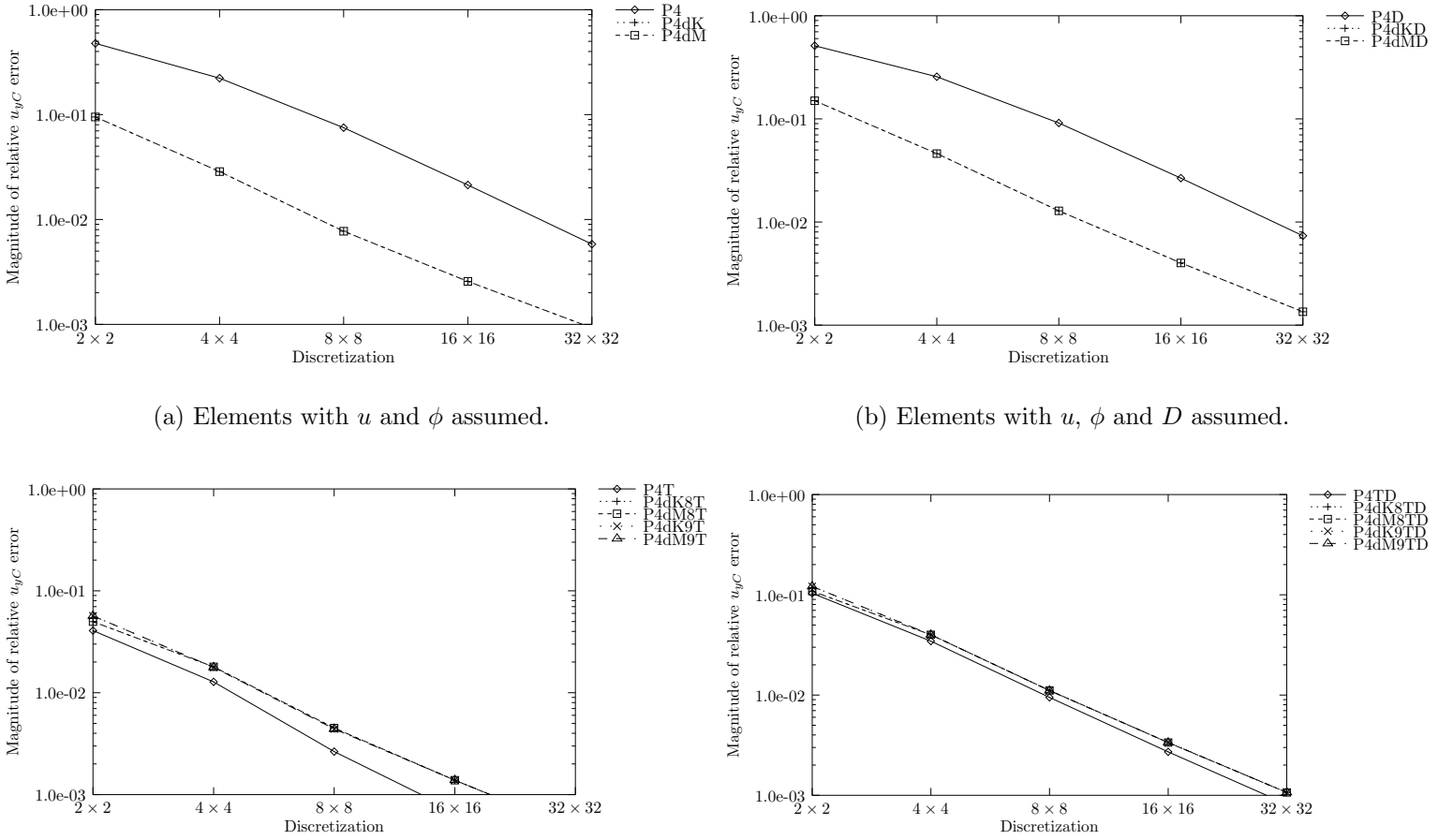

(a) Elements with u and ϕ assumed.

(b) Elements with u, ϕ and D assumed.

(c) Elements with u, ϕ and T assumed.

(d) Elements with u, ϕ, D and T assumed.

Figure 3.14: Cook's membrane: y–displacement at C (u_{yC}).

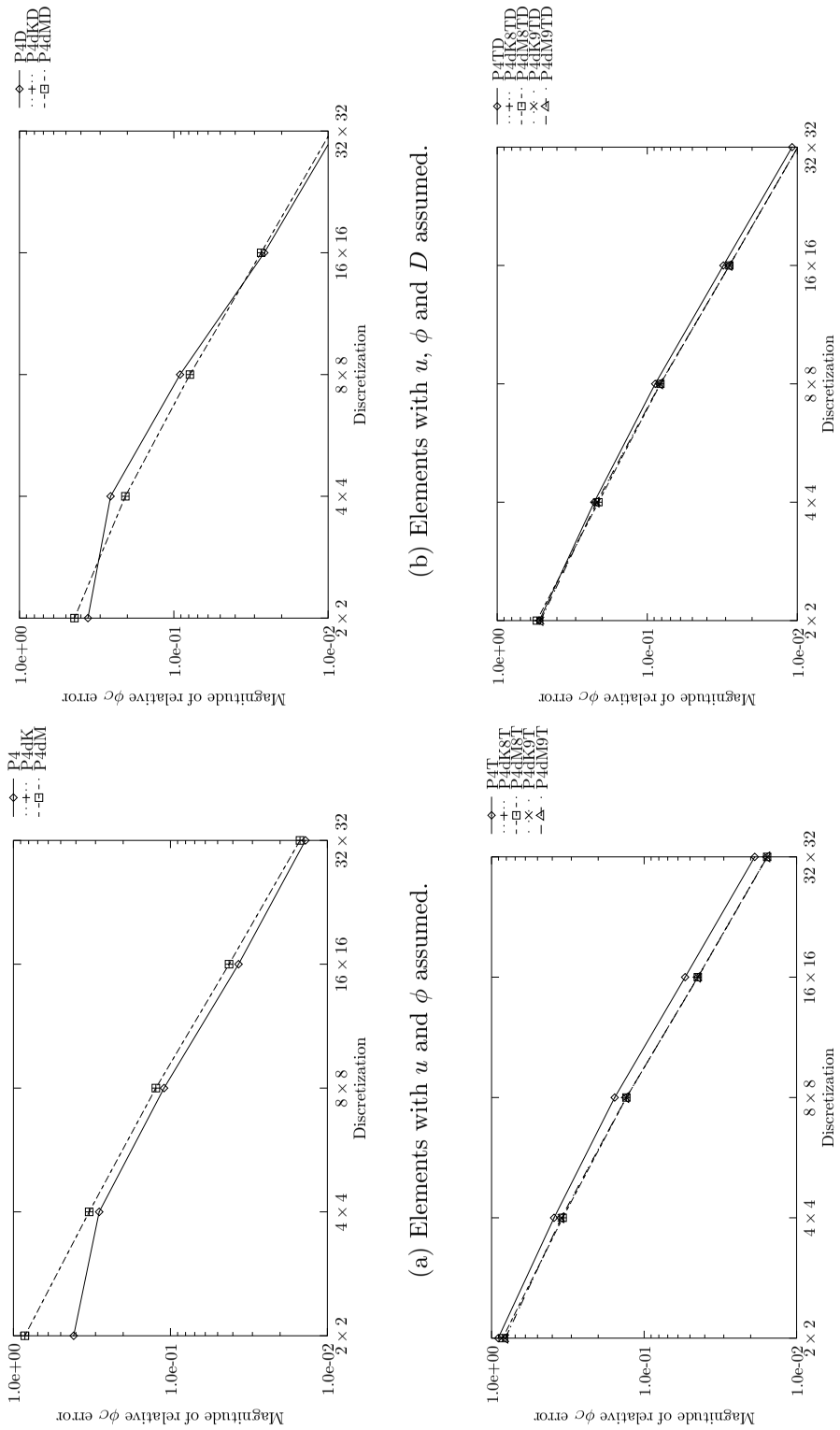

(a) Elements with u and ϕ assumed.

(b) Elements with u, ϕ and D assumed.

(c) Elements with u, ϕ and T assumed.

(d) Elements with u, ϕ, D and T assumed.

Figure 3.15: Cook's membrane: Electric potential at C (ϕ_{yC}).

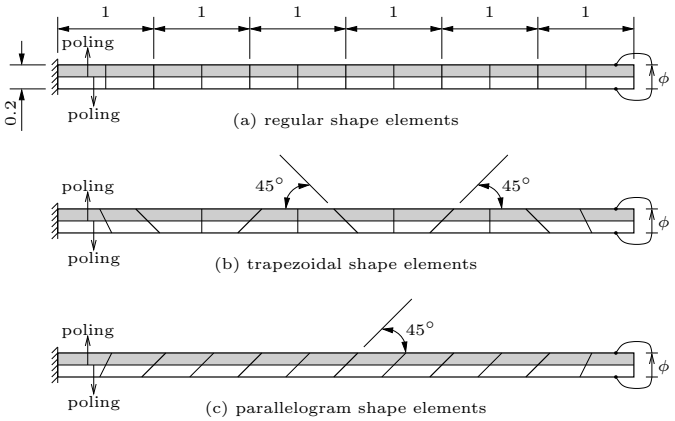

Figure 3.16: Bimorph based on MacNeal's elongated beam.

3.8.7 Piezoelectric bimorph beam

The final problem, evaluating element accuracy under electrical actuation, takes the form of a piezoelectric bimorph beam. The physical problem consists of two identical layers of piezoelectric material with opposite polarities, as indicated in Figure 3.16. Upon application of an electric field in the through-thickness direction, the bimorph bends as a result of moments caused by the layers' opposing polarities.

This problem is often solved using PVDF material constants and compared to the solution of Tzou [83]. For the purpose of the current study, tests are conducted using two different materials. To assess the element accuracy by beam solution, the Poisson's ratio is set to zero. Therefore the material properties for the PVDF material are [84] $E_1 = E_2 = E_3 = 2\times10^3$ (N/mm^2), $\nu_{12} = \nu_{13} = \nu_{23}=0$, $e_{31} = e_{32}=$-0.046$\times10^6$ (pC/mm^2) and $\epsilon_{11} = \epsilon_{33} = \epsilon_{33}=0.1062\times10^9$ (pC/GVmm). The e_{33} coefficient is assumed to be zero [84]. In the second case, the material properties of PZT-4, as used in the preceding problems, are used and the solution is compared to a refined finite element solution.

Since at least two elements are required through the thickness, the meshes used here represents a bisection of the discretisation suggested by MacNeal and Harder [85]. The top surface of the beam is subjected to 1V, and the bottom surface to -1V. The relative percentage error on the tip displacement is reported for the two different materials and the three meshes in Table 3.3. The beam solution for the PVDF material is 6.2100×10^{-5} mm, while the best known solution for the PZT-4 material is 4.3622×10^{-4} mm.

The over-stiff response of the P4 and P4D elements are once again highlighted for both regular and distorted elements. The significant improvement in performance upon addition of the drilling DOFs within these two element families is also once again apparent.

The results for both the assumed stress and fully mixed families employing the PVDF material are similar. Notably, elements with drilling DOFs and no assumed flux density interpolation predict the exact (beam) solution for the undistorted mesh. Meanwhile the same slight displacement error results for undistorted assumed flux density and fully mixed elements with drilling DOFs.

Table 3.3: Relative percentage error on vertical tip displacement of piezoelectric bimorph.

	PVDF			PZT-4		
	Regular	Trapezoidal	Parallel	Regular	Trapezoidal	Parallel
P4	-75.7576	-85.7547	-88.7211	-63.2273	-80.9720	-87.5199
P4dM	0	-35.4700	-10.4663	-6.3609	-27.7086	1.9377
P4dK	0	-35.4711	-10.4666	-6.3609	-27.7102	1.9372
P4D	-75.7722	-85.7599	-88.7247	-78.6452	-86.8639	-91.3582
P4dMD	-0.2484	-35.5802	-10.6666	-8.3357	-32.5815	-7.8569
P4dKD	-0.2484	-35.5813	-10.6669	-8.3357	-32.5825	-7.8572
P4T	0	-29.2346	-4.2227	7.0048	-19.7686	4.1441
P4dM8T	0	-33.8712	-5.0015	6.6919	-22.8712	3.8611
P4dK8T	0	-33.8721	-5.0020	6.6919	-22.8717	3.8604
P4dM9T	0	-33.8995	-5.0448	6.3358	-23.3704	3.5463
P4dK9T	0	-33.9004	-5.0453	6.3358	-23.3711	3.5457
P4TD	-0.2484	-29.3670	-4.4527	-2.6514	-26.4455	-5.2251
P4dM8TD	-0.2484	-33.9872	-5.2288	-2.9145	-29.0260	-5.5317
P4dK8TD	-0.2484	-33.9881	-5.2292	-2.9145	-29.0263	-5.5321
P4dM9TD	-0.2484	-34.0154	-5.2717	-3.2111	-29.4803	-5.8180
P4dK9TD	-0.2484	-34.0163	-5.2722	-3.2111	-29.4807	-5.8184

For this problem, the assumed stress elements perform slightly better than the fully mixed elements for the PZT-4 material and distorted meshes, with our assumed stress elements with drilling DOFs performing marginally better than the standard P4T element. The excellent performance of the irreducible elements for the PZT-4 bimorph is also noted.

3.9 Conclusions

A number of variational formulations accounting for piezoelectricity and in-plane rotations have been presented. Two new families of functionals, namely M-type, which retains the skew-symmetric part of the stress tensor, and K-Type, in which the skew part of stress is eliminated, are introduced.

From the M-Type Hu-Washizu-like functional an irreducible formulation with only 'kinematic' independent variables, i.e. displacement and electric potential, was developed. It has also been shown how a 'fully' mixed formulation, with stress and electric flux density assumed, can be generated. Two M-Type 'degenerate' Hellinger-Reissner-like functionals with either stress or electric flux density assumed, are also given. It was also demonstrated how the K-Type counterparts of our M-type functionals can be constructed.

Furthermore, numerical implementations of the M- and K-Type formulations are presented. The accuracy and robustness of our elements on a number of benchmark problems was demonstrated. The addition of drilling degrees of freedom enriches the interpolated displacement field, resulting in improved element performance. This is borne out by the improved accuracy and robustness of the P4dM and P4dK elements over the standard P4 piezoelectric element. The improved performance of our mixed elements with drilling degrees of freedom is generally less marked when compared to existing mixed piezoelectric elements. In fact, it is difficult to conclusively state that any one of the elements used in this study is better in terms of accuracy than all the others. This is so since none of the elements herein consistently outperforms all the other elements on all reported accuracy measures. Our 'fully mixed' elements, however, are shown to be accurate and stable, even at extreme element distortions. They also allow for improved modelling capabilities due to the additional rotational degree of freedom, e.g. compatibility with elastic elements with drilling degrees of freedom is ensured. The results presented herein, therefore indicate that the P4dMnTD and P4dKnTD elements are useful for modelling engineering applications.

What is more, the variational formulations constructed in this work can be used to establish three dimensional solid piezoelectric elements with drilling degrees of freedom. Furthermore, the planar elements derived here, when combined with piezoelectric plate elements, can be used to calculate through-thickness phenomena in thick piezoelectric shell elements.

Chapter 4

Modified reduced order quadratures for quadratic membrane elements

4.1 Summary

Reduced integration is frequently used in evaluating the element stiffness matrix of quadratically interpolated finite elements. Typical examples are the serendipity (Q8) and Lagrangian (Q9) membrane finite elements, for which a reduced 2×2 Gauss-Legendre integration rule is frequently used, as opposed to full 3×3 Gauss-Legendre integration. This 'softens' these element, thereby increasing accuracy, albeit at the introduction of spurious zero energy modes on the element level. This is in general not considered problematic for the "hourglass" mode common to Q8 and Q9 elements, since this spurious mode is non-communicable. The remaining two zero energy modes occurring in the Q9 element are indeed communicable. However, in topology optimization for instance, conditions may arise where the spurious mode associated with the Q8 element becomes activated. To effectively suppress these modes altogether in elements employing quadratic interpolation fields, two modified quadratures are employed herein. For the Q8 and Q9 membrane elements, the respective rules are a five and an eight point rule. As compared to fully integrated elements, the new rules enhance element accuracy due to the introduction of soft, higher-order deformation modes. A number of standard test problems reveal that element accuracy remains comparable to that of the under-integrated counterparts.

4.2 Introduction

In the earlier days of the development of the finite element method, numerical integration schemes attracted significant attention (e.g. see [54, 86, 87, 88]), possibly due to the limitations of the computing devices available at the time.

More recently, reduced integration schemes have frequently been used in combination with stabilization methods and explicit integration in the time domain, so as to increase computational efficiency when simulating computationally demanding models, e.g. nonlinear

crash analysis, metal forming, etc. The contributions of Belytschko and others (e.g. see [89, 90, 91, 92, 93]) are notable here. In essence they employ reduced integration schemes in conjunction with stabilization methods to prevent spurious modes that arise as a result of these schemes. On this subject the paper of Hughes *et al.* [94] is informative.

While the need for reduced integration is obvious in explicitly integrated, computationally demanding analyses, reduced integration is also frequently employed in implicitly integrated elastostatic or -dynamic analyses. This is normally done to alleviate locking in membrane, plate or shell elements, or merely to improve the behavior or these elements. Typical examples are the serendipity and Lagrangian membrane elements, which are over-stiff when full integration is used.

In the finite element method the equilibrium equations involve integration over the element volume. This is also true for the expressions for consistent nodal loads, mass matrices, penalty matrices, etc. For simple elements the integrand may be formed explicitly, resulting in *exact* integration. However, numerical integration schemes are necessary when element geometries are distorted, of which the Gaussian rules are possibly the best known and most frequently employed. The effects of numerical integration schemes are summarized in a clear manner by Cook *et al.* [17]:

For numerically integrated elements, full integration indicates a quadrature rule sufficient to provide the exact integrals of all terms in the element stiffness matrix $\boldsymbol{K}^e$ if the element geometry is undistorted. The same 'full integration' rule will not exactly integrate $\boldsymbol{K}^e$ if the element is distorted, or if the center nodes are offset from the element midpoints, since the Jacobian $\boldsymbol{J}$ is no longer constant throughout the element domain.

In this work, reduced order integration refers an integration scheme of lower order (fewer points and lower order of accuracy) than the lowest order rule which results in the exact integration of elemental matrices for an undistorted element.

A lower-order quadrature rule, called reduced integration, may be desirable for two reasons. Firstly, since the expense of generating the matrix $\boldsymbol{K}^e$ by numerical integration is proportional to the number of sampling points, fewer points results in lower computational cost. Secondly, a low order rule tends to soften an element, thus countering the overly-stiff behavior associated with assumed displacement fields. (The displacement based finite element method is monotonically convergent from below.) Softening comes about because certain higher-order polynomial terms happen to vanish at Gauss points of a low-order rule. Simply stated, with fewer sampling points, some of the more complicated displacement modes offer less resistance to deformation.

We pertinently differentiate between (a) the accuracy of an integration scheme, and (b) the numerical accuracy of finite elements. The former indicates the error of an approximate integration scheme as compared to the exact integral, while the latter indicates the performance of finite elements employing these approximate numerical schemes. It is reiterated that the numerical accuracy or performance of finite elements frequently increases when the accuracy of the integration scheme itself decreases. This is due to the fact that some limiting behavior (e.g. locking) is rendered negligible, or almost so, when reduced as opposed to full integration is employed. While accuracy of integration of $\boldsymbol{K}^e$ decreases with reduced integration, the element accuracy may actually increase.

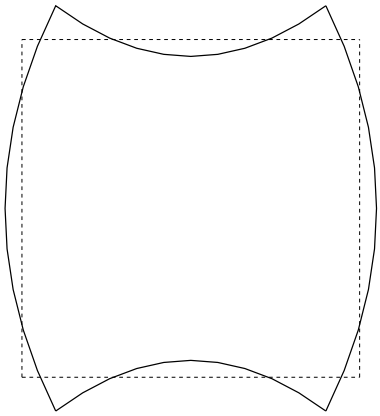

Figure 4.1: Typical spurious mode of Q8 employing a 4 point Gauss-Legendre scheme.

In summary, reduced integration may be able to simultaneously reduce cost, reduce accuracy in the evaluation of integration expressions, and increase the accuracy of the finite element analysis. Barring extremely expensive analyses, it is however noted that most authors agree that reduced integration should in general not be used if reduced cost is the sole motivation.

Numerical testing of any proposed rule is mandatory. Even though solution accuracy may be mesh dependent and problem dependent, one quadrature rule is usually superior to others. For bilinear (Q4) and eight-node plane elements (Q8), and for eight node linear solid elements, an order 2 Gauss rule is favored over an order 3 rule (four and eight points for plane and solid elements, respectively).

For Q4, the order 2 Gauss rule is problem free (at least as far as spurious modes are concerned). For Q8, the order 2 Gauss rule introduces a spurious mode on the element level. For Q9 (the Lagrangian 'bubble' counterpart of Q8), the order 2 Gauss rule introduces 3 spurious modes on the element level. The "hourglass" spurious mode common to the Q8 and Q9 elements, depicted in Figure 4.1, is in general not considered problematic since it is non-communicable, viz. the spurious mode is unable to propagate in a mesh consisting of more than one element. However, in some practical situations, conditions may arise where this spurious mode becomes activated. One example is the SIMP (Solid Isotropic Material with Penalization) material description, frequently used in topology optimization (e.g. see [4]), where the elasticity tensor in adjacent elements may vary considerably. The remaining two zero energy modes associated with the Q9 element are, however, communicable.

For illustrative purposes the general expression for the stiffness matrix $\boldsymbol{K}^e$ of a single three-dimensional finite element is considered, and can be written as (e.g. see [60])

$$\boldsymbol{K}^e = \int_\Omega \boldsymbol{B}^T \boldsymbol{C} \boldsymbol{B} \, d\Omega, \tag{4.1}$$

where $\boldsymbol{B}$ is the strain-displacement operator, $\boldsymbol{C}$ the matrix that defines the constitutive relationship, and Ω the element volume. Also, $d\Omega = dx\, dy\, dz$ in the Cartesian coordinate system, which is transformed to the natural coordinate system as $d\Omega = dr\, ds\, dt\, |\boldsymbol{J}|$, with $|\boldsymbol{J}|$ the determinant of the Jacobian matrix $\boldsymbol{J}$ of the transformation. In the natural coordinate

system,

$$\boldsymbol{K}^e = \int_{-1}^{1}\int_{-1}^{1}\int_{-1}^{1} \boldsymbol{B}^T\boldsymbol{C}\boldsymbol{B}\,|\boldsymbol{J}|\;dr\,ds\,dt. \tag{4.2}$$

During numerical integration, (4.2) is written as

$$\boldsymbol{K}^e = \sum_{n=1}^{N} W_n \boldsymbol{B}^T(r_n,s_n,t_n)\,\boldsymbol{C}\,\boldsymbol{B}(r_n,s_n,t_n)\,|\boldsymbol{J}(r_n,s_n,t_n)|, \tag{4.3}$$

where (r_n, s_n, t_n) is the n^{th} position of the integration point, associated with weight W_n, of any suitable integration scheme using N integration points. In (4.3) it is assumed that the constitutive relation defined by $\boldsymbol{C}$ is not a function of the global coordinates (x, y, z). It is desirable that (4.3) is problem free in terms of locking, (element) accuracy and spurious modes.

For 2-D planar elements the through-thickness component is usually constant, (4.3) therefore reduces to

$$\boldsymbol{K}^e = h\sum_{n=1}^{N} W_n \boldsymbol{B}^T(r_n,s_n)\,\boldsymbol{C}\,\boldsymbol{B}(r_n,s_n)\,|\boldsymbol{J}(r_n,s_n)|, \tag{4.4}$$

where h represents the constant element thickness and where the Jacobian, $\boldsymbol{J}$, is of reduced size compared to (4.3).

In this study it is attempted to effectively suppress spurious modes in quadratic finite elements altogether, using two modified quadratures proposed by Dovey [54].

This chapter is laid out as follows: Firstly, a summary of the formulation presented by Dovey is presented since his work on reduced order integration is probably not widely known. Numerical experiments are then performed for several well known test problems using the modified quadrature rules, as well as the standard order 2 and order 3 Gauss-Legendre rules. Finally, conclusions are drawn, based on the results of our numerical experiments.

For the sake of brevity, we restrict ourselves to the 2-D problem. However, the development for quadratically interpolated 3-D brick elements is similar. In 2-D, the standard order 2 and order 3 Gauss-Legendre rules will be referred to as the 4 and 9 point Gauss-Legendre rules.

4.3 Derivation of numerical integration schemes

In this section the work of Dovey [54] is closely followed. The same notation is used. Consider the area integral given by

$$I = \int_{-1}^{1}\int_{-1}^{1} F(r,s)\;\;dr\,ds, \tag{4.5}$$

where $F(r, s)$ is any polynomial function of r and s. Any polynomial expression of two variables can be expressed in the form

$$F(r,s) = \sum_{i,j} A_{ij} r^i s^j. \tag{4.6}$$

No limits are placed on the summation indices i and j as any arbitrary polynomial is being considered.

Let any N-point rule be written as

$$I^* = \sum_{n=1}^{N} W_n F(r_n, s_n), \tag{4.7}$$

where I^* represents the numerical approximation to I. Integration point n is given by (r_n, s_n) and the associated weight is given as W_n.

Each term of (4.6) may be trivially integrated as follows:

$$\int_{-1}^{1}\int_{-1}^{1} A_{ij} r^i s^j \, drds = \begin{cases} \frac{2^2 A_{ij}}{(i+1)(j+1)} & i, j \text{ both even,} \\ 0 & \text{otherwise.} \end{cases} \tag{4.8}$$

Application of the quadrature rule of (4.7) to the function $F(r, s)$ in the form of (4.6) gives the following result, which is expressed in terms of the coefficients A_{ij} as

$$I^* = A_{00}\sum_{n=1}^{N}(W_n) + A_{10}\sum_{n=1}^{N}(W_n r_n) + A_{01}\sum_{n=1}^{N}(W_n s_n) + A_{20}\sum_{n=1}^{N}\left(W_n r_n^2\right) + \cdots \tag{4.9}$$

Two points are to be noted:

- Symmetry of the rule in each coordinate implies that the coefficients corresponding to all odd powers will vanish in (4.9). This of course corresponds to the vanishing of the integral of odd powers over this region.
- Symmetry with respect to both coordinates is required to ensure invariance of the rule.

Equating the coefficients of A_{ij} between (4.8) and (4.9) gives a series of equations in the weights W_n and the coordinates r_n and s_n. Evidently the number of equations that are satisfied for a particular set of weights and coordinates indicate which polynomial terms are integrated exactly by that particular rule. Also, the degree to which each remaining equation is not satisfied gives the error in that polynomial term. Each equation has the form

$$\sum_{n=1}^{N} W_n r_n^i s_n^j = \frac{2^2}{(i+1)(j+1)}, \tag{4.10}$$

for the coefficient A_{ij}. Clearly all equations containing odd values for either i or j are satisfied identically for symmetric rules.

The maximum number of equations needed from (4.10) is determined by the order of the function $F(r, s)$ which is to be integrated. If the maximum number of equations possible is satisfied for a particular configuration, then an optimal scheme for that configuration is obtained. However, if less than the maximum number are satisfied, a less accurate rule is obtained, but freedom is available for arbitrary selection of some values of weights or coordinates. The foregoing was used by Dovey to derive a symmetrical 5 and 8 point rule, as is briefly presented in the following.

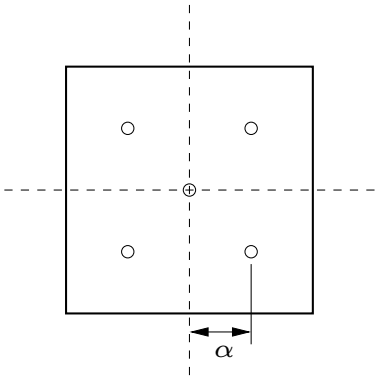

Figure 4.2: 5 Point integration scheme.

4.3.1 A five point rule

The 5-point rule is depicted in Figure 4.2. Due to symmetry, the weights W_α are identical. The rule is indicated by

$$I^* \;=\; W_0 F(0,0) + W_\alpha F(\pm\alpha, \pm\alpha). \tag{4.11}$$

The second term of (4.11) indicates four points when all combinations of positive and negative signs are taken.

Employing (4.10) the first four equations are obtained for the appropriate terms A_{ij} as

$$\begin{array}{lcl} A_{00} & : & W_0 + 4W_\alpha = 4, \\ A_{20}, A_{02} & : & 4W_\alpha\alpha^2 = 4/3, \\ A_{22} & : & 4W_\alpha\alpha^4 = 4/9, \\ A_{40}, A_{04} & : & 4W_\alpha\alpha^4 = 4/5. \end{array} \tag{4.12}$$

The last two of these equations are directly inconsistent and so the last is discarded. Also, however, the first three are inconsistent if the center point is retained.

Solving the first three expressions of (4.12) leads to

$$\alpha \;=\; 1/\sqrt{3};\;\; W_\alpha \;=\; 1 \;\text{ and }\; W_0 \;=\; 0, \tag{4.13}$$

which is the 2×2 Gaussian product rule. The leading error term is defined by the last of equations (4.12) and gives the error $(I^* - I)$, corresponding to the fourth power terms, r^4 and s^4, as

$$E_{40} \;=\; (4W_\alpha\alpha^4 - 4/5)A_{40},\;\; E_{04} \;=\; (4W_\alpha\alpha^4 - 4/5)A_{04}. \tag{4.14}$$

However, the center point may be retained by selecting a value for W_0, computing W_α and α from the first two relationships in (4.12). This implies an error in the A_{22} term. The scheme is now defined by

$$W_\alpha \;=\; 1 - W_0/4, \tag{4.15}$$

$$\alpha \;=\; \left(\frac{1}{3W_\alpha}\right)^{\frac{1}{2}}. \tag{4.16}$$

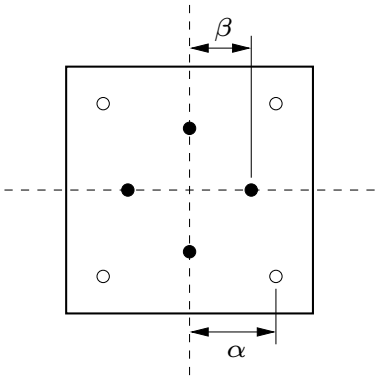

Figure 4.3: 8 Point integration scheme.

The scheme only has physical meaning while $0 \leq W_0 < 4$. The error in the A_{22} term is minimized as $W_0 \rightarrow 0$. In practice this implies that the 5-point scheme converges to the 2×2 Gaussian scheme as $W_0 \rightarrow 0$. This rule was previously used by Groenwold and Stander for their 4-node thick shell finite element with 6 d.o.f. per node [52].

It is noted that as $W_0 \rightarrow 4$, $W_\alpha \rightarrow 0$ and from (4.16), $\alpha \rightarrow \infty$. Even though, for a polynomial being integrated between -1 and 1, function evaluations outside of this region may be permitted, it is preferable that for applications in the finite element method this situation be avoided. The value of α is therefore limited to the defined region $0 \leq \alpha \leq 1$. This implies from (4.15) and (4.16) that W_0 be chosen such that $0 \leq W_0 \leq \frac{8}{3}$.

4.3.2 An eight point rule

The 8-point rule is depicted in Figure 4.3. This rule was previously employed for membrane elements with in-plane rotational degrees of freedom by Stander and Wilson [95] in the QC9(8) element, and also by Ibrahimbegovic *et al.* [21] in their drilling degree of freedom membrane element. The rule is described by

$$I^* = W_\alpha F(\pm\alpha, \pm\alpha) + W_\beta \left[F(\pm\beta, 0) + F(0, \pm\beta)\right]. \tag{4.17}$$

Due to symmetry, the weights W_α are identical, as are the weights W_β. The governing equations are given by

$$\begin{array}{lcl} A_{00} & : & 4W_\alpha + 4W_\beta = 4, \\ A_{20}, A_{02} & : & 4W_\alpha\alpha^2 + 2W_\beta\beta^2 = 4/3, \\ A_{22} & : & 4W_\alpha\alpha^4 = 4/9, \\ A_{40}, A_{04} & : & 4W_\alpha\alpha^4 + 2W_\beta\beta^4 = 4/5. \end{array} \tag{4.18}$$

All four equations may be satisfied and the solution is

$$\alpha = \sqrt{7/9}; \quad W_\alpha = 9/49; \quad \beta = \sqrt{7/15}; \quad W_\beta = 40/49. \tag{4.19}$$

This rule gives comparable accuracy to the 3×3 Gaussian rule. However unlike the 3×3 Gauss rule, this 8-point rule possesses leading error terms are given by:

$$E_{42} = (4W_\alpha\alpha^6 - 4/15)A_{42},\ E_{24} = (4W_\alpha\alpha^6 - 4/15)A_{24},\ \text{and} \tag{4.20}$$

$$E_{44} = (4W_\alpha\alpha^8 - 4/25)A_{44}. \tag{4.21}$$

A scheme of lower accuracy, neglecting the last term of (4.18), is defined by

$$W_\alpha = 1 - W_\beta, \tag{4.22}$$

$$\alpha = (\frac{1}{9W_\alpha})^{\frac{1}{4}}, \tag{4.23}$$

$$\beta = \left(\frac{2/3 - 2W_\alpha\alpha^2}{W_\beta}\right)^{\frac{1}{2}}. \tag{4.24}$$

In this case both α and β are restricted to be between 0 and 1. This implies that W_β be chosen such that $0 < W_\beta < \frac{8}{9}$.

4.4 Numerical evaluation

For the purpose of determining accuracy, approximate area integration schemes should be evaluated numerically [54]. Without numerical evaluation the effect of reduced integration on for instance locking, higher order deformation modes, etc., cannot be determined.

Moreover, such evaluations should include an investigation into element eigenvalues to determine element rank. In general, it is of the utmost importance to prevent any spurious modes or rank deficiencies [96], which could lead to unstable mechanisms on the structural level. Even if no mechanisms appear in an assembled structure, element rank deficiency should always be accepted cautiously. The basis for this reasoning is that no extent of numerical testing can fully characterize an element with inherent mechanisms, and no guarantee for well-defined behavior under all conditions can be given. (Again, computationally demanding models may be considered an exception. However, one does of course *not* expect elements with quadratic interpolations in these models.)

The derived modified quadratures, as well as the standard 4 and 9 point quadrature rules, are now applied to various test problems in order to obtain estimates for appropriate values of the weights W_0 and W_β.

4.4.1 Eigenvalue analysis

The results of an eigenvalue analysis of a single (square) Q8 element are tabulated in Table 4.1. (Eigenvalue analyses should in general be done for regular, undistorted elements, since distortion may actually suppress zero energy modes due to the inaccuracies of an approximate integration scheme.) In Table 4.1, the 9 point scheme represents full and exact integration. As is well known, the 4 point scheme introduces a superfluous zero energy mode or mechanism ($\lambda_{13} \approx 0$). The mode associated with λ_{13} is depicted in Figure 4.1. With the 5 and 8 point

λ_i	4 pt. scheme –	5 pt. scheme $W_0 = 0.01$	5 pt. scheme $W_0 = 0.1(8/3)$	8 pt. scheme $W_\beta = 0.01$	8 pt. scheme $W_\beta = 0.1(8/9)$	9 pt. scheme –
1	4.82388e+00	4.82388e+00	4.82388e+00	4.82388e+00	4.82388e+00	4.82388e+00
2	4.82388e+00	4.82388e+00	4.82388e+00	4.82388e+00	4.82388e+00	4.82388e+00
3	2.31873e+00	2.32416e+00	2.47404e+00	2.31933e+00	2.32434e+00	2.41527e+00
4	2.00000e+00	2.00251e+00	2.07309e+00	2.00126e+00	2.01168e+00	2.21240e+00
5	1.37447e+00	1.37447e+00	1.37447e+00	1.37447e+00	1.37447e+00	1.37447e+00
6	1.37447e+00	1.37447e+00	1.37447e+00	1.37447e+00	1.37447e+00	1.37447e+00
7	1.00000e+00	1.00251e+00	1.07143e+00	1.00063e+00	1.00582e+00	1.10000e+00
8	7.50000e-01	7.50209e-01	7.56048e-01	7.50629e-01	7.55908e-01	8.79436e-01
9	5.00000e-01	5.01251e-01	5.34055e-01	5.00628e-01	5.05772e-01	5.87596e-01
10	4.31271e-01	4.31475e-01	4.36678e-01	4.31294e-01	4.31482e-01	4.34735e-01
11	3.01646e-01	3.01646e-01	3.01646e-01	3.01646e-01	3.01646e-01	3.01646e-01
12	3.01646e-01	3.01646e-01	3.01646e-01	3.01646e-01	3.01646e-01	3.01646e-01
13	$<$ 1.0e-15	4.17595e-04	1.18095e-02	1.25524e-03	1.15433e-02	1.70564e-01
14	$<$ 1.0e-15	$<$ 1.0e-15	$<$ 1.0e-15	$<$ 1.0e-15	$<$ 1.0e-15	$<$ 1.0e-15
15	$<$ 1.0e-15	$<$ 1.0e-15	$<$ 1.0e-15	$<$ 1.0e-15	$<$ 1.0e-15	$<$ 1.0e-15
16	$<$ 1.0e-15	$<$ 1.0e-15	$<$ 1.0e-15	$<$ 1.0e-15	$<$ 1.0e-15	$<$ 1.0e-15

Table 4.1: Eigenvalues of a square Q8 serendipity element for different integration schemes (plane stress, $|\boldsymbol{J}| = 1$, $E = 1$, $\nu = 1/3$).

schemes, the mechanism is replaced by a 'soft' higher order deformation mode, as borne out by the low value for λ_{13}. Hence a low strain energy is associated with this particular mode.

Figure 4.4 depicts the effect of the weights W_0 and W_β on the value of λ_{13}, for respectively the 5 and 8 point schemes. If the soft higher order mode is desired, a low value of weight should be used, typically in the region of 10% of the maximum weight for both W_0 and W_β, viz. $W_0 = 0.1(8/3)$ and $W_\beta = 0.1(8/9)$. Furthermore, if W_β is chosen in the region of $40/49$ for the 8 point scheme, similar values to the 9 point scheme are obtained.

For the Q9 element, a similar analysis is carried out with results tabulated in Table 4.2. As is well known, e.g. see [17], reduced integration of this element with an order 2 Gauss rule induces 3 zero energy modes ($\lambda_{13,14,15} \approx 0$). For this element the 5 point scheme only eliminates one of the spurious modes, and the resulting element remains rank deficient by 2.

Figure 4.5 depicts the effect of integration rule weight on λ_{15} for both the 5 and 8 point schemes. For the 5 point scheme, W_0 has no effect on λ_{15} as illustrated in Figure 4.5, or on λ_{14} (not shown). For λ_{13}, however, the weight of the 5 point rule has an effect similar to that experienced by the Q8 element.

4.4.2 Effect of element aspect ratio

For both Q8 and Q9, the effect of element aspect ratio on the λ_{13} is now studied. For this test, a single rectangular element of unit height, with variable length, and constant material

λ_i	4 pt. scheme –	5 pt. scheme $W_0 = 0.1(8/3)$	8 pt. scheme $W_\beta = 0.01$	8 pt. scheme $W_\beta = 0.1(8/9)$	8 pt. scheme $W_\beta = 40/49$	9 pt. scheme –
1	4.82388e+00	4.81443e+00	4.82783e+00	4.86165e+00	6.25205e+00	5.58912e+00
2	4.82388e+00	4.81443e+00	4.82783e+00	4.86165e+00	6.25205e+00	5.58912e+00
3	2.31873e+00	2.32416e+00	2.31933e+00	2.32434e+00	2.41527e+00	2.41527e+00
4	2.00000e+00	2.00251e+00	2.00126e+00	2.01168e+00	2.21240e+00	2.21240e+00
5	1.37447e+00	1.37396e+00	1.37522e+00	1.38171e+00	1.75566e+00	1.56065e+00
6	1.37447e+00	1.37396e+00	1.37522e+00	1.38171e+00	1.75566e+00	1.56065e+00
7	1.00000e+00	1.00251e+00	1.00063e+00	1.00582e+00	1.10000e+00	1.10000e+00
8	7.50000e-01	7.50209e-01	7.50629e-01	7.55908e-01	8.84191e-01	8.79436e-01
9	5.00000e-01	5.01251e-01	5.00628e-01	5.05772e-01	8.84191e-01	6.80792e-01
10	4.31271e-01	4.31475e-01	4.31294e-01	4.31482e-01	8.79436e-01	6.80792e-01
11	3.01646e-01	3.01593e-01	3.02001e-01	3.05498e-01	5.87596e-01	5.87596e-01
12	3.01646e-01	3.01593e-01	3.02001e-01	3.05498e-01	4.34735e-01	4.34735e-01
13	$<$ 1.0e-15	4.17595e-04	5.02504e-03	4.64348e-02	2.74764e-01	2.69437e-01
14	$<$ 1.0e-15	$<$ 1.0e-15	5.02504e-03	4.64348e-02	2.74764e-01	2.69437e-01
15	$<$ 1.0e-15	$<$ 1.0e-15	1.25524e-03	1.15433e-02	1.70564e-01	1.70564e-01
16	$<$ 1.0e-15	$<$ 1.0e-15	$<$ 1.0e-15	$<$ 1.0e-15	$<$ 1.0e-15	$<$ 1.0e-15
17	$<$ 1.0e-15	$<$ 1.0e-15	$<$ 1.0e-15	$<$ 1.0e-15	$<$ 1.0e-15	$<$ 1.0e-15
18	$<$ 1.0e-15	$<$ 1.0e-15	$<$ 1.0e-15	$<$ 1.0e-15	$<$ 1.0e-15	$<$ 1.0e-15

Table 4.2: Eigenvalues of a square Q9 Lagrange element for different integration schemes (plane stress, $|\boldsymbol{J}| = 1$, $E = 1$, $\nu = 1/3$).

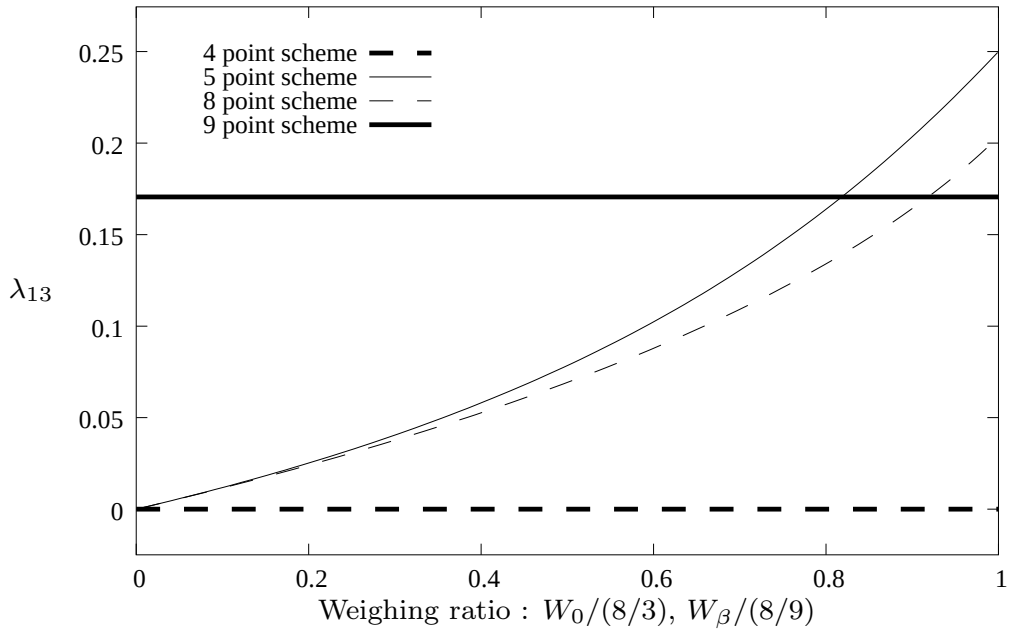

Figure 4.4: λ_{13} of Q8 with different integration schemes (plane stress, $|\boldsymbol{J}| = 1$, $E = 1$, $\nu = 1/3$).

properties $E = 1$ and $\nu = 1/3$ is used. Results are depicted in Figures 4.6 and 4.7 for Q8 and Q9 respectively.

For Q8, λ_{13} obtained with all of the 5 and 8 point rules converge to the eigenvalue obtained using full 3×3 Gauss-Legendre integration. (While this value decreases as the aspect ratio increases, it never reaches zero.) For Q9, similar results are obtained, although the results reiterate that Q9 is to be integrated using the 8 point scheme. For this element, the results for λ_{14} and λ_{15} are similar (not shown).

The foregoing illustrates that, for both Q8 and Q9, the modified integration schemes do not induce mechanisms as element aspect ratio is increased.

4.4.3 Cantilever beam in pure bending

Figure 4.8 depicts a cantilever beam modeled using two elements with a common distortion d. The vertical displacements v_A and v_B, and horizontal displacement u_B are reported for the Q8 and Q9 elements, using different integration schemes. The results are tabulated in Table 4.3. Since the Q9 element stiffness matrix becomes singular when 4 and 5 point schemes are used, these results are not reported. For $d = 0$, both elements predict the exact solutions for displacements. In addition, the Q9 element is completely insensitive to distortion using both the 8 and 9 point schemes and predicts the exact solution in all cases. Even for the extreme case of $d = 5$, the exact solution is recovered.

For the Q8 element, Figure 4.9 depicts the effect of distortion on the vertical displacement v_B for the various integration schemes. With the 4 and 5 point schemes (the latter with

d	Element	Scheme	Weight	v_A	u_B	v_B
1.0	Q8	4	–	7.50000	1.50000	7.51000
		5	0.01	7.50000	1.50000	7.51002
			0.1(8/3)	7.50000	1.50000	7.51045
		8	0.01	7.49961	1.49992	7.50958
			0.1(8/9)	7.49648	1.49929	7.50621
			40/49	7.41490	1.48277	7.42211
		9	–	7.44849	1.48962	7.45721
	Q9	8	0.01	7.50000	1.50000	7.52250
			0.1(8/9)	7.50000	1.50000	7.52250
			40/49	7.50000	1.50000	7.52250
		9	–	7.50000	1.50000	7.52250
2.0	Q8	4	–	7.50000	1.50000	7.47250
		5	0.01	7.50000	1.50000	7.47256
			0.1(8/3)	7.50000	1.50000	7.47429
		8	0.01	7.49187	1.49849	7.46381
			0.1(8/9)	7.43244	1.48708	7.40160
			40/49	6.27595	1.25407	6.23790
		9	–	6.66839	1.33307	6.63637
	Q9	8	0.01	7.50000	1.50000	7.52250
			0.1(8/9)	7.50000	1.50000	7.52250
			40/49	7.50000	1.50000	7.52250
		9	–	7.50000	1.50000	7.52250
Exact				7.50000	1.50000	7.52250

Table 4.3: Displacement results for distorted cantilever beam.

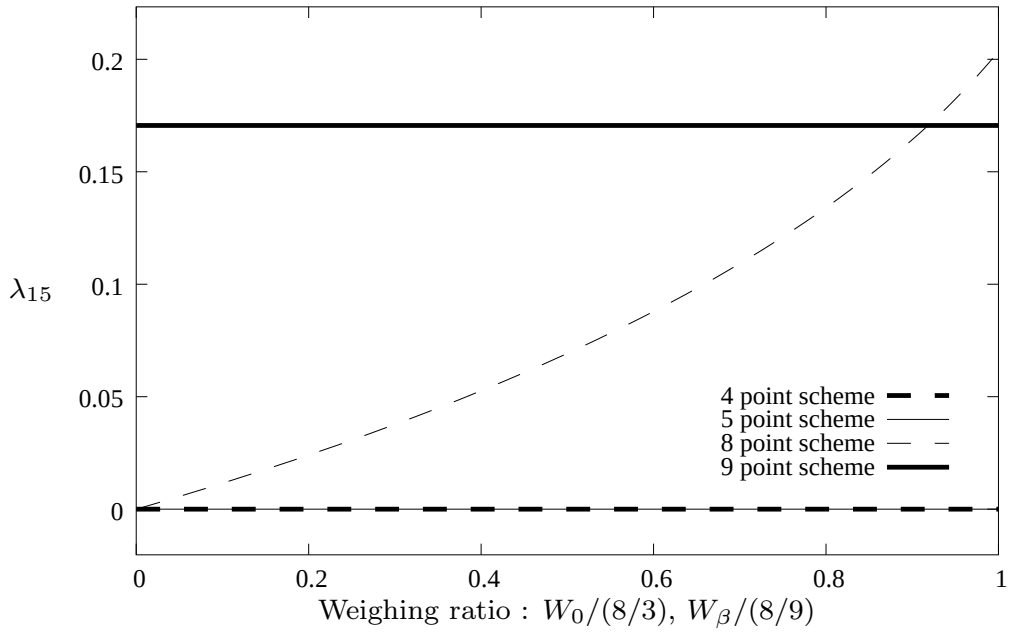

Figure 4.5: λ_{15} of Q9 element for different integration schemes (plane stress, $|\boldsymbol{J}| = 1$, $E = 1$, $\nu = 1/3$).

low value of W_0), this element is notably less sensitive to the severity of the distortion as compared to the 8 and 9 point schemes. Again, $W_0 = 0.1(8/3)$ and $W_\beta = 0.1(8/9)$ seem suitable.

4.4.4 A near mechanism

Again, Cook *at al.* [17] are cited: A structure that appears to be adequately constrained may have an instability that makes the assembled structural stiffness matrix $\boldsymbol{K}$ singular, or near-singular. Or, unstable elements may combine to form a structure that is stable, but unduly susceptible to certain load patterns, so that computed displacements are excessive. Again, this situation may occur in topology optimization problems.

The situation is depicted in Figure 4.10. A 2×2 Gauss rule is used to integrate $\boldsymbol{K}^e$ in each element. The stiff element, shown shaded, is weakly restrained by soft elements connected to the fixed boundary allowing a singular mode to become pronounced.

Figure 4.11 depicts the incremental displacement $\hat{v}$ at point A, as illustrated in Figure 4.10. The 5 and 8 point schemes yield comparable results (their respective curves are not distinguishable on the scale of the figure. Again, suitable weights are roughly 10% of the maximum permissible weights (viz. $0.1(8/3)$ for the 5 point rule and $0.1(8/9)$ for the 8 point rule).

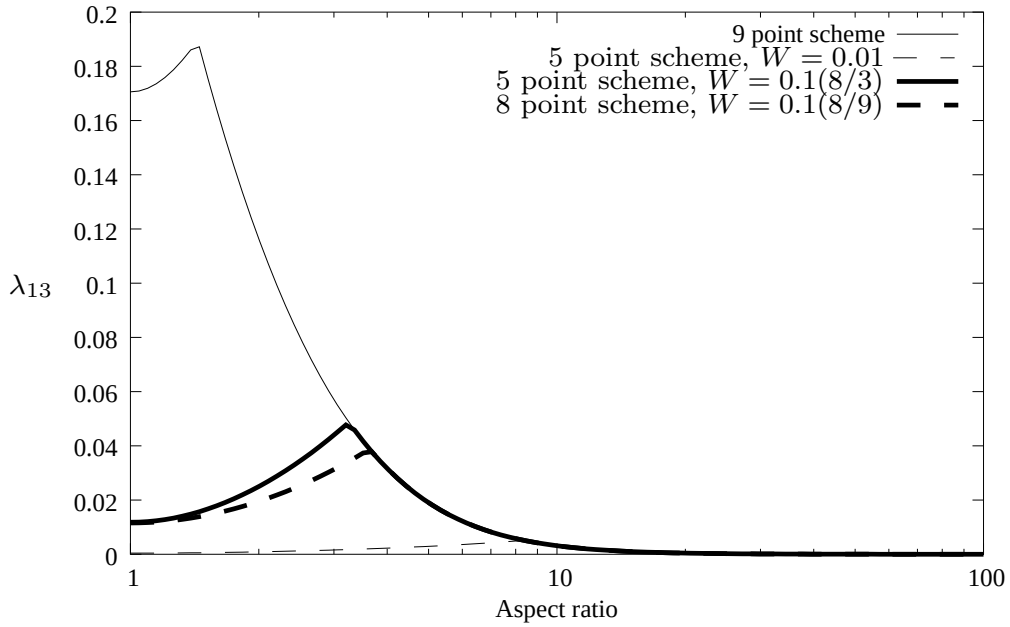

Figure 4.6: Effect of aspect ratio on λ_{13} of Q8 for different integration schemes.

4.4.5 Highly constrained square plate

In this test, a highly constrained mesh is used to demonstrate that spurious modes are not confined to meshes with few constraints, as illustrated by Bićanić and Hinton [97]. A square 6×6 mesh is completely constrained on the boundary, and an eigenvalue analysis is carried out on the global stiffness matrix. In Figures 4.12, 4.13 and 4.14 the lowest six eigenvectors are depicted together with the corresponding eigenvalue, for the 4, 8 ($W_\beta = 0.1(8/9)$) and 9 point schemes, respectively.

Modes 5 and 6 of the 4 point scheme in Figure 4.12 are spurious and are due to instabilities caused by the reduced integration scheme. (These modes are also known as Escher modes.) In Figure 4.13, it is shown that these spurious modes are not present when a 9 point integration scheme is used. What is more, it is shown that if the 8 point scheme is used with $W_\beta = 0.1(8/9)$, the spurious modes are eliminated, as demonstrated in Figure 4.14.

4.4.6 Cook's membrane

This popular test problem has been used by many authors and is depicted in Figure 4.15. The center displacement v_C for the various integration schemes is tabulated in Table 4.4, while stresses $(\sigma_{\min})_B$ and $(\sigma_{\max})_A$ are presented in Table 4.5.

The displacement results reveal the over-stiff behavior of the Q8 element with a 9 point rule and an 8 point scheme with $W_\beta = 40/49$. All other integration schemes predict displacement values close to the best known solution. Although the four point scheme is the most accurate, this high accuracy of course comes at the expense of a mechanism. Figure 4.16 depicts the effect of different values of weight on the center displacement v_C for a single Q8 element.

Element	Scheme	Weight	1×1	2×2	4×4
Q8	4	-	20.00	23.17	23.73
	5	0.01	19.98	23.17	23.73
		$0.1(\frac{8}{3})$	19.52	23.09	23.72
	8	0.01	19.95	23.17	23.73
		$0.1(\frac{8}{9})$	19.58	23.14	23.73
		40/49	17.16	22.71	23.71
	9	-	17.22	22.72	23.71
Q9	4	-	26.97	24.15	24.00
	5	0.01	26.97	24.15	24.00
		$0.1(\frac{8}{3})$	26.75	24.11	23.99
	8	0.01	26.74	24.10	23.97
		$0.1(\frac{8}{9})$	25.25	23.91	23.94
		40/49	19.09	23.20	23.82
	9	-	19.64	23.29	23.84
Best known				23.95	

Table 4.4: Cook's membrane: Center displacement v_C.

			1×1		2×2		4×4	
Element	Scheme	Weight	$(\sigma_{max})_A$	$(\sigma_{min})_B$	$(\sigma_{max})_A$	$(\sigma_{min})_B$	$(\sigma_{max})_A$	$(\sigma_{min})_B$
Q8	4	-	0.12530	-0.26746	0.26210	-0.23356	0.24439	-0.20198
	5	0.01	0.12536	-0.26700	0.26198	-0.23354	0.24438	-0.20196
		$0.1(\frac{8}{3})$	0.12678	-0.25577	0.25881	-0.23313	0.24408	-0.20156
	8	0.01	0.12553	-0.26589	0.26197	-0.23351	0.24439	-0.20196
		$0.1(\frac{8}{9})$	0.12726	-0.25437	0.26090	-0.23312	0.24425	-0.20182
		40/49	0.13451	-0.18594	0.24722	-0.22750	0.24212	-0.20075
	9	-	0.13446	-0.18623	0.24727	-0.22741	0.24212	-0.20075
Q9	4	-	0.18776	-0.15703	0.27176	-0.33457	0.24523	-0.33042
	5	0.01	0.18745	-0.15732	0.27178	-0.33436	0.24532	-0.33029
		$0.1(\frac{8}{3})$	0.17950	-0.16401	0.27184	-0.32621	0.24675	-0.32073
	8	0.01	0.18476	-0.15786	0.26984	-0.30335	0.24484	-0.26768
		$0.1(\frac{8}{9})$	0.16806	-0.16181	0.26437	-0.22257	0.24657	-0.21771
		40/49	0.13613	-0.16055	0.25023	-0.21037	0.24374	-0.20539
	9	-	0.13736	-0.15334	0.25015	-0.20845	0.24362	-0.20633
Best known			0.2360	-0.2010	0.2360	-0.2010	0.2360	-0.2010

Table 4.5: Cook's membrane: Stress analysis.

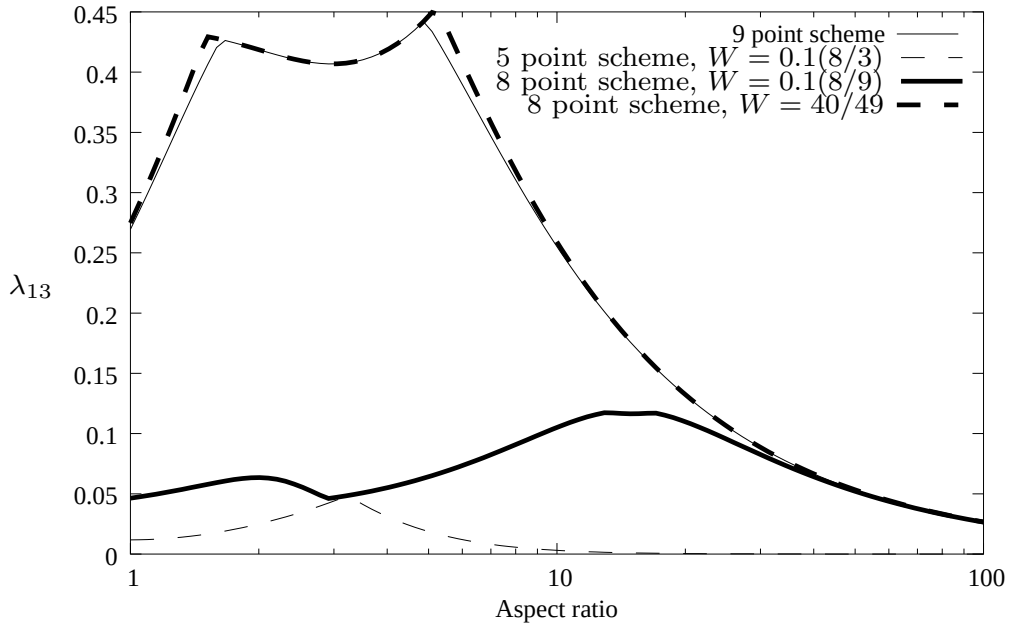

Figure 4.7: Effect of aspect ratio on λ_{13} of Q9 for different integration schemes.

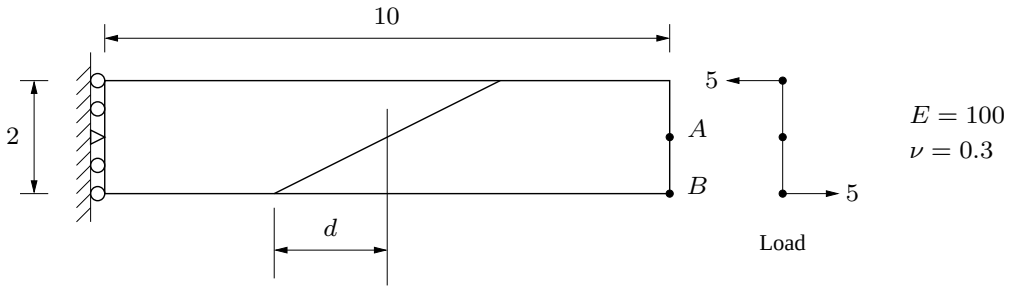

Figure 4.8: Distorted cantilever beam.

In contrast to the Q8 element, for the Q9 element the lower order integration schemes overestimate the displacement, while the 9 and 8 point schemes with $W_\beta = 40/49$ still lock. The best scheme for the Q9 element is the 8 point scheme with $W_\beta = 0.1(8/9)$. Figure 4.17 depicts the effect of different values of weight on the center displacement u_C for a Q9 element. As expected, locking of the Q9 element is to a great extent alleviated by low values of W_β.

The stress results generally reveal the same trend. It should be noted that for the 1×1 mesh, a single value of stress is calculated at points A and B, whereas in the case of the 2×2 and 4×4 meshes, the average of the stresses over the two relevant elements is calculated and reported. This explains the non-monotonic convergence behavior between the three mesh densities (although monotonic convergence on displacement does of course not imply that the stresses converge monotonically over the whole domain).

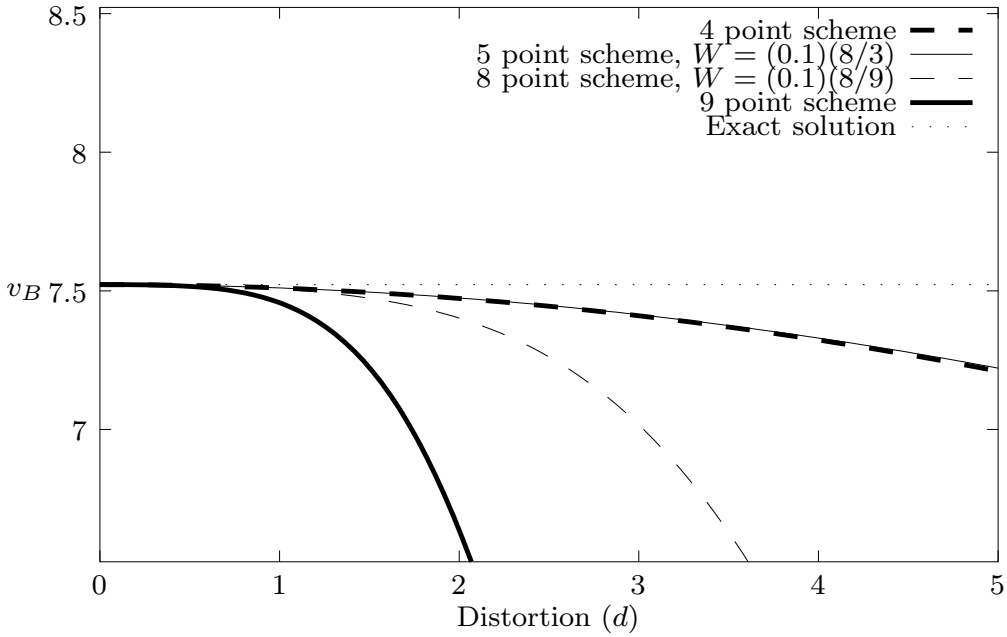

Figure 4.9: Distorted cantilever beam: Effect of distortion d on v_B for various integration schemes with Q8 elements.

4.5 Conclusion

The effect of modified reduced order quadrature rules on the presence of spurious modes in the stiffness matrices of the Q8 serendipity and Q9 Lagrange membrane finite elements has been investigated. For these elements, modified reduced order quadratures present an alternative to full integration using order 3 Gauss rules, (which results in excessively stiff behavior), and reduced integration using an order 2 Gauss rule, (which results in the introduction of spurious modes on the element level). Even though the spurious mode associated with the Q8 element is non-communicable, it remains undesirable, and may influence results in a number of situations of practical importance, e.g. topology optimization.

The alternative 5 and 8 point schemes proposed for respectively Q8 and Q9, allow for the elimination of spurious modes, while element accuracy is enhanced as compared to order 3 Gauss rules, through the introduction of soft higher order deformation modes. For the respective elements, the following considerations are pointed out:

For the Q8 element, both the 5 and 8 point rules can be used for integrating the element stiffness matrix. In each case the spurious mode is eliminated. If the weights W_0 and W_β are both chosen to be in the order of 10% of the maximum allowable weight, a highly accurate element is obtained. The numerical cost of the 8 point scheme is higher than the 5 point scheme, with no obvious benefits. Hence it is recommended that the Q8 element be integrated using the 5 point rule, with $W_0 = 0.1(8/3) = 8/30$.

For the Q9 element, the 5 point rule is inadequate since only one of the three spurious modes is eliminated. The 8 point rule (with $W_\beta = 0.1(8/9) = 8/90$) results in a rank

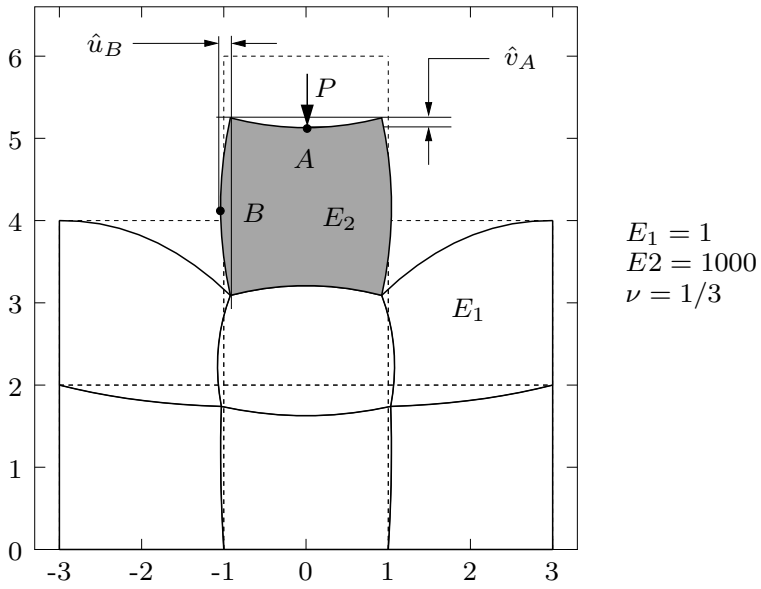

Figure 4.10: Near mechanism with point load.

sufficient element of increased accuracy as compared to the fully integrated counterpart.

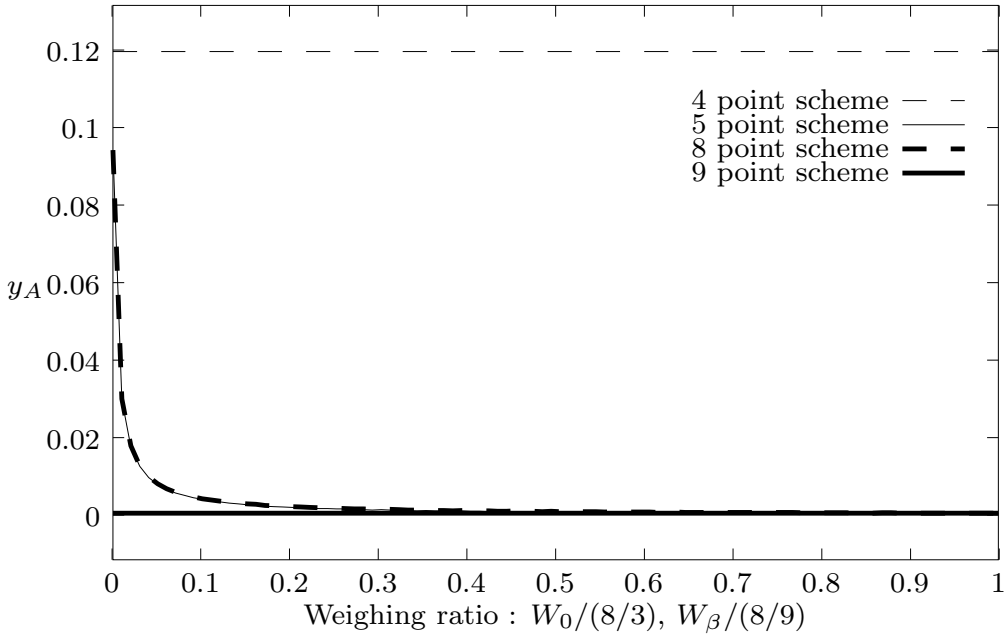

Figure 4.11: Incremental displacement $\hat{v}$ at A.

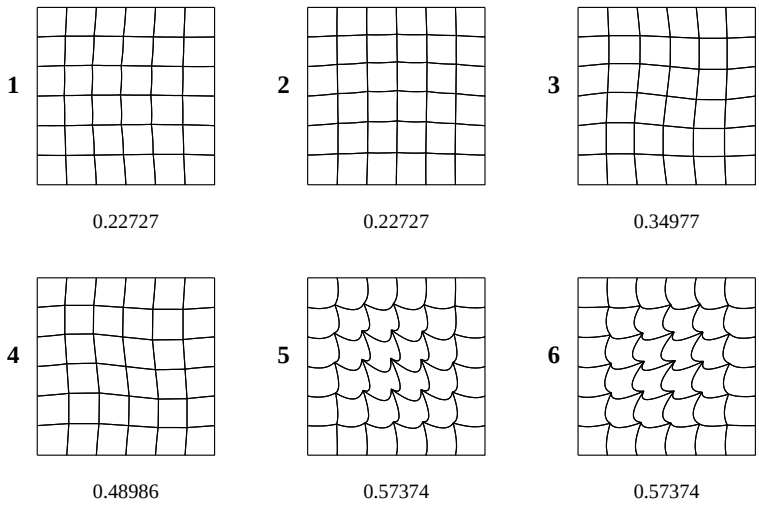

Figure 4.12: Lowest six eigenvalues and eigenvectors (Escher modes) for constrained mesh with Q9 elements and 4 point integration scheme (mesh size 6×6, $E = 2.4$, $\nu = 0.2$).

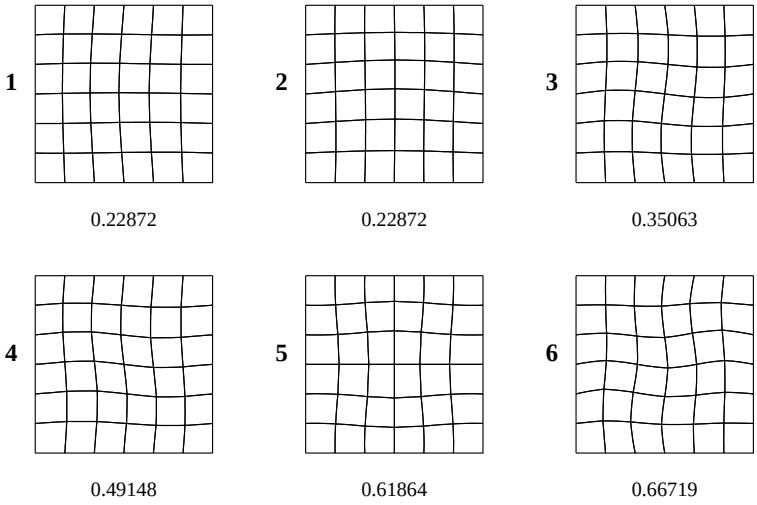

Figure 4.13: Lowest six eigenvalues and eigenvectors for constrained mesh with Q9 elements and 9 point integration scheme (mesh size 6×6, $E = 2.4$, $\nu = 0.2$).

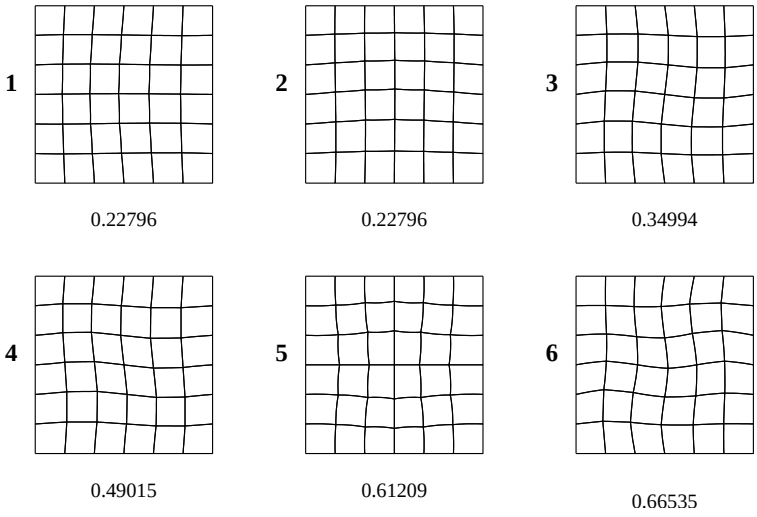

Figure 4.14: Lowest six eigenvalues and eigenvectors for constrained mesh with Q9 elements and 8 point integration scheme, $W_\beta = 0.1(8/9)$ (mesh size 6×6, $E = 2.4$, $\nu = 0.2$).

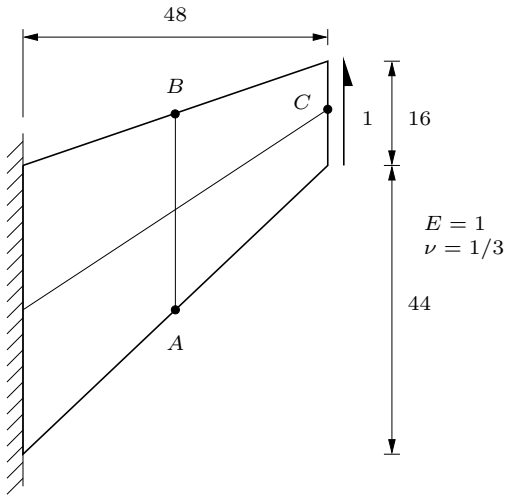

Figure 4.15: Cook's membrane

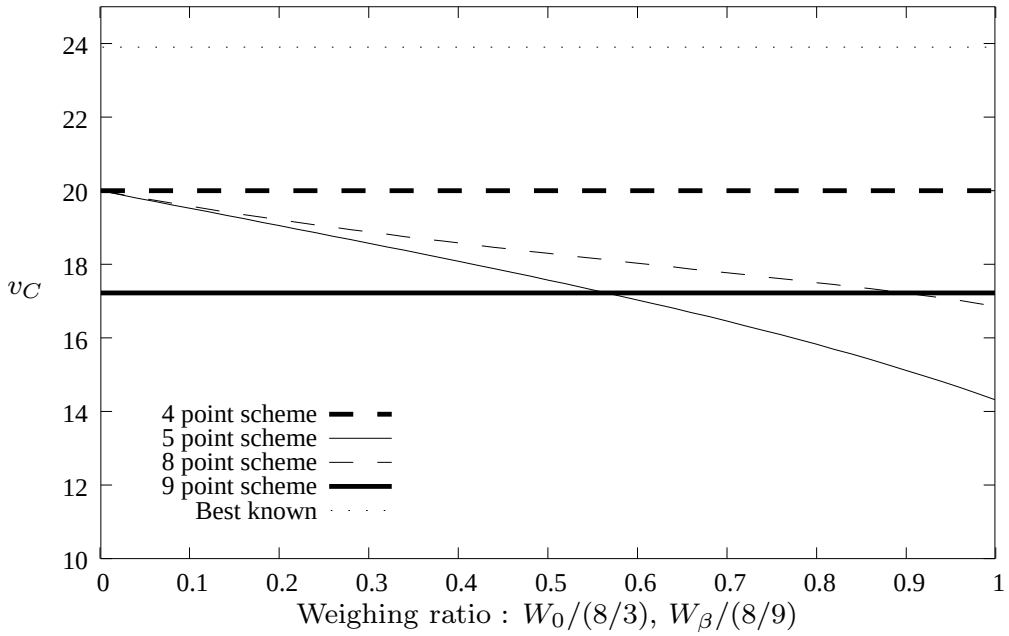

Figure 4.16: Effect of weight on v_C for Cook's membrane (Q8, 1×1 mesh).

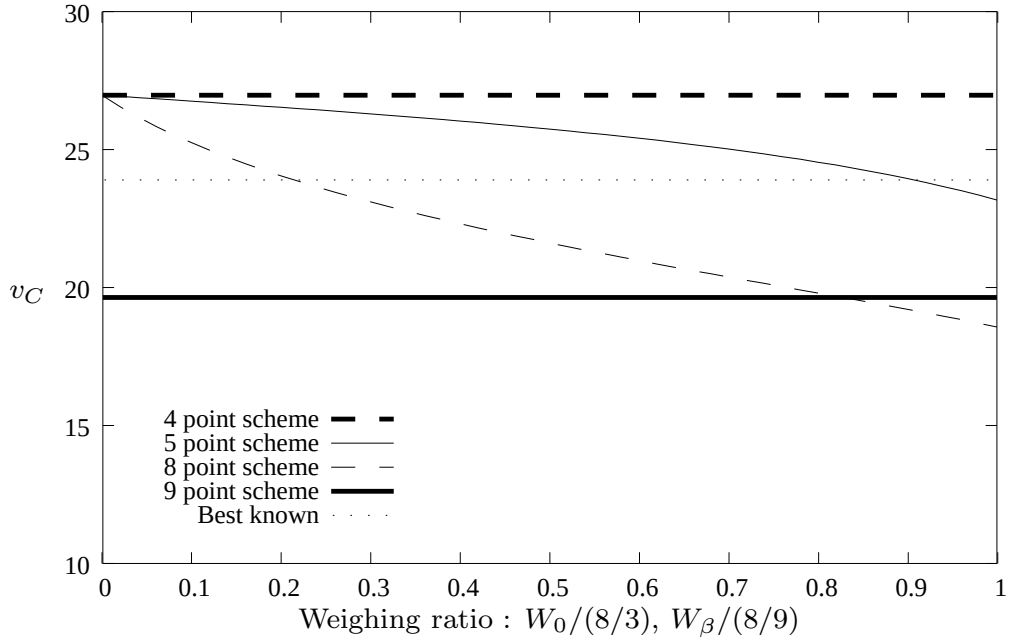

Figure 4.17: Effect of weight on v_C for Cook's membrane (Q9, 1×1 mesh).